CSD Hydrodynamics

An analysis of a CSD in coastal conditions, and the effect of flexible spud keeper configurations on the hydrodynamic response.

Master of Science Thesis

Jesse Dijkstra

Delft University of Technology

TU Delft

DAMEN

CSD Hydrodynamics

An analysis of a CSD in coastal conditions, and the effect of flexible spud keeper configurations on the hydrodynamic response.

Master of Science Thesis

by

Jesse Dijkstra

18th January, 2023

For the degree of Master of Science in Offshore and Dredging Engineering
at Delft University of Technology,
to be defended publicly on February 15th, 2023 at 10:00 AM.

Student number:	4492099	
Project duration:	March 2022 - December 2022	
Thesis committee:	Prof. Dr. Ir. C. van Rhee	TU Delft, Chair
	Dr. Ir. S. A. Miedema	TU Delft
	Dr. Ir. R. L. J. Helmons	TU Delft
	Ir. F. Smeets	Damen, Supervisor

Faculty of Mechanical, Maritime and Materials Engineering (3mE) · Delft University of Technology

TU Delft

Preface

This thesis describes the process of my graduation project for the degree of Master of Science in Offshore and Dredging Engineering at TU Delft. The project was carried out at and on behalf of Damen Dredging Equipment in Nijkerk.

Writing a thesis and finishing a degree always seemed like a daunting task to me. The subject of computational modelling of ship hydrodynamics in particular has been researched by some of the finest in this field of study, so it was important to find a niche that fit my background. I can say however that these past months have flown by, mostly through the help of some wonderful people at Damen and the TU Delft. I would like to take a moment to express my gratitude and appreciation to all of them, in particular:

Steven van Braak, for getting me onboard at DDE, and Frank Bosman for helping me set the boundaries of my project and giving me the freedom and confidence to adapt the project to suit my background and interests.

Floris Smeets, for his time and continuous support with advice and encouraging words, and helping me find my way within Damen in both Nijkerk and Gorinchem. Thank you for driving up and down to Delft to be present at the meetings, it is much appreciated.

Karthik Sankaramoorthy and the people at R&D in Gorinchem, for their help with everything hydrodynamics-related and assisting me with any modelling problems I came across.

Mark Winkelman, Florent Cochennec, and the entire engineering department at DDE, for their advice and expertise on the topic of CSDs and welcoming me into the office.

Cees van Rhee, for his help and guidance this past year and getting me in contact with some of the greats in the field of dredging and computational modelling. The insights into the practical side of dredging have been a great help in keeping the project focused and concise.

All my friends in Delft, Hoevelaken and all across the Netherlands, everyone at CLAFC and Weldam, who helped me take my mind off the project and gave me some valuable moments of procrastination.

Lastly, I owe a big thank you to my family who graciously put up with me over these nine months, especially during the stressful final portions of the project. I truly could not have done this without you.

Jesse Dijkstra
Delft, January 2023

Abstract

Cutter suction dredgers (CSD) are highly vulnerable to large wave loading due to their stiff, spud-based mooring. Many mitigations targeted at reducing the resulting stresses on the spud and other critical operating components have been proposed in recent years, most notably by adding a level of flexibility to the connection between the pontoon and the spud for rotational motions. Investigating the merits of the implementation of a flexible spud keeper however are hindered by the lack of accurate, CSD-specific models that are able to simulate real waves in the working area, as well as the multibody system of a CSD and its complex interactions with the sea floor. In this thesis, an ANSYS AQWA model is developed to conduct an operability analysis of a CSD in operation in offshore, coastal conditions. Three modelling objectives were established to provide a complete analysis of the effect of increased flexibility in a spud keeper: adding non-linear wave effects, improvement of the soil boundary conditions, and building a dynamic multibody system of a CSD in ANSYS AQWA.

A wave model is developed that expands upon standard Linear Wave Theory (LWT) through the use of Stokes 2nd Order Wave Theory (S2). S2 was found to be valid for a larger range of water depths and wave parameters than other wave theories, mainly in shallow, coastal conditions, which is the main operating area of a CSD. These non-linearities cannot be implemented into a frequency domain (FD) model, therefore a time domain (TD) model is required. A combination of S2 waves in a JONSWAP spectrum is used to simulate the motion and force response in TD, as well as second-order forces from the interaction of wave groups with the CSD. The model output is then used as a means of verification of these assumptions and to show the effect of the wave shapes on the spud bending stress.

An altered spud model is proposed for shallow, wide spuds, using a rotational spring system instead of the commonly used clamped model. For the use-case of a CSD it shows a spud's tendency for rigid motion below the mudline, while also providing an upper operational limit for soil failure around the spud. The model output showed this upper limit to likely not be a important operational limit, but it can be used to investigate spud rotation below the mudline. Mooring effects from the cutter are absent in older models, but are added in the form of spring elements to better approach reality.

Finally, a number of CSDs with different levels of flexibility are tested for four operational limits. The model shows a clear shift in motion resonance towards lower frequencies when the stiffness is decreased, while operability analysis in TD presents a significant increase in operability when a CSD is free to move in pitch. This completely flexible connection provides a major reduction in spud bending stress, but is governed by the acceleration limit of the pontoon. Other reduced stiffness designs are shown to only provide limited benefits to the operability.

Contents

Nomenclature

Abbreviations

Abbreviation	Definition
BC	Boundary Condition
BS	Bretschneider Spectrum
COB	Center of Buoyancy
COG	Center of Gravity
CS	Clamped Spud Keeper
CSD	Cutter Suction Dredger
DOF	Degree of Freedom
EOM	Equation of Motion
FD	Frequency Domain
FEM	Finite Element Method
FK	Froude-Krylov Forces
FLS	Force-Limited Spud Keeper
FS	Flexible Spud Keeper
HD	Hydrodynamic Diffraction
HR	Hydrodynamic Response
JONSWAP	Joint North Sea Wave Project
KdV	Korteweg-de Vries Equation
LWT	Linear Wave Theory
NLWT	Non-linear Wave Theory
QTF	Quadratic Transfer Function
RAO	Response Amplitude Operator
S2	Stokes 2nd Order Wave Theory
SWL	Still-Water Line
TD	Time Domain

Symbols

Waves - Symbols

Symbol	Definition	Unit
A	Area	[m^2]
B	Beam	[m]
c	Phase velocity	[m/s]
$c(\alpha)$	Directional coefficient	[-]
C_D	Drag coefficient	[-]
cn	Jacobi elliptic function	[-]
F	Force	[N]
g	Gravitational constant	[m/s^2]

Symbol	Definition	Unit
h	Water depth	[m]
H	Wave height	[m]
H_b	Breaking wave height	[m]
H_s	Significant wave height	[m]
k	Wave number	[rad/m]
K_s	Shoaling coefficient	[-]
L	Length	[m]
m_0	Zero-th order moment	[-]
n	Number of waves	[-]
p	Pressure	[N/m^2]
S	Steepness	[-]
$S(\omega)$	Wave spectrum	[m$^2 \cdot$ s]
t	Time	[s]
T	Draught	[m]
T_ζ	Mean wave period	[s]
T_p	Wave period	[s]
T_p	Peak wave period	[s]
T_s	Significant wave period	[s]
u	Horizontal water particle velocity	[m/s]
U_R	Ursell number	[-]
v	Horizontal water particle velocity	[m/s]
w	Vertical water particle velocity	[m/s]
α	Wave direction	[rad]
α_ω	Phase shift	[rad]
ϵ	Dimensionless wave height	[-]
γ	Peak enhancement factor	[-]
λ	Wavelength	[m]
μ	Relative depth	[-]
ω	Wave frequency	[rad/s]
ω_ζ	Mean wave frequency	[rad/s]
Φ	Velocity potential	[-]
Ψ	Stream function	[-]
ρ	Density	[kg/m^3]
ζ	Surface elevation	[m]
ζ_a	Wave amplitude	[m]

Soil interaction - Symbols

Symbol	Definition	Unit
A	Loading factor	[-]
c_{ij}	Stiffness in i-direction due to j-mode	[N/m]
D	Spud diameter	[m]
E	Young's modulus	[Mpa]
e	Loading eccentricity	[m]
E_{kin}	Kinetic energy	[J]
EI	Flexural rigidity	[N/m^2]

Symbol	Definition	Unit
G	Shear modulus	[MPa]
h_c	Cone height	[m]
Δh	Spud dropping height	[m]
H_ult	Ultimate lateral capacity	[N]
I_{ij}	Area moment of inertia	[m^4]
K_θ	Rotational stiffness	[Nm/rad]
K_{P_u}	Ultimate net pressure coefficient	[-]
K_{rs}	Relative spud stiffness	[-]
K_p	Rankine's coefficient of passive earth pressure	[-]
L_pen	Spud penetration depth	[m]
m	Mass	[kg]
M_ult	Ultimate moment capacity	[Nm]
P	Power	[W]
p_u	Ultimate soil pressure	[Pa]
Q_{ur}	Spud tip load	[N]
r	Radius	[m]
R_1	Internal spud diameter	[m]
R_2	External spud diameter	[m]
R_u	Modified soil resistance	[N]
t	Wall thickness	[m]
T	Tension	[N]
T_0	Pretension	[N]
v	Poisson's ratio	[-]
v_w	Swing speed	[m/min]
w	Spud deflection	[m]
α	Shaft friction factor	[-]
α_d	Drop correction factor	[-]
β	Shaft friction factor	[-]
γ'	Effective unit weight	[N/m^3]
γ_a	Saturated unit weight	[N/m^3]
ϕ'	Effective soil stress friction angle	[$^\circ$]
ϕ'_a	Angle of internal friction	[$^\circ$]
ϕ_s	Swing angle	[$^\circ$]
σ'	Effective stress	[Pa]

Multibody dynamics - Symbols

Symbol	Definition	Unit
A_{ij}	Added mass for force in i-direction from acceleration in j-mode	[kg]
B_{crit}	Critical damping factor	[Ns/m]
B_{ij}	Damping component for force in i-direction from velocity in j-mode	[Ns/m]
C_B	Block coefficient	[-]
C_f	Friction coefficient	[-]
C_M	Inertia coefficient	[-]

Symbol	Definition	Unit
f	Morison force	[N/m]
$F^{(2)}$	Second-order wave force	[N]
Fn	Froude number	[-]
K_{eq}	Equivalent spud stiffness	[N/m]
k_{ij}	Radius of gyration	[m]
KC	Keulegan-Carpenter number	[-]
$\vec{n}$	Normal direction vector	[-]
R_{ij}	Retardation function for force in i-direction due to motion in j-mode	[Ns/m]
r_c	Effective bilge keel radius	[m]
S	Wetted surface area	[m^2]
ϕ	Roll angle	[rad]
Φ_D	Diffraction potential	[-]
Φ_I	Undisturbed wave potential	[-]
Φ_R	Radiation potential	[-]
ψ	Yaw angle	[rad]
θ	Pitch angle	[rad]
θ_L	Ladder pitch angle	[rad]

List of Figures

List of Tables

1 Introduction

Most dredging vessels, especially smaller designs, have always been limited in their workability by their response to waves and the forces and motions these induce on critical operating components. The recent move away from working in sheltered waters into offshore coastal areas only exacerbates this issue, where waves and tidal currents are not only ever present, but far more intense than in rivers and lakes. No vessel is more affected by this change than the cutter suction dredger (CSD), with its need to be anchored to the sea floor by a spud pole. As a result its behaviour and response to waves becomes extremely stiff in comparison to regularly moored vessels with anchor lines, almost comparable to bottom-founded offshore structures in certain scenarios. Problems arise when waves enter the resonant frequencies of the CSD, leading to reduced workability due to the large motions, possible damages to the spud or cutter and even safety concerns for the personnel on board. Prevention of scenarios where the workability limits are exceeded therefore need to be avoided at all costs. Commercial dredgers have tried to mitigate these issues by introducing a certain level of flexibility in the connection between the spud and the pontoon [57]. These flexible spud keepers would allow some rotational movement of the pontoon and thereby reducing the spud stress. These designs come with their own set of operational limits based on both structural limits as well as restrictions to the allowed motion of the vessel for proper operation. The viability of such a flexible spud keeper comes down to how much the operability window is increased compared to the original system. Because a design change of this magnitude can be very drastic both economically, as well as in the way the CSD operates, an in-depth analysis of the possible benefits of this new design is required.

Comparing what level of flexibility and which design is most effective in coastal waters requires an accurate model which is able to simulate different real-world wave climates. Commonly used hydrodynamic response models are arguably not significantly accurate when it comes to predictions in shallow water, as they tend to be based on deep-water assumptions which ignore the strong non-linearities that exist in coastal conditions [86]. The linear aspects have been sufficiently studied with the use of frequency domain modelling, however not much has been done to include these coastal non-linearities, which require an expansion into time domain simulation [84]. Furthermore, CSD-specific models often use simplified representations of the characteristic operational and mooring forces. Knowledge on the validity of these simplifications is limited and should be investigated, especially in the areas of interaction of important components with the soil, and the coupled dynamics of the cutter ladder and the pontoon. This thesis will elaborate on the creation of such a model and use it to analyse a number of flexible spud keepers to extend the operability window for coastal conditions.

This chapter will introduce the difficulties associated with the use of cutter suction dredgers in coastal waters and the motivation behind the research in this report, a small introduction into the history and workings of a cutter suction dredger, as well as the general research goals to be attained and the structure of this document.

1.1. Cutter suction dredgers and history of modelling

A Cutter Suction Dredger (CSD) is a stationary dredging vessel anchored to the sea floor by a large spud pole. The first CSD can be traced back to 1884 [78], when large amounts of sandstone had to be cut in the port of Oakland, California. Since then, the design has changed and the scale has increased drastically, but the main working method has remained the same.

During operation, the CSD will rotate itself around the spud in an arc, as depicted in Fig 1.1 [3]. This rotation is caused by the winching of swing wires extending from the cutter ladder, anchored to the sea floor. A cutter ladder with attached cutter head is lowered down to the sea floor to cut a wide range of soils, from sand to rock, which is then sucked up by the dredge pump. This slurry flow is usually transported via floating pipeline to a discharge location. To move the CSD forward another 'step', the spud pole has to be moved. In most cases the spud is mounted on a movable spud carriage system on the aft of the vessel. In this system the spud is clamped at two points, thereby only allowing the pontoon to move in heave and yaw. After a swing, the pontoon moves forward with respect to the spud and makes another swing in the opposite direction. This continues until the spud is lifted and moved up to the front of the spud carriage to allow this process to start over again. While moving the primary spud, an auxiliary spud is lowered to keep the CSD in place. One step can cover up to multiple meters and includes multiple swings of the cutter, depending on the size and power of the CSD and the soil that is cut [77].

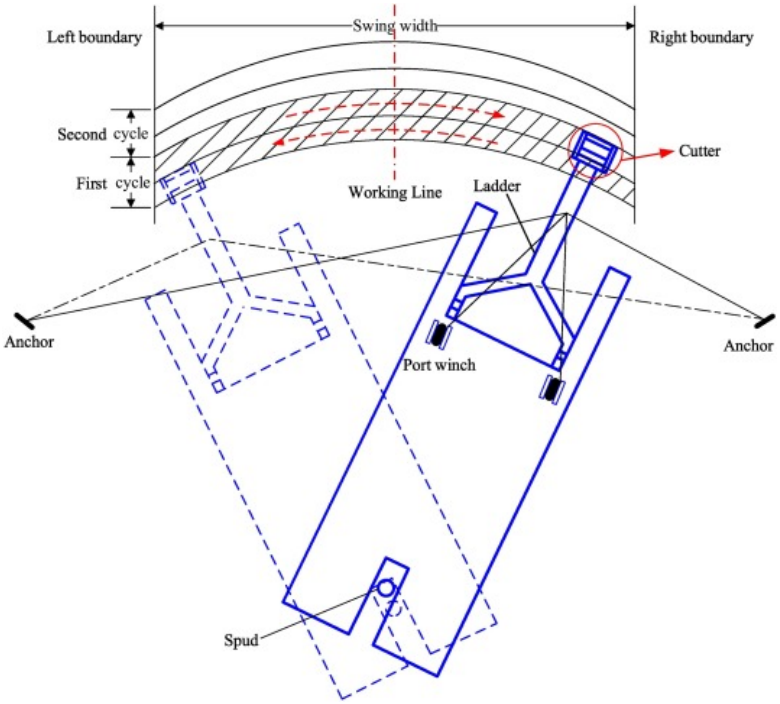

Figure 1.1: Swing pattern of a CSD in operation [3].

CSDs are often for dredging activities that require precision without needing to displace the slurry a great distance. Generally, a distinction is made between highly specialised dredgers that are made for a specific project, and multi-purpose commercial dredgers. These specialised dredgers are disassembled after completion of their intended use case, whereas commercial dredgers can have a lifetime of over 20 years. For commercial dredgers, a high level of adaptability and a wide range of utilisations is therefore required. This results in a single CSD needing to be able to perform in various wave climates and weather environments, often without any supporting vessels, while still remaining economically viable for smaller projects. Expanding a CSD's operating range into coastal waters is one of the examples of an increase in this required adaptability. It would require the dredger to withstand large wave forces which are not present in sheltered waters, as well as larger current components. In an attempt to alter their design for these new conditions, larger dredgers have pivoted to the use of flexible spud carriages, where the pontoon is allowed certain freedoms in rotation to limit the overall stress on the spud.
The combination of environmental forces from waves, wind and currents are the main elements preventing operation due to the structural stresses they induce, mainly on the spud and cutter ladder. According to studies done by Miedema [51], there are four main aspects of operation which limit the workability:

- **Stress in the spud pole and soil failure:** The spud's ability to counteract movement and forces from the pontoon and the cutter ladder is limited by its own interaction with the soil. When this exceeds the maximum soil reaction forces, the spud can leave the soil and thereby destabilise the system. Structurally, excessive deflection of the spud can lead to buckling and other forms of permanent damage to the spud. The increased stiffness of the system compared to normal floating vessels can cause resonant motions due to the wave loading.
- **Forces on the swing wires:** The forces on the wires can cause breakage when having to accommodate the swing motion as well as environmental forces. On top of that, the winches controlling the swing motion only have a limited power, which if exceeded would prevent operation.
- **Motions and accelerations of the pontoon:** Excessive motions and accelerations of the pontoon can cause large forces on other components such as the spud keeper connection and the hinge pin of the cutter ladder, but mostly it can be harmful to the safety of personnel on board due to shifting of heavy machinery or other on-deck elements.
- **Cutter head movement:** The cutter ladder is connected to the pontoon by a simple hinge system to allow the ladder to be easily hoisted up and down to different working depths. This however allows the cutter head to rotate around this hinge point, which can cause problems when the cutter head is pushed into the breach, creating axial stresses in the cutter ladder. Secondly, the cutter ladder should not be lifted of the soil as this prevents the cutting action.

These limits provide an upper bound to the sea-states that are suitable for dredging operation. If environmental conditions can be expressed in terms of these limits, a good estimate of the workability in a specific region can be made. Larger dredgers tend to exceed their operability limits quickly in sea states commonly found in coastal areas. An expansion of this operability range would require an alternative spud carriage system to relieve stresses on the spud.

Research and modelling of sea-going dredgers is not a recent phenomenon. From 1980 onward, the workability of multiple dredging vessels was studied, most notably by Wichers [84]

and Miedema [51]. This culminated in modelling programs capable of frequency domain analysis of a CSD in operation, such as DREDMO by Miedema [49] and DREDSIM by the Dutch Marine Research Institute MARIN [85]. Problems arose when the model outputs were compared to real-world data, which tended to differ significantly. Attempts to correct these discrepancies were done, but the programs never caught on for commercial use. More recently, Royal IHC developed the Dynamic Operations in Dredging and Offshore (DODO) tool for the evaluation of a CSD design in waves [26]. This tool allows for the modelling of the hydrodynamic response as well as characteristic dredging forces. It however does not account for mooring effects of the cutter ladder as it assumes the mooring load is completely absorbed by the spud and the swing wires, and it simplifies the connection of the spud in the soil to a clamped support.

1.2. CSD700

For the purposes of this project, Damen's CSD700 vessel will be analysed. Damen has been a world leader in shipbuilding for many years, using their business model of standardised ship design to provide highly adaptable CSDs that are able to operate in a wide variety of conditions. The CSD700 will be Damen's largest CSD to date, with a slurry pipe diameter of 700 mm and the capability to dredge soil up to 25 m water depth. The design of the CSD700 is part of the ongoing CSD2.0 project which aims to redesign CSDs in order to achieve better working efficiency and the ability to dredge in offshore conditions and other unsheltered waters. It features a number of design changes which affect the hydrodynamic response, including a reduction in overall length in mooring condition and a tapered pontoon shape. A full overview of the design and the principal dimensions of the CSD700 used in this thesis is given in Appendix A.

1.3. Problem statement

The ability of a CSD to operate has always been linked to the statistical prediction of weather and ocean environments in the working area. The move from in-land dredging to offshore dredging expands the need for accurate prediction methods because of the larger wave loading and tidal current effects. Predicting the response of a CSD to these conditions requires an accurate model of not only the specific wave climate of coastal waters, but also the interaction between the soil and the vessel, as well as the dynamics of the cutter ladder interacting with the pontoon and the spud. Damen has used models from other spud-pontoon vessels to approximate the behaviour of a CSD in waves, but these vessels either have very different operating conditions, or the model becomes too general and loses the intricacies of real-world situations. Accurate prediction of a CSD's motion response therefore requires an adequate model including all CSD-specific boundary conditions and a better description of coastal waters.

This thesis aims to expand upon the ideas of previous sea-going dredger research and models by creating a new model covering all aspects of CSD operation, culminating in an analysis of flexible spud keeper systems. This requires three new modelling elements. Firstly, a new way of describing the wave climate in coastal areas has to be examined. The majority of research involving CSDs and their hydrodynamic response rely on linear wave theory and frequency domain (FD) responses to regular waves. Experiments on wave shapes near the coast have shown that FD analysis overlooks non-linear wave phenomena which alter the magnitude and distribution of the wave forces compared to standard regular waves used in the frequency domain [19]. Due to their non-linear nature, these phenomena have to be included in a time domain (TD) model. Secondly, the model itself has to be expanded. Older models are made

up of assumptions which no longer hold up for significant wave loading [34]. Previous assumptions included a clamped or pinned spud below the mudline and a ladder which is hoisted up to a horizontal position. The real effects of these boundary conditions need to be checked and verified with experimental data to approach a realistic scenario.
Lastly, these elements need to be merged into a multi-body dynamic model. Because the movement of the cutter ladder relative to the pontoon is a crucial workability limit, it can no longer be assumed that the cutter ladder is merged with the pontoon. Ultimately, an operability analysis can be performed on different spud keeper configurations to determine the advantages and disadvantages compared to the original clamped system. A model is proposed using the diffraction software ANSYS AQWA and the more complex systems are processed in MATLAB. This model is capable of both FD and TD calculations. The FD model is crucial as a prerequisite to the TD calculations, but also as a form of verification with previous research. The TD model can then be used to account for the non-linearities described above.

1.4. Research goals

Summarising the problem statement above yields the following main research question for this thesis:

"How can different flexible spud keeper configurations be modeled and incorporated into a dynamic multibody model of a CSD in coastal conditions, and what are the effects on its hydrodynamic response?"

To achieve an in-depth answer to this question, a model has to be build which can investigate the flexible spud keeper configurations which can realistically simulate a CSD in coastal conditions. This model aims to achieve three main objectives:

1. Building and verifying a model of wave forces, including non-linear wave phenomena and shallow water effects.
2. Modelling and verifying the boundary conditions such as the spud-soil interaction, representation of the swing wire forces and reaction forces related to the cutter in operation.
3. Modelling kinematics of the CSD-spud system as a multibody system, where the cutter ladder can move independently of the pontoon. The response of the system should be described in the time domain to account for shallow water non-linearities. Using this model, different flexible spud keeper configurations are analysed for their impact on CSD motions, spud stress and deflections and their overall effect on the workability of a CSD.

A general outline of the approach to answer these questions is given in Fig. 1.2.

1.5. Document structure

This thesis is structured into a nine parts. Firstly in *Ch. 2 - Waves*, wave theories are discussed in terms of their applications in different coastal conditions, as well as how wave statistics will be used to accurately represent a realistic wave spectrum in the model. Secondly in *Ch. 3 - Soil interaction*, all boundary conditions are discussed where the CSD interacts with the sea floor. It will establish limits to these conditions and propose a new way of modelling a spud pole based on recent research foundings. Next in *Ch. 4 - Multibody dynamics*, the equation of motion is discussed which governs the motions of the CSD when interacting with waves. Important hydrodynamic coefficients are verified analytically and with experimental data to ensure the model is accurate compared for practical applications. In *Ch. 5 - Modelling*, the findings of the previous chapters are summarised to provide the model made in ANSYS AQWA in both

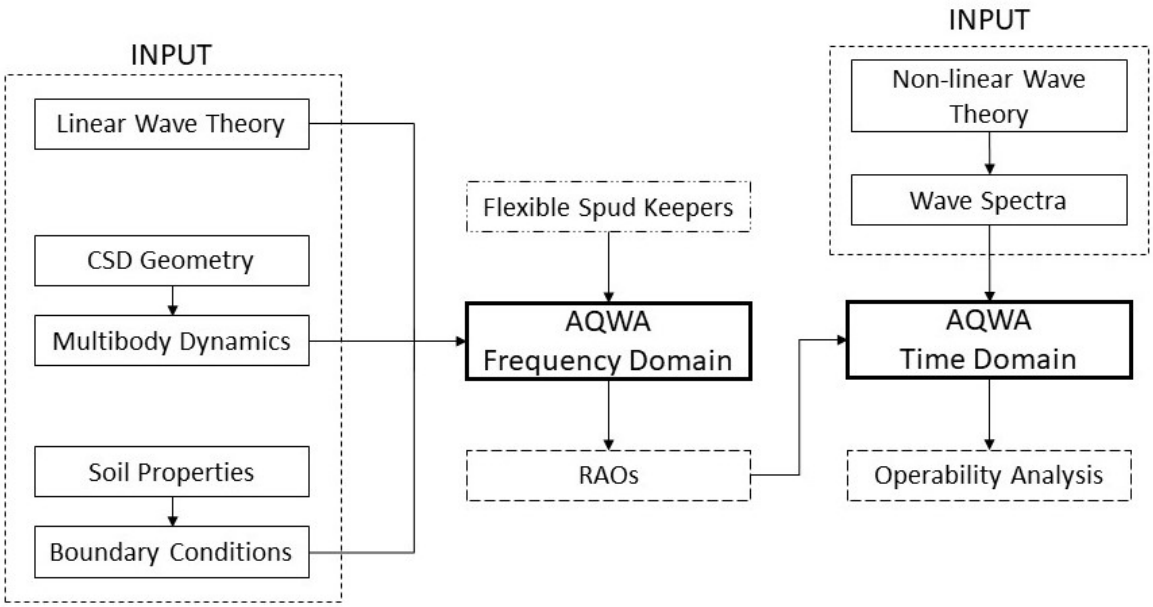

Figure 1.2: General project outline.

the frequency domain and the time domain. The different flexible spud keeper configurations are outlined and the motion response of the original CSD system is verified with analytical data. This motion response is used as a benchmark for the FD models of the flexible spud keeper configurations presented in *Ch. 6 - Results and Discussion - FD*, which provide the differences between the different designs through their components in the equation of motion. The FD model is transformed into TD in *Ch. 7 - Results and Discussion - TD* to verify the wave theory assumptions made previously and perform the operability analysis which answers the main research question. Lastly, the major findings of this thesis and their effects on the future of hydrodynamic modelling of CSDs are presented in *Ch. 8 - Conclusion* and the possibilities for further research and verification are elaborated upon in *Ch. 9 - Further research*. Any utilised symbols or terms are explained in the glossary prior to this introduction chapter, which concludes with a list of figures and tables present in the report.

2

Waves

Waves, currents and their interactions with the environment differ wildly in coastal areas all around the world. Knowledge of accurate metocean conditions in the operational area is key to ensuring safe dredging activities. In the absence of real-time wave elevation or current data in the form of wave buoys or other altimetry measurement devices, one must resort to a statistical approach to predicting important factors like wave height, wave period and the amount of kinetic wave energy that is transferred onto the dredger. It is therefore critical that a representative load case is found for a dredger at sea. This chapter aims to give insight into standard wave theory and the associated parameters that come with linearised wave theories, followed by the inclusion of non-linear elements of these wave theories which are important especially in shallow water operating conditions. Afterwards, the validity of these theories is discussed for different wave climates and wave shapes. These theories are then used to find the spectral definition of waves using real wave scatter diagrams. Static forces like current and wind are shortly discussed in the context of a CSD in operation. Finally, a case is given which will be used to determine the hydrodynamic response in the TD model.

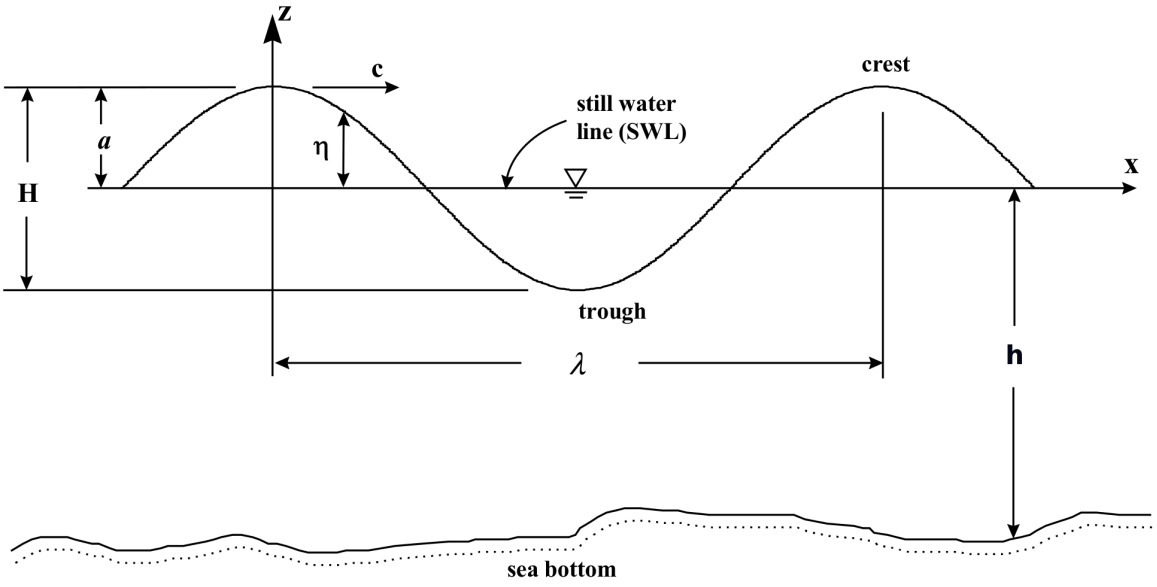

Figure 2.1: Representation of a travelling regular wave.

Wave records are often described by either deterministic and regular waves, or random and irregular waves. Regular waves have a sinusoidal character and can be expressed as a function of their amplitude ζ_a (or a), period T and total wavelength λ, resulting in the surface elevation profile ζ as a function of space x and time t, as shown in Fig. 2.1 [43]. In linear wave theory, this surface elevation is described as [1]:

$$\zeta = \zeta_a \cos(kx - \omega t) \tag{2.1}$$

To get a better approximation of a real sea state, this equation is expanded to include many amplitudes and many wave frequencies. The resulting surface elevation profile then becomes the sum of many varying regular waves:

$$\underline{\zeta}(t) = \sum_{i=1}^{N} \underline{\zeta_a}_i \cos\left(2\pi f_i t + \underline{\alpha}_i\right) \tag{2.2}$$

This is known as the superposition principle of waves, which was first described within hydrodynamics by St. Denis and Pierson [71]. This is illustrated in Fig. 2.2.

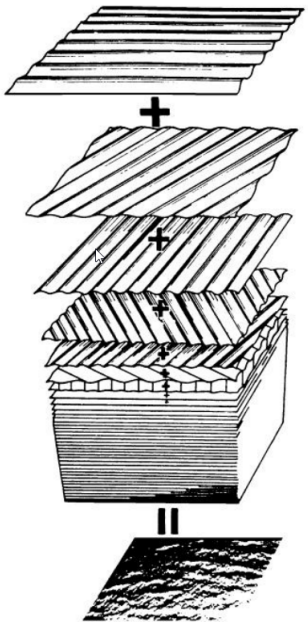

Figure 2.2: Multiple regular waves, added together by way of the superposition principle [62].

2.1. Linear wave theory

Linear Wave Theory (LWT) is the most commonly used wave theory, as it is fairly simple while also being applicable and a good estimation for the real world in most cases, especially in deep water. To properly examine the differences and validity of different wave theories and their application, some base definitions need to be established (symbols and variables are used as described in Fig. 2.1, except ζ is used to denote surface elevation instead of η) [30]:

- **Wave height.** In LWT, waves are regular and sinusoidal as described in Fig. 2.1. It follows that the wave height is:

$$H = 2 \cdot \zeta_a \tag{2.3}$$

- **Wave steepness.** The steepness of a wave is an important parameter in the validity of different wave theories and determines certain wave behaviours, such as wave breaking:

$$S = \frac{H}{\lambda} \tag{2.4}$$

- **Wave number.** Wave number k expresses the spatial frequency of a wave, or the amount of wave passed per meter of wavelength:

$$k = \frac{2\pi}{\lambda} \tag{2.5}$$

- **Phase velocity.** Also referred to as wave celerity, the phase velocity is a metric describing the speed with which a single wave propagates through its medium:

$$c = \frac{\lambda}{T} = \frac{\omega}{k} \quad \text{for} \quad \omega = \frac{2\pi}{T} \tag{2.6}$$

To be able to apply LWT, one has to assume a small wave steepness and small wave amplitude compared to its wavelength or the water depth, meaning any squared steepness terms can be ignored. As LWT is a first-order theory, some simplifications have to be made to exclude higher-order terms. This results in the following approximations (using an arbitrary variable x):

$$\begin{aligned} &\text{For large x:} \quad sinh(x) \approx cosh(x) >> x \\ &\qquad\qquad\quad\ \ tanh(x) \approx 1 \end{aligned} \tag{2.7}$$

$$\begin{aligned} &\text{For small x:} \quad sinh(x) \approx tanh(x) >> x \\ &\qquad\qquad\quad\ \ cosh(x) \approx 1 \end{aligned} \tag{2.8}$$

In these conditions we consider a 2D situation. Horizontal wave motion is independent in x and y-direction, so any wave displacement, velocity or acceleration given in x-direction also applies for y-direction. Furthermore, the fluid is assumed to be incompressible, irrotational with continuous flow [30].

2.1.1. Potential theory

The wave potential Φ_w is defined as the integral of the flow velocity (u, v, w) in its direction, integrated over its respective direction (x, y, z).

$$\begin{aligned} \Phi_w &= \frac{\zeta_a g}{\omega} \cdot \frac{\cosh k(h+z)}{\cosh kh} \cdot \sin(kx - \omega t) \\ \text{for: } u = \dot{x} &= \frac{\partial \Phi_w}{\partial x} \quad v = \dot{y} = \frac{\partial \Phi_w}{\partial y} \quad w = \dot{z} = \frac{\partial \Phi_w}{\partial z} \end{aligned} \tag{2.9}$$

To solve this potential, four requirements or boundary conditions need to be fulfilled [37]:

1. **Continuity equation or Laplace equation.** This equation ensures that wave energy is conserved. Because these velocities can be integrated to the potential function, the continuity equation 2.10 results in the Laplace equation 2.11:

$$\frac{\partial u}{\partial x} + \frac{\partial v}{\partial y} + \frac{\partial w}{\partial z} = 0 \tag{2.10}$$

$$\nabla^2\Phi = \left(\frac{\partial^2\Phi}{\partial x^2} + \frac{\partial^2\Phi}{\partial y^2} + \frac{\partial^2\Phi}{\partial z^2}\right) = 0 \tag{2.11}$$

2. **Seabed boundary condition.** Water particles cannot travel through the seabed, therefore the vertical velocity of these particles at the seabed has to be zero:

$$\frac{\partial\Phi_w}{\partial z} = 0 \quad \text{for} \quad z = -h \tag{2.12}$$

3. **Free surface kinematic boundary condition.** The vertical velocity of the upper water particles at the sea surface has to be equal to the vertical velocity of the free sea surface ζ:

$$\frac{\partial\Phi}{\partial z} = \frac{\partial\zeta}{\partial t} + u\frac{\partial\zeta}{\partial x} + v\frac{\partial\zeta}{\partial z} \text{ for } z = \zeta(x,y,t) \tag{2.13}$$

The second and third term are products of two very small values due to the assumption of small wave steepnesses in LWT, so these terms can be ignored. This linearised boundary condition therefore becomes:

$$\frac{\partial\Phi}{\partial z} = \frac{\partial\zeta}{\partial t} \text{ for } z = \zeta(x,t) \tag{2.14}$$

When these terms are rearranged and differentiated with respect to t, it results in the general free surface kinematic boundary condition, also known as the Cauchy-Poisson condition:

$$\frac{\partial\zeta}{\partial t} + \frac{1}{g}\cdot\frac{\partial^2\Phi_w}{\partial t^2} = 0 \tag{2.15}$$

4. **Free surface dynamic boundary condition.** The pressure at the free surface has to be equal to the atmospheric pressure. This ensures the wave is only subject to gravity, without influence from outside pressure from the atmosphere. From the continuity equation solved for its boundary condition, the Bernoulli equation in three dimensions follows as:

$$p + \rho g z + \frac{1}{2}\cdot\rho\left(u^2 + v^2 + w^2\right) = C \tag{2.16}$$

In which C is the Bernoulli constant. Rewriting this for the surface elevation ζ and substituting the velocities with the potential derivatives, this becomes:

$$\frac{\partial\Phi}{\partial t} + \frac{1}{2}\left[\left(\frac{\partial\phi}{\partial x}\right)^2 + \left(\frac{\partial\phi}{\partial y}\right)^2 + \left(\frac{\partial\phi}{\partial z}\right)^2\right] + g\cdot\zeta = f(t) \quad \text{for } z = \zeta(x,y,t) \tag{2.17}$$

Again, this can be linearised because the products of very small values are negligible, which results in the linearised equation [37]:

$$\frac{\partial\Phi}{\partial t} + y\cdot r = \int(l) \tag{2.18}$$

Potential flow theory requires viscosity to be neglected in order to be applicable. This causes issues down the road, especially when determining the rotational motions near the natural frequencies of the CSD in those motions. Viscous damping will therefore be added manually to the model.

2.1.2. Dispersion relation

Using potential theory, Eq. 2.9 can be substituted into the dynamic boundary condition of Eq. 2.18 to find the relation between the wave frequency ω and wave number k. This becomes the general dispersion relationship for any water depth [30]:

$$\omega^2 = gk \cdot tanh(kh) \tag{2.19}$$

In most practical cases the wave period will be known, but changes based on the position of the wave with respect to sea floor (this shoaling effect will be further explained in Section 2.1.5). This causes the wave number k to change accordingly, which needs to be determined iteratively using the dispersion relation. Simplifications can be made when waters are considered completely in the deep or shallow water range. For deep water ($tanh(kh) \approx 1$):

$$\omega^2 = gk \tag{2.20}$$

From this simplified dispersion relation, the deep water relation between the wave period T and the wavelength λ becomes:

$$T = \sqrt{\frac{2\pi}{g}} \cdot \sqrt{\lambda} \quad \text{or} \quad \lambda = \frac{g}{2\pi} \cdot T^2 \tag{2.21}$$

With substitution of the constants g and π:

$$T \approx 0.80 \cdot \sqrt{\lambda} \quad \text{or} \quad \lambda \approx 1.56 \cdot T^2 \tag{2.22}$$

Similarly, these relations can be simplified for shallow waters ($tanh(kh) \approx kh$):

$$\omega = k \cdot \sqrt{gh} \tag{2.23}$$

With the T and λ relation becoming:

$$T = \frac{\lambda}{\sqrt{gh}} \quad \text{or} \quad \lambda = T \cdot \sqrt{gh} \tag{2.24}$$

2.1.3. Water particle kinematics

As expressed in Eq. 2.9, the velocity potential Φ_w is the velocity of a water particle in three dimensions, integrated over the three directions x, y and z. The individual velocity components can therefore be retrieved by taking the derivative of the velocity potential over a singular direction. This results in the general expression of the velocity components u, v and w (x and y directions are considered to be equal for this section, so only u and w will be given) [10]:

$$u = \frac{\partial \Phi_w}{\partial x} = \frac{dx}{dt} = \zeta_a \frac{kg}{\omega} \cdot \frac{\cosh k(h+z)}{\cosh kh} \cdot \cos(kx - \omega t) \tag{2.25}$$

$$w = \frac{\partial \Phi_w}{\partial z} = \frac{dz}{dt} = \zeta_a \frac{kg}{\omega} \cdot \frac{\sinh k(h+z)}{\cosh kh} \cdot \sin(kx - \omega t) \tag{2.26}$$

Substituting the kg/ω term with the dispersion relation, the horizontal velocities and their shallow and deep water approximations are expressed as:

$$\begin{aligned} u &= \zeta_a \cdot \omega \cdot \frac{\cosh k(h+z)}{\sinh kh} \cdot \cos(kx - \omega t) \\ u &= \zeta_a \omega \cdot \frac{1}{kh} \cdot \cos(kx - \omega t) \quad \text{for shallow water} \\ u &= \zeta_a \omega \cdot e^k \cdot \cos(kx - \omega t) \quad \text{for deep water} \end{aligned} \tag{2.27}$$

And in the vertical z-direction:

$$\begin{aligned} w &= \zeta_a \cdot \omega \cdot \frac{\sinh k(h+z)}{\sinh kh} \cdot \sin(kx - \omega t) \\ w &= \zeta_a \omega \cdot \left(1 + \frac{z}{h}\right) \cdot \sin(kx - \omega t) \quad \text{for shallow water} \\ w &- \zeta_a \omega \cdot e^k \cdot \sin(kx - \omega t) \quad \text{for deep water} \end{aligned} \tag{2.28}$$

Because waves are propogations of energy in water without actually transporting water particles over distances, the trajectories of the velocity components describe an oscillating motion and always return to their original position. The precise shape of this motion is dependent on the influence of the sea floor on the wave. For deep waters this influence is negligible, resulting in a circular motion, as shown in Fig. 2.3 [37]. When approaching shallower conditions, the horizontal motion never disappears, even on the sea floor, resulting in an elliptical motion trajectory over the water depth. The water particle velocity is integrated over t to find the displacement:

$$x = \int_0^T \zeta_a \cdot \omega \cdot \frac{\cosh k(h+z)}{\sinh kh} \cdot \cos(kx - \omega t)\, dt = -\zeta_a \cdot \frac{\cosh k\,(h+z)}{\sinh kh} \cdot \sin\,(kx - \omega t) + C_1 \tag{2.29}$$

$$z = \int_0^T \zeta_a \cdot \omega \cdot \frac{\sinh k(h+z)}{\sinh kh} \cdot \sin(kx - \omega t)\, dt = +\zeta_a \cdot \frac{\sinh k\,(h+z)}{\sinh kh} \cdot \cos\,(kx - \omega t) + C_2 \tag{2.30}$$

Wherein C_1 and C_2 are constants denoting the starting position of the particle. Similarly, the water particle acceleration can be found from the derivative of the velocity with respect to time:

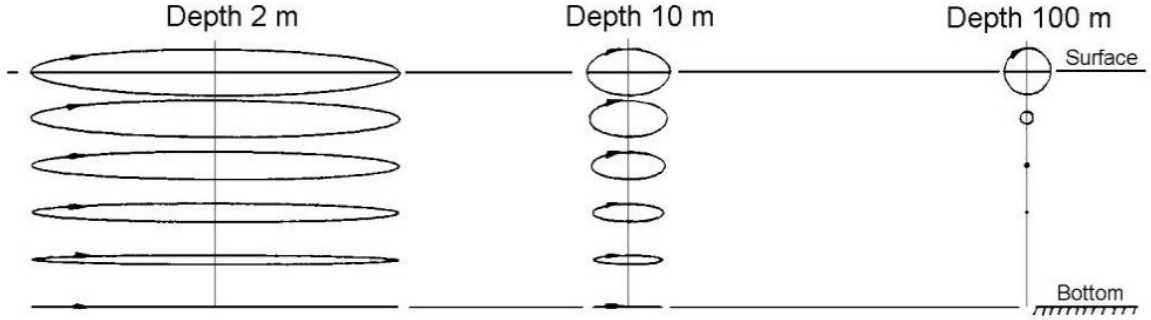

Figure 2.3: Trajectories of water particles in different water depths [37].

$$\dot{u} = +\zeta_a \cdot \omega^2 \cdot \frac{\cosh k(h+z)}{\sinh kh} \cdot \sin(kx - \omega t) \tag{2.31}$$

$$\dot{w} = -\zeta_a \cdot \omega^2 \cdot \frac{\sinh k(h+z)}{\sinh kh} \cdot \cos(kx - \omega t) \tag{2.32}$$

The acceleration can be simplified in deep waters ($kh \to \infty$) with the following equations:

$$\dot{u} = +\zeta_a \cdot \omega^2 \cdot e^{kz} \cdot \sin(kx - \omega t) \tag{2.33}$$

$$\dot{w} = -\zeta_a \cdot \omega^2 \cdot e^{kz} \cdot \cos(kx - \omega t) \tag{2.34}$$

2.1.4. Linear pressure

One of the main components of the force a wave exerts on a structure is determined by the pressure field it creates on the surface of the structure. In LWT, this pressure follows from the (linearised) Bernoulli equation as shown in Eq. 2.16. Combining this with the wave potential of Eq.2.9, the pressure is distributed as:

$$p = -\rho g z + \rho g \zeta_a \cdot \frac{\cosh k(h+z)}{\cosh kh} \cdot \cos(kx - \omega t) \tag{2.35}$$

In deep water, this can be approximated with a hydrostatic and a linearised hydrodynamic part [37]:

$$p = -\rho g z + \rho g \zeta_a \cdot e^{kz} \cdot \cos(kx - \omega t) \tag{2.36}$$

Where the amplitude of the dynamic pressure is $\rho g \zeta_a \cdot e^{kz}$. For shallow water this dynamic pressure component becomes zero, leaving only the hydrostatic pressure part for the shallow water depth:

$$p = -\rho g z + \rho g \zeta_a \cos(kx - \omega t) \tag{2.37}$$

2.1.5. Shoaling

When waves enter intermediate and shallow water depths when coming from deep water conditions, the seafloor starts affecting the orbital motion of the waves, as explained previously. This elliptical motion causes water particles to no longer return to their original position. Wavelengths shorten and the phase velocity of the waves decreases, which due to the continuity principle, result in larger crest heights. This continues until the wave reaches its breaking limit. To determine this shoaling effect on wave height, the energy flux in shallow and deep water is assumed to be equal [12, 37]. The shoaling coefficient K_s is given as:

$$\frac{H_{\text{shallow}}}{H_{\text{deep}}} = \sqrt{\frac{1}{\tanh\left(kh\left[1 + \frac{2kh}{\sinh 2kh}\right]\right)}} = K_s \tag{2.38}$$

The shoaling coefficient is a function of the wave number k and the water depth h, so according to the dispersion relation the shoaling effect will vary based on the wave numbers ω. The shoaling coefficient of multiple wave numbers is plotted in Fig 2.4. From Fig. 2.4 it can be seen that shoaling effects increase with smaller wave numbers (and thus decrease with smaller wave frequencies), and that the shoaling coefficient approaches 1 for deeper waters.

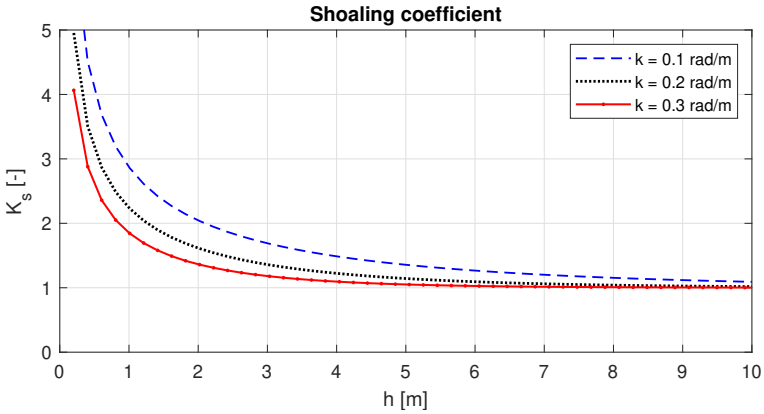

Figure 2.4: Shoaling coefficient K_s in varying wave numbers.

2.1.6. Wave breaking

Due to the increasing crest heights in shallow waters, waves reach their breaking limit earlier than in deep waters. The main cause for wave breaking is the water particle velocity exceeding the phase velocity of the wave at the crest. Wave breaking redistributes the available wave energy throughout the energy spectrum. Due to the phase velocity being correlated with the wavelength, the general wave breaking height H_b is given by [59]:

$$H_b = 0.14 \cdot \lambda \cdot \tanh\left(\frac{2\pi h}{\lambda}\right) \tag{2.39}$$

This breaking wave height provides an upper limit of the wave height in shallow waters. It is common practice to reduce Eq. 2.39 with the following estimate [14]:

$$H_b = 0.78 \cdot h \tag{2.40}$$

2.2. Non-linear wave theories

Real waves are never perfectly harmonic due to non-linearities caused by wave-wave interactions, shallow water effects and more. In LWT, this specifically means that waves have to adhere to the small wave steepness principle, where H/h and $S << 1$. To better approximate real waves, finite amplitude waves are considered where the wave height is no longer equally distributed over the crest and trough, as is the case in LWT. Furthermore, the amplitude of the wave is no longer considered insignificant with respect to the wavelength or the water depth. These considerations result in the wave height becoming a variable used to describe the theory in question, with no theory being universally applicable for all cases. This section will examine the most commonly used non-linear wave theories and their respective applicability range.

2.2.1. Stokes 2nd order theory

To better approximate a real wave shape, a correction is proposed to the expression of the harmonic wave, resulting in a steeper peak and shallower wave trough, as seen in Fig 2.5. This correction was proposed by Stokes [72], using a correction term representing the wave steepness, more commonly known as the dimensionless wave height $\epsilon = ka$ [23]. A single harmonic wave is then described as:

$$\zeta(x,t) = a\cos(\omega t - kx) = \varepsilon\zeta_1(x,t) \tag{2.41}$$

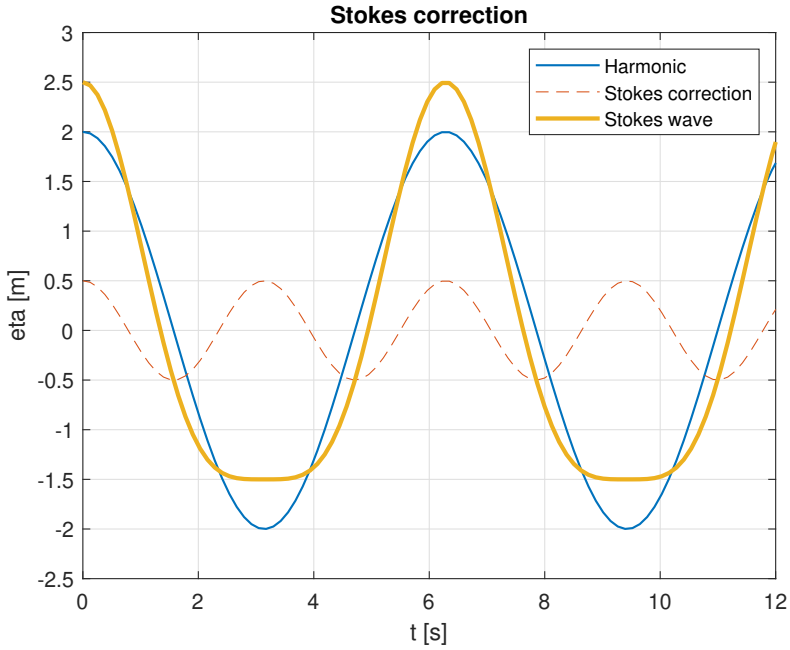

Figure 2.5: 2nd order Stokes correction of a harmonic wave.

Where $\zeta_1(x,t) = k^{-1}\cos(\omega t - kx)$. A perturbation technique is applied by adding an extra harmonic wave term with the steepness term squared:

$$\zeta(x,t) = \varepsilon\zeta_1(x,t) + \varepsilon^2\zeta_2(x,t) \tag{2.42}$$

From Eq. 2.42 it is easy to see how a higher order approximation can be constructed by adding more terms of higher order wave steepnesses and thus expanding this Taylor polynomial. Because the wave steepness is inherent to the description of the sea surface profile, the superposition principle is no longer valid. Additionally, this theory can only be used when wave amplitudes are still fairly small, compared to wavelength and water depth, it does however provide a description for the overall wave kinematics. Stokes theory generally holds for conditions with small ϵ and a small U_R, more on wave theory applicability and its parameters can be found in Section 2.2.7.
In Stokes theory, the boundary conditions for the velocity potential Φ change to accommodate the non-linearities. The Laplace equation and the seabed boundary condition remain the same as they are not order-dependent, however the free surface boundary conditions need to include the new sea surface profile. In Eq. 2.13 and 2.16, a second order term is added for Stokes 2$^{\text{nd}}$ order theory. The new free surface kinematic boundary condition becomes:

$$\frac{\partial^2\Phi_2}{\partial t^2} + g\cdot\frac{\partial\Phi_2}{\partial z} = -\zeta_1\frac{\partial}{\partial z}\left[\frac{\partial^2\Phi_2^2}{\partial t^2} + g\frac{\partial\Phi_1}{\partial z}\right] - \frac{\partial}{\partial t}\left[\left(\frac{\partial\Phi_1}{\partial x}\right)^2 + \left(\frac{\partial\Phi_1}{\partial z}\right)^2\right] \quad \text{at } z=0 \tag{2.43}$$

And the free surface dynamic boundary condition:

$$\zeta_2 = -\frac{1}{g}\left[\frac{\partial\Phi_2}{\partial t} + \zeta_1\frac{\partial^2\Phi_1}{\partial z\partial t} + \frac{1}{2}\left(\frac{\partial\Phi_1}{\partial x}\right)^2 + \frac{1}{2}\left(\frac{\partial\Phi_1}{\partial z}\right)^2\right] \quad \text{at } z=0 \tag{2.44}$$

If these four boundary conditions are implemented back into Eq. 2.42, we find the following expression for the wave potential [70]:

$$\Phi_w = \frac{\zeta_a g}{\omega}\frac{\cosh k(z+h)}{\cosh(kh)}\sin(kx-\omega t)+\frac{3}{g}\frac{\pi CH}{kT}\left(\frac{\pi H}{\lambda}\right)\cdot\frac{\cosh kh(z+h)}{\sinh^4 kh}\cdot\sin 2(kx-\omega t) \quad (2.45)$$

It is then assumed that the surface elevation can be approximated using an amplitude modulated wave [10, 30]:

$$\begin{aligned}\zeta &= \zeta_1 + \frac{1}{2}\cdot\zeta_a^2 \\ \zeta &= \zeta_a\cos(kx-\omega t)+\frac{\pi H^2}{8\lambda}\frac{\cosh kh}{\sinh^3 kh}\cdot[2+\cosh 2kh]\cdot\cos 2(kx-\omega t)\end{aligned} \quad (2.46)$$

As explained in Section 2.1.3, the water particle velocities are found by taking the potential derivative over their respective directions. Doing this for the new expression given in Eq. 2.45 results in the following velocities:

$$u = \frac{\pi H}{T}\cdot\frac{\cosh k(z+h)}{\sinh kh}\cdot\cos(kx-\omega t)+\frac{3(\pi H)^2}{4T\lambda}\cdot\frac{\cosh 2k(h+z)}{\sinh^4 kh}\cdot\cos 2(kx-\omega t) \quad (2.47)$$

$$w = \frac{\pi H}{T}\cdot\frac{\sinh k(z+h)}{\sinh kh}\cdot\sin(kx-\omega t)+\frac{3(\pi H)^2}{4T\lambda}\cdot\frac{\sinh 2k(h+z)}{\sinh^4 kh}\cdot\sin 2(kx-\omega t) \quad (2.48)$$

Most importantly for the application of this project, there is a key difference in the distribution of the wave energy in a non-linear wave compared to a regular wave. This energy transfer from the kinetic energy of a wave to the kinetic energy of the CSD is the driving force behind the CSD motion, so it is important to consider this. This effect has been documented by Dong et al. [19] as shown in Fig. 2.6. It shows that, especially for Stokes 2nd order waves, the wave energy can be increased by as much as 10% compared to LWT for higher wave steepnesses.

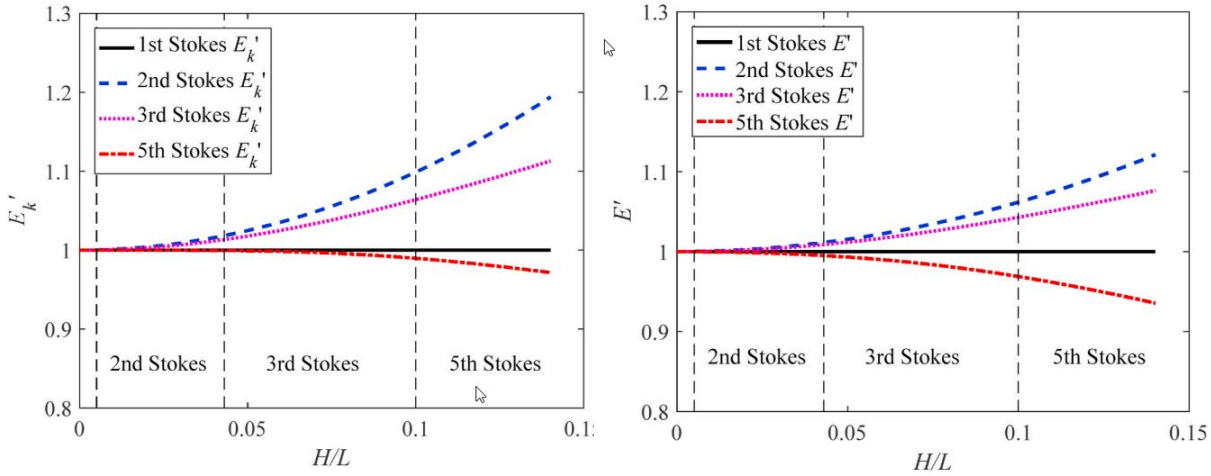

Figure 2.6: Kinetic wave energy (left) and total wave energy (right) of different Stokes theories for a range of wave steepnesses [19].

2.2.2. Non-linear pressure fields

Similarly to LWT, the non-linear pressure field is generated by combining the velocity potential of Eq. 2.45 into the Bernoulli equation of Eq. 2.16. It is defined without the hydrostatic pressure in a first-order component and a second-order component, where the first-order component is the same as linear pressure fields from Eq. 2.35 and dominates in the deep water regions of Stokes 2nd order theory. The shallower the water becomes, the larger the contribution of the second-order component will be [10]:

$$\begin{aligned} p_{dyn} =& \frac{3}{4}\rho g \frac{\pi H^2}{\lambda} \frac{1}{\sinh 2kh} \left[\frac{\cosh 2k(h+z)}{\sinh^2 kh} - \frac{1}{3} \right] \cos 2(kx - \omega t) \\ & - \frac{1}{4}\rho g \frac{\pi H^2}{\lambda} \frac{1}{\sinh kh} [\cosh 2k(h+z) - 1] \end{aligned} \tag{2.49}$$

2.2.3. Limits Stokes theory

The limits to non-linear theories are often described as functions of wave height, wave period and water depth. However, making comparisons between the applicability of these theories becomes much easier when considering dimensionless parameters, the three most important parameters being [30]:

- **Wave steepness.** As described in Section 2.1, the wave steepness S can be found as:

$$S = \frac{H}{\lambda} \tag{2.50}$$

- **Relative depth.** The relative depth μ is used to make the distinction between shallow, intermediate and deep water conditions. The influence of the sea floor on a wave is a function of the length of a wave with respect to the water depth:

$$\mu = \frac{h}{\lambda} \tag{2.51}$$

- **Ursell number.** As shown for LWT, waves have to have a small wave steepness for LWT to be applied correctly. However, waves with a small steepness can still be highly non-linear. To indicate this non-linearity, the Ursell number U_R is used, which is an empirical limit to which a wave is considered linear. It is expressed as:

$$U_R = \frac{H \cdot \lambda^2}{h^3} \tag{2.52}$$

These parameters will be used in Section 2.2.7 to determine the applicability and accuracy of the different non-linear theories in this project. In Stokes 2nd order theory, the dispersion relation given in Section 2.1.2 is still applicable. This relies on two criteria being met when using this theory. Firstly, the convergence criterion states that the correction terms applied to the harmonic wave expression are much smaller than unity [65]. Secondly, the so-called 'no bump' criterion ensures that no wave crest appears in the trough of the original wave profile. From Fig. 2.5 it is easy to see that if the amplitude of the correction wave becomes too great, the center of the trough will start to rise in elevation instead of simply flattening out. To better be able to state these limits, a maximum wave steepness is implemented. Stokes 2nd order theory is only valid for the trough being horizontal and not higher, or mathematically: the derivative of the surface elevation in the trough cannot exceed zero. This maximum S is described as:

$$S = \frac{\sinh^3 kh}{\pi \cosh(kh) \cdot (2 + \cosh 2kh))} \tag{2.53}$$

For deep water approximations ($kh \to \infty$), this limit approximates to $S = 1/7$.

2.2.4. Stokes 5th order waves

As seen in the previous chapter, Eq. 2.42 shows that Stokes waves are in theory infinitely expandable to include more steepness corrections. A common higher order technique especially for deep water with large wave heights is the Stokes 5th order wave theory. By including these extra correction terms it expands the applicability range of standard 2nd order Stokes theory, being valid for larger ranges of Ursell numbers and wave steepnesses [10]. Due to these terms it is especially well-suited for deep water wave analysis near the free surface. The velocity potential for this theory is:

$$\Phi = \frac{c}{k} \sum_{n=1}^{5} L \cosh nk(z+h) \sin n(kx - \omega t) \tag{2.54}$$

Where L is a function of kh and n is the number of total waves to be summed, in this case 5 as shown in Fig. 2.7. Due to the size of a CSD and the relatively small difference in wave profile compared to ordinary Stokes wave theory, the wave force difference for more than one correction wave is insignificant. Because the difference in so small, it can be argued that Stokes 5th order waves can become too complex and add unnecessary computing time with little benefit for the coastal conditions which a CSD operates in.

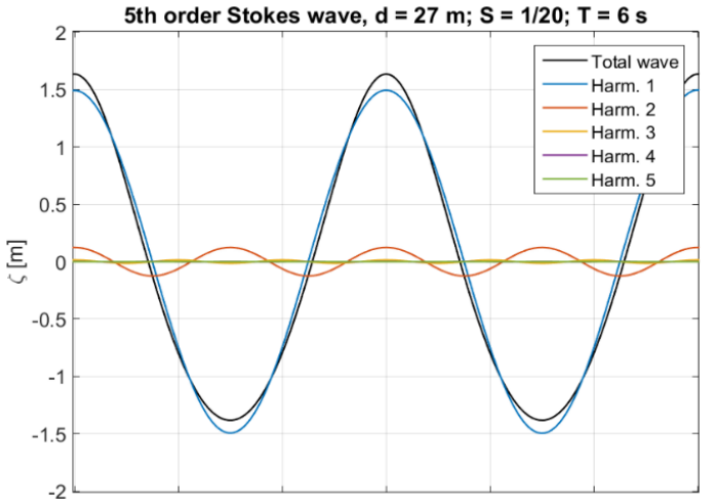

Figure 2.7: Stokes 5th order wave shape with four harmonic wave corrections [10].

2.2.5. Cnoidal waves

As shown, LWT or Stokes approximation are not valid for every possible sea state, therefore other theories can be considered to account for these conditions. Stokes in particular describes shallow water conditions better than LWT, but still breaks down when the relative depth becomes too small. For these cases, Cnoidal theory is often used, which is a better representation of shallow water waves, but not being very accurate in deep waters [30, 44]. Cnoidal waves are described as long, periodic and sharp crested. This inherent period is

based on the wavelength and the wave amplitude. As this wavelength becomes longer and the amplitude decreases, Cnoidal waves converge to linear regular waves as in Fig. 2.1.
In essence Cnoidal theory is based on the Korteweg-De Vries equation (KdV), first originated by Boussinesq [5] and expanded upon by Korteweg and de Vries [42]:

$$\frac{\partial \Phi}{\partial t} + \frac{\partial^3 \Phi}{\partial x^3} - 6\Phi \frac{\partial \Phi}{\partial x} = 0 \tag{2.55}$$

Cnoidal waves are the solution found of the KdV equation using Jacobi elliptic functions cn. The resulting surface profile is described by:

$$\zeta = \zeta_t + H cn^2 \left[2K\left(k_{cn}\right) \left(\frac{2\pi}{\lambda} - \frac{2\pi}{T} t \right), k_{cn} \right] \tag{2.56}$$

Where ζ_t is the surface elevation in the wave trough and K is a function of the elliptical integral of the wave particle motion. The applicability cases for these theories are very complicated to derive due to the use of the cn function and outside the scope of this paper, but in practice the Cnoidal theory is among the best approximations of very shallow water waves, when waves approach their breaking limit, as is shown by Wiegel [86] in Fig. 2.8. Wiegel shows that Cnoidal theory becomes the dominant theory with the best approximation of a real wave shape for H/h > 0.5 in shallow water. Cnoidal waves will eventually become solitary waves when the wavelength becomes infinitely long. In practice this is not a real case, as waves break before becoming truly solitary. Because of this reason solitary waves are not considered in this project.

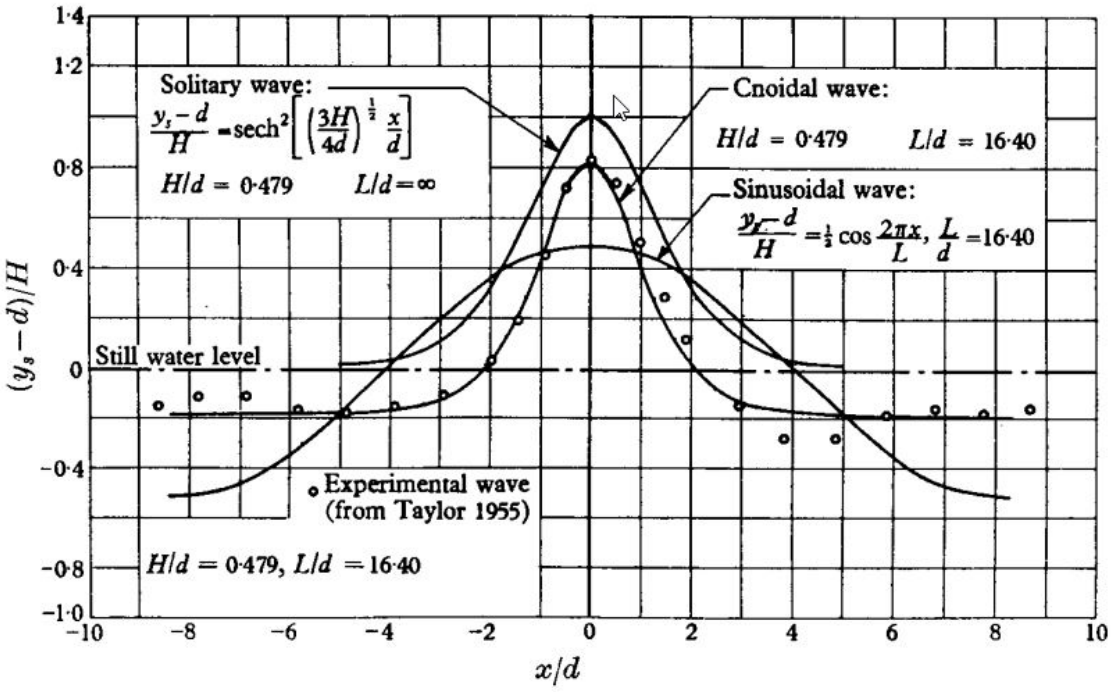

Figure 2.8: Comparison of a Cnoidal wave profile compared to a real wave in shallow water [86].

2.2.6. Dean's stream function

A completely different approach to wave modelling which in theory is useable in all conditions, is Dean's stream function waves theory [17]. It moves away from the velocity potential theory used in all of the above theories and instead implements a stream function Ψ, where the resulting streamlines in the water flow are of constant Ψ. By defining every stream line in this manner, with an arbitrary number of stream lines, a wave shape can be approximated numerically instead of the analytical theories using potential flow. Due to this numerical approach, it is very hard to use in design and the development of models in the time domain as many non-linear equations need to be solved to find the coefficients that describe the flow. This causes any models to become highly specific to that wave, as well as requiring heavy computing power. The advantage however, is a very high accuracy.

2.2.7. Applicability of wave theories

To identify the most accurate wave theory for any sea state or water depth, the parameters given in Section 2.2.3 can be used to find a series of dimensionless sea state parameters. Table 2.1 shows when the five given theories are valid. This is shown visually in Fig. 2.9 [44]. This figure shows that LWT is valid for a large portion of deep water waves, whereas very shallow water waves can almost always be approximated best with Cnoidal theory. Dean's stream functions are always valid, as they are purely numerical approximations of a wave profile. As such they can be used for every situation in theory, but practically this requires a lot of computing compared to analytical methods. All theories are affected by larger overarching non-linear effects, for instance shoaling and wave breaking limits, the latter explaining the absence of valid theories above the upper limit of H/h = 0.78 in Fig. 2.9.

Theory	S	μ	U_R
LWT	$\ll 1$	$\geq \frac{1}{20}$ or S/μ < 0.3	< 26
Stokes 2nd	< 0.04	$\frac{1}{10} < \mu < \frac{1}{7}$	26 < U_R < 40
Stokes 5th	< 0.14	$\frac{1}{10}$	< 40
Cnoidal	< 0.125	$\frac{1}{50} < \mu < \frac{1}{8}$	26 < U_R < 40
Dean	-	-	-

Table 2.1: Applicability ranges of non-linear wave theories.

2.3. Wave statistics

There are two distinct ways of describing wave climates: short-term wave statistics and long-term wave statistics. In the former, wave elevation is considered a stationary, Gaussian process [8]. This theory applies for shorter wave records of typically up to 30 minutes, but could be used to describe certain storm conditions of several hours as well. In the case of long-term wave statistics, records range from hours to multiple years. Due to this extended time frame, the record can no longer be described using any Gaussian models. Instead, the record is described by its extreme values in wave height, wavelength or zero-crossing wave period. For the scope of this thesis, mainly short term wave statistics will be considered, as the motions of the CSD need to be expressed in the time domain. Another important concept used in all wave statistics is the use of the random-phase/amplitude model. In this model, every uniformly distributed random phase is associated with a Rayleigh distributed amplitude. Because in practice sea states consist of a large range waves in different phases and frequencies, the

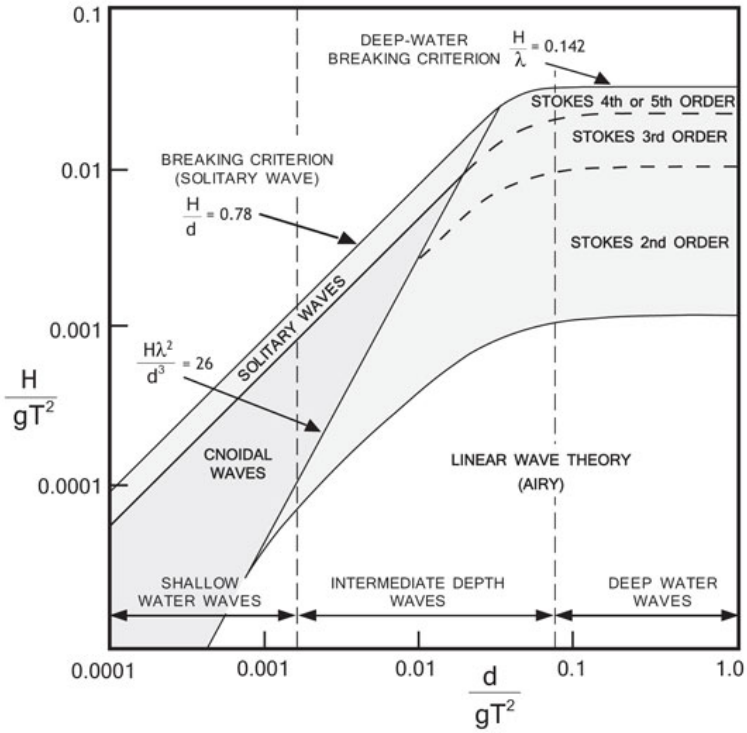

Figure 2.9: Different wave theories and their applicability ranges [44].

variance of the amplitude spectrum is distributed over a frequency interval $\Delta\omega_i$. When this interval approaches zero, the resulting spectrum is called the variance density spectrum $S(\omega)$:

$$E(\omega) = \lim_{\Delta\omega \to 0} \frac{1}{\Delta\omega} E\left\{\frac{1}{2}\underline{a}^2\right\} = S(\omega) \tag{2.57}$$

This variance density spectrum (statistically) contains all possible descriptions of the surface elevation ζ, if ζ is considered a stationary and Gaussian process.

2.3.1. Short-term wave statistics

Because it is considered a Gaussian process, the instantaneous sea-surface elevation in short-term wave statistics can be written as the following variance density function:

$$p(\zeta) = \frac{1}{(2\pi m_0)^{1/2}} \exp\left(-\frac{\zeta^2}{2m_0}\right) \tag{2.58}$$

In 2.58, m_0 denotes the zeroth-order moment, representing the variance of the probability density function of the sea-surface elevation ζ:

$$m_n = \int_0^\infty \omega^n S(\omega) \mathrm{d}\omega \quad \rightarrow S\left\{\underline{\zeta}^2\right\} = \int_0^\infty S(\omega)\mathrm{d}\omega = m_0 \quad \text{for } \mu_\zeta = S\{\underline{\zeta}\} = 0 \tag{2.59}$$

The density function representation of a wave record can be used to find a number of important parameters to describe a sea state. Based on the expression by Rice [37], the mean level crossing frequency can be found (as the inverse of the mean wave period T_ζ):

$$\omega_\zeta = \sqrt{\frac{m_2}{m_0}} \exp\left(-\frac{\zeta^2}{2m_0}\right) \tag{2.60}$$

Taking $\zeta = 0$, the mean zero-crossing frequency can be found:

$$\omega_0 = \sqrt{\frac{m_2}{m_0}} \tag{2.61}$$

For practical purposes, the significant wave period T_s is often based on empirical approximations. These are slightly different based on the source of the wave generation [25]:

$$T_s \approx T_{peak} \quad \text{for swell} \tag{2.62}$$
$$T_s \approx 0.95 T_{peak} \quad \text{for wind sea} \tag{2.63}$$

Similarly, the wave height can be described in terms of the moments of the probability density function of the surface elevation. This is useful especially when considering the probability of exceedance of a certain surface elevation, which is formed from combining equations 2.60 and 2.61:

$$\mathsf{p}\left\{\zeta_{crest} > \zeta\right\} = \frac{\omega_\zeta}{\omega_0} = \frac{\sqrt{\frac{m_2}{m_0}}\,\mathsf{exp}\left(-\frac{\zeta^2}{2m_0}\right)}{\sqrt{\frac{m_2}{m_0}}} = \mathsf{exp}\left(-\frac{\zeta^2}{2m_0}\right) \tag{2.64}$$

Given that the wave height is Rayleigh distributed [30], and the significant wave height is expressed as the lower limit of the highest $1/3$ of waves in the wave record, such that the probability of a wave being equal or larger than the significant wave height is:

$$\int_{H_s}^{\infty} p(H)\mathsf{d}H = \frac{1}{3} \tag{2.65}$$

Substituting this equation into a Rayleigh distribution gives the significant wave height H_{m0} in terms of the variance density spectrum:

$$H_{m_0} \approx 4\sqrt{m_0} \tag{2.66}$$

There is a noticeable difference between the value of significant wave height H_{m0} when gathered from statistics like shown above and from visible inspection of waves ($H_{1/3}$), where H_{m0} tends to be 5-10% higher than $H_{1/3}$. This report assumes H_{m0} to be the most accurate manner of determining H_s.

2.3.2. Long-term wave statistics

As mentioned before, long-term wave statistics are based on wave records spanning multiple years, and are therefore not as useful when considering a time domain analysis of ship motions. However, it is good to discuss the differences found in waves in coastal conditions around the world. Long-term wave statistics for this project will be based on determining the main outcome of Eq. 2.64: when is a certain limiting wave height exceeded for a particular operation site. To achieve this, all bodies of water across the globe are divided into areas with similar conditions [29], as shown in Fig. 2.10 [56]. For one of these areas, characteristic wave data can be combined to find the probability of a wave with a certain wave height and wavelength occurring for an arbitrary wave record. This wave scatter diagram is then used as an easy indication of a wave distribution, where the probability of exceedance is simply the number of observations of that particular cell over the total number of observations, as shown in Fig. 2.11.

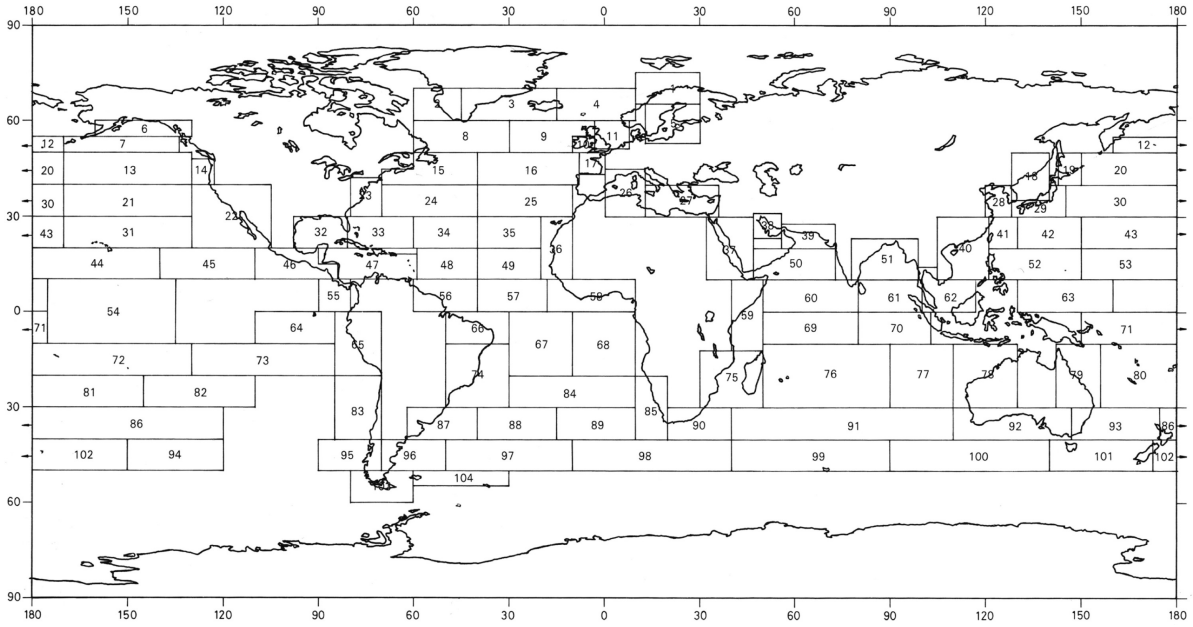

Figure 2.10: Zone division of seas and oceans [56].

	T_2 (s)											
H_s (m)	3.5	4.5	5.5	6.5	7.5	8.5	9.5	10.5	11.5	12.5	13.5	Total
14.5	0	0	0	0	2	30	154	362	466	370	202	1586
13.5	0	0	0	0	3	33	145	293	322	219	101	1116
12.5	0	0	0	0	7	72	289	539	548	345	149	1949
11.5	0	0	0	0	17	160	585	996	931	543	217	3449
10.5	0	0	0	1	41	363	1200	1852	1579	843	310	6189
9.5	0	0	0	4	109	845	2485	3443	2648	1283	432	11249
8.5	0	0	0	12	295	1996	5157	6323	4333	1882	572	20570
7.5	0	0	0	41	818	4723	10537	11242	6755	2594	703	37413
6.5	0	0	1	138	2273	10967	20620	18718	9665	3222	767	66371
5.5	0	0	7	471	6187	24075	36940	27702	11969	3387	694	111432
4.5	0	0	31	1586	15757	47075	56347	33539	11710	2731	471	169244
3.5	0	0	148	5017	34720	74007	64809	28964	7804	1444	202	217115
2.5	0	4	681	13441	56847	77259	45013	13962	2725	381	41	210354
1.5	0	40	2699	23284	47839	34532	11554	2208	282	27	2	122467
0.5	5	350	3314	8131	5858	1598	216	18	1	0	0	19491
Total	5	394	6881	52126	170773	277732	256051	150161	61738	19271	4863	999995

Figure 2.11: Example of a wave scatter diagram for area 9 during a winter [29, 37].

2.4. Wave spectra

General wave spectra are an adequate way to approximate the energy distribution in a certain geographical location, however they are never perfectly accurate. Even in locations that seem to be experiencing relatively simple meteorological conditions, the resulting wave spectrum can still be complex based on the surrounding geography and seasonal characteristics. In the most simplified version, a wave spectrum is a function of the significant wave height H_s and the average wave period $\bar{T}$:

$$S_\zeta(\omega) = {H_s}^2 \cdot f(\omega, \bar{T}) \tag{2.67}$$

One of the most widely applicable of these was established by Bretschneider [6]:

$$S_\zeta(\omega) = \frac{173 \cdot H_s^2}{T_1^4} \cdot \omega^{-5} \cdot \exp\left\{\frac{-692}{T_1^4} \cdot \omega^{-4}\right\} \tag{2.68}$$

The Bretschneider Spectrum (BS) is most suited for open, fully-developed seas where the waves are no longer influenced by the fetch distance. This spectrum is based on a more general spectrum put forth by Pierson and Moskowitz [61]. BS is therefore also referred to as a Modified Two-Parameter Pierson-Moskowitz Wave Spectrum. The original Pierson-Moskowitz spectrum expression can be found by implementing the following relation to eliminate the period from Eq. 2.68 [37]:

$$T_1 = 3.86 \cdot \sqrt{H_s} \quad \text{and} \quad T_2 = 3.56 \cdot \sqrt{H_s} \tag{2.69}$$

In reality, the wave spectrum is rarely the same for two different seas, based on their environmental conditions, geometry, etc. The assumption of fully-developed seas used in earlier wave spectra works for a lot of large bodies of water with little variation in wind conditions. However, especially when coastal conditions are concerned, the waves are mostly fetch-limited and not fully developed. The Joint North Sea Wave Project (JONSWAP) was carried out to better approximate real wave spectra near-shore. It is defined as follows [28]:

$$S_\zeta(\omega) = \frac{320 \cdot H_s^2}{T_p^4} \cdot \omega^{-5} \cdot \exp\left\{\frac{-1950}{T_p^4} \cdot \omega^{-4}\right\} \cdot \gamma^A \tag{2.70}$$

Fig. 2.12 shows the comparison between a Bretschneider and a JONSWAP spectrum. The JONSWAP spectrum clearly favours lower wave frequencies, which is in accordance with the theory from Hasselmann [27], where waves start interacting with one another, producing longer waves. Energy from short waves gets transferred to lower frequencies, explaining the larger peak in JONSWAP compared to Bretschneider at low wave frequencies.

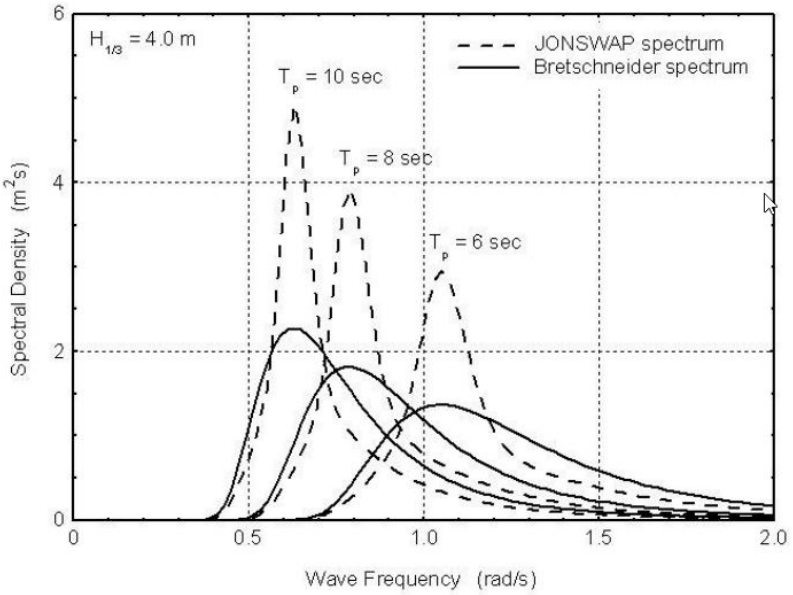

Figure 2.12: Comparison of JONSWAP and PM-spectra [37].

2.4.1. Directional spreading

A wave spectrum accounts for variation in wave period and wave height, but each wave spectrum is subject to a distribution over the wave direction, centered around its dominant wave direction. A good approximation for this spreading can be found using the cosine-squared rule [37]:

$$S_\zeta(\omega, \mu) = \left\{ \frac{2}{\pi} \cdot \cos^2(\mu - \bar{\mu}) \right\} \cdot S_\zeta(\omega) \tag{2.71}$$

A comparison between an actual directional spectrum and the approximation in Eq. 2.71 is shown in Fig. 2.13 [20, 37]. There is some difference at the outer edges of the spectrum in particular, but around the most prominent direction the distribution is accurate. For the purpose of this project the largest forces are found in the main wave direction, meaning the force output in this one direction is almost always accompanied by smaller wave forces in similar directions. To account for this, the response of the model will be determined across all 360° wave directions.

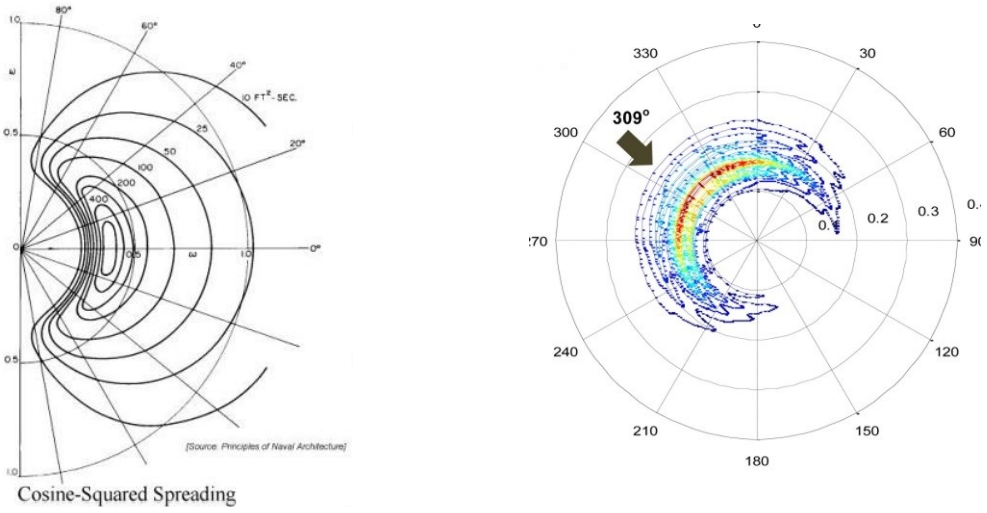

Figure 2.13: Cosine-squared approximation compared to measured directional data [20, 37].

2.5. Currents and wind

Currents are responsible for large steady forces on floating structures and are the main driving force behind the steady-state solution for displacements in the time domain. Due to the large underwater side area of the CSD especially in beam seas, currents can place large forces on positioning elements such as the spud, but also the swing wires. Similarly, wind forces in combination with currents and waves can put a large amount of stress on vital mechanical components of a CSD and cause unforeseen forces in normal operation. This section aims to explore the order of magnitude of these forces and its effect on different components of a CSD. Furthermore, the case to be used in upcoming model analysis is explained. A number of typical values is given to analyse the orders of magnitude of these forces. The wave records considered in this project are very short, where it can be assumed that currents and winds do not change significantly. Therefore, current and wind speed and their respective forces on the CSD are assumed to be constant.

2.5.1. Current forces on floating structures

To determine current forces near the sea surface, naturally only projected areas below SWL are considered. These areas include the diffracting parts of the spud, the pontoon and the entire cutter ladder as its considered completely submerged in operational conditions.

$$F_{curr} = \frac{1}{2} C_D \cdot \rho_w \cdot A_S \cdot u_{curr}^2 \tag{2.72}$$

In which u_{curr} is the current velocity at the surface, as expressed in Eq. 2.75 and A is the area projected to the incoming current. For the use of this project the resulting current forces have to be decoupled into their directional component with $c_n(\alpha)$ is a coefficient based on the drag coefficient and the incoming angle of the current α, taken from the stern [40]:

$$\begin{aligned} F_{curr,X,Y} &= \frac{1}{2} \cdot \rho_w \cdot \sqrt{L^2 + B^2} \cdot T \cdot u_{curr}^2 c_{x,y}(\alpha) \\ F_{curr,\psi} &= \frac{3}{5} \cdot \rho_w \cdot B \cdot T \cdot u_{curr}^2 \cos \alpha \end{aligned} \tag{2.73}$$

2.5.2. Current forces on bottom-founded components

Due to the friction of water with the seabed, current velocity is never truly constant over the entire water depth. The height to which the current is influenced by the sea floor is commonly referred to as the boundary layer thickness. In deep water conditions with slow current velocities, this boundary layer occupies only a small portion of the total water depth, just above the seabed. However, when shallow waters are considered and the current velocity increases, the boundary layer can cover the complete depth from the sea floor to the sea surface. This creates a velocity profile over any structure that is connected to the seabed, and in turn results in a varying current force over the depth. An approximation is proposed that is applicable in most situations, where the boundary layer covers half the water depth [45]:

$$u_z = \left(\frac{z}{0.32h}\right)^{1/7} \bar{u} \quad \text{for } 0 \leq z \leq 0.5h \tag{2.74}$$

$$u_z = 1.07\bar{u} \quad \text{for } 0.5h \leq z \leq h \tag{2.75}$$

In which, $\bar{u}$ denotes the average current speed. The actual current speed can then be iterated over water depth with Eq. 2.72 to find the total current force. For the CSD system this only truly affects the spud and the cutter ladder, as in operation they reach the seabed, the pontoon current forces can be estimated with Eq. 2.72.

2.5.3. Wind

It is argued that wind forces are relatively small for most vessels, especially compared to current and wave forces. However, due to the fact wind is one of the main driving forces behind wave generation, high wave loads are almost always paired with high wind loads. Practical operability and downtime analysis therefore always has to include wind force analysis. Wind forces are calculated in very much the same fashion as current forces, but for the projected areas above SWL:

$$F_{wind} = \frac{1}{2} \rho_{air} \cdot v_{wind}^2 \cdot C_{d,wind} \cdot A_{top} \tag{2.76}$$

To be able to check the impact of these forces, a practical example is considered of real current and wind data taken in the IJgeul, situated outside the Nieuwe Buitenhaven in IJmuiden, the Netherlands [53, 54]. The resulting current and wind speed found between April 12th and 14th

2022 are shown in Fig. 2.14. Mean wind and current speed for the North Sea area are found as 7.8 m/s and 0.46 m/s respectively [13, 76]. To be conservative in this analysis, a practical operating scenario is chosen for a sea state with $v_{wind} = 10$ m/s and $v_{curr} = 0.5$ m/s. Due to the short nature of the wave records used in the time domain model, it can be assumed that the current and wind speed remain constant for the duration.

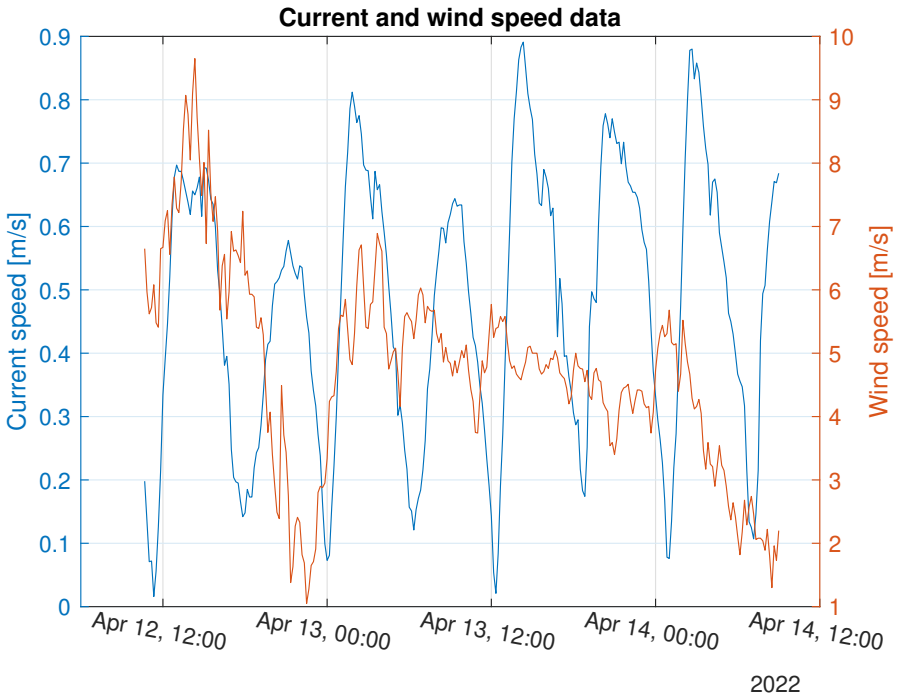

Figure 2.14: Current and wind speed data of the IJgeul [53, 54].

2.6. Model case study

In summary, including all the aspects presented in this chapter, a single case is chosen to represent the different possible operational conditions of a CSD. The complete range of allowable working depths of the CSD will be used. 5 m was deemed a safe minimum dredging depth for the CSD700, using the rules of thumb that a minimum bottom clearance of 1 m is required for operation, as well as a minimum angle of the cutter ladder with the bottom of 5° [78]. Phenomena such as spud resonance are crucial to determine structural response, so the range of water depths will be checked in increments of 1 m, up to the maximum dredging depth of 25 m.

For the sake of presenting a real-world example, wave, current, and wind data are taken for the Dutch coast of the North Sea, or area 11 in Fig. 2.10. Table 2.2 shows the most probable wave period T_2 in this area, ranging from 3 seconds to 12 seconds. An extra assessment of general wave periods is retrieved from the GWS data [29] and shown in Fig. 2.15, further reinforcing that waves longer than 12 seconds are unlikely to appear in the project area. These values are therefore taken to assess operability in the time domain model. As almost all significant wave heights are present throughout the wave scatter diagram, all wave heights up to 2.5 m will be taken into account. Waves higher than 2.5 m are highly likely to be outside the operability range and are therefore beyond the scope of this analysis [77].

	T_2 [s]											
H_s [m]	3.5	4.5	505.5	6.5	7.5	8.5	9.5	10.5	11.5	12.5	13.5	Total
13.5												0
12.5												0
11.5												0
10.5												0
9.5					1							1
8.5				1	1	1						3
7.5		1	2	2	1							6
6.5		2	4	4	2	1						13
5.5		1	4	9	8	4	1					27
4.5		2	11	19	15	6	2					55
3.5		6	27	39	26	10	3	1				112
2.5	1	17	63	74	40	13	3	1				212
1.5	3	48	151	100	40	10	2					324
0.5	18	86	95	42	10	2						253
Total	22	160	324	290	147	49	12	2	0	0	0	1006

Table 2.2: Wave scatter diagram for the project area [29].

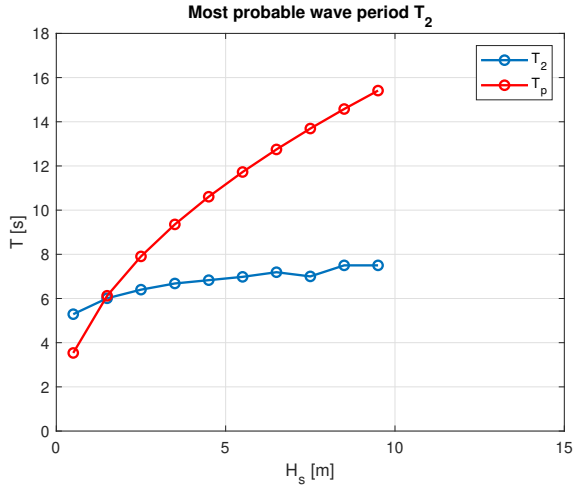

Figure 2.15: Most probable zero-crossing period T_2 and peak period T_p.

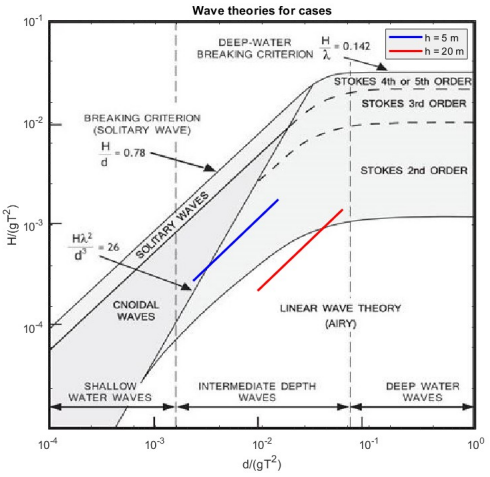

Figure 2.16: Validity of wave theories for the given cases.

The appropriate wave theories for these conditions are shown in Fig. 2.16, with the blue line indicating all relevant wave periods for 5 m water depth, and the red line for 25 m water depth. As can be seen in Fig 2.16, the shallow water depth bound is completely describable by Stokes 2nd order wave theory, with Cnoidal theory and Stokes theory overlapping for the given relative depths. For all wave periods, LWT can be assumed from a depth of 18 m onward. For these larger water depths, the Stokes correction wave has a negligible amplitude. Sea floor influence on the wave height due to shoaling is present from 10 m water depth, increasing for smaller wave numbers.

For the time domain model involving a full wave spectrum, a JONSWAP spectrum is used with peak enhancement factor γ of 3.3, as is appropriate for wave climates in the North Sea. This translates to the spectral energy distributions found for different peak periods shown in Fig. 2.17. Moving forward, whenever specific data is needed to provide an example of model input, data will be taken from the North Sea coast.

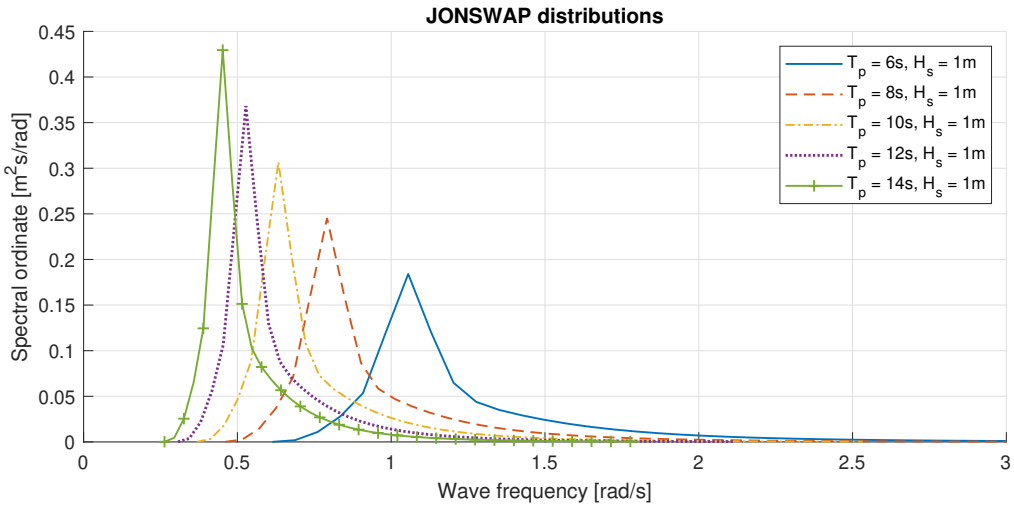

Figure 2.17: Energy distributions in different JONSWAP spectra.

3

Soil interaction

The main failure mechanism that differentiates CSDs from other ships and floating structures is the connection with the soil through the spud. The spud itself is a fairly simple construction with known motions and displacement or shear force distribution, however modelling the connection with the soil and the effect on the overall response of the CSD is less known. Due to the nature of soil parameters and their unpredictability, as well as the wide range in which the CSD operates, it becomes very difficult to find a general model which covers all these possible operating conditions. Similar studies have been done in other fields in offshore engineering, including the response of monopiles and spud-piled jack-up structures to environmental forces in different soils. Key differences with a CSD however are the means of installation: where normal piled structures are forcibly piled to a desired depth, CSD spuds are dropped into the soil and will reach different depths depending on the soil they are in and the height they are dropped from. This penetration depth can very much change the maximum reaction force the soil is able to exert. Secondly, due to the varying water depths encountered in operation, the effective length of the spud changes and with that change the maximum hydrodynamic force capacity of the CSD.

This chapter aims to establish two important aspects of an accurate spud-soil model: a representation of real operating conditions including spud penetration depth and the resulting spud and soil stiffness, all resulting in a new way of modelling the spud-soil interaction. Furthermore, secondary boundary conditions involving soil interaction are investigated, consisting of a representation of the cutter forces and the stiffness acquired from the swing wires.

3.1. Preliminary soil study

A CSD can cut a wide range of soil, but for the sake of this model medium-dense sand will be analysed as the dominant soil type, partly due to previous in-depth research done by Damen and TU Delft on the cyclic lateral loading of spuds in sand. This section will follow the parameters set forth by Sitanggang [68], as these values are verified by geo-centrifuge experiments using the beam centrifuge facility at TU Delft. The soil parameters found are crucial for both the cutter forces acting upon the cutter head, as well as the loading capacities of the soil holding the spud. The soil chosen is one found commonly around the Netherlands: a medium-dense sand and silt mix (relative density D_r = 65%) present in rivers and near the coast. Due to the multitude of environmental conditions a CSD has to operate in, varying this soil is an important part of validating the spud response to hydrodynamic loading and the possibility of soil failure. However, as this project aims to compare flexible spud keeper designs, the soil parameters

will remain constant to prevent any needless variables which could make the model output overly complex. Secondly, soil can be highly non-linear, especially when considering deeper penetration depths of the spud. Real conditions often involve multiple soil types, layers and a change in soil parameters over the depth. The assumption is made that the penetration depths found in Section 3.2 are too small to consider these non-linearities and all parameters are constant over the depth. In summary, the soil parameters are given in Table 3.1 [22, 35].

Symbol	Description	Value	Unit
ϕ'	Effective soil stress friction angle	28	[°]
ϕ'_a	Angle of internal friction between spud and soil	21	[°]
γ_s	Saturated unit weight	20.0	[kN/m^3]
γ'	Effective unit weight	9.94	[kN/m^3]
v_s	Poisson's ratio soil	0.3	[-]
E_s	Young's modulus soil	30.0	[MPa]
G_s	Shear modulus soil	11.54	[MPa]
h_c	Cone height spud	1.0	[m]
m	Mass spud	15000	[kg]
r	Radius spud	0.507	[m]

Table 3.1: Soil parameters for medium-dense sand [22, 35].

From these parameters the variables needed to find the bearing capacity can be found [47]. Important to include is Rankine's coefficient of passive earth pressure, a measure of the horizontal pressure exerted by the soil to counter lateral loads, depending on the geometry of the object which in this case is the spud [66]:

$$K_p = \frac{1 + sin(\phi')}{1 - sin(\phi')} = 2.769 \tag{3.1}$$

3.2. Spud penetration depth

An important parameter determining the fixity of the spud in the soil is the total penetration depth of the spud into the ground. Due to the varying operating conditions that the CSD can be used in, this penetration depth varies largely over different soil types and water depths. This can have major effects on the validity of a spud-soil model. As discussed in Section 1.1, the spud is dropped from a set position with respect to the CSD pontoon and only subject to its own gravitational force and buoyancy when entering the soil, as shown in Fig. 3.1. For the purposes of these estimations the frictional forces inside the guiding components of the spud carriage are considered negligible. To find the spud penetration depth, the method of Sitanggang [68] found during a previous Damen study on spud anchoring is used. It relies on an energy balance approach where the kinetic energy of the spud when it hits the soil has to equal to a function of the specific soil stiffness and the penetration depth of the spud. This kinetic and potential energy is partly dissipated through the impact with the water surface if the spud is dropped from above SWL and through drag forces of the water. To account for this a correction factor α_d is proposed and empirically calculated for this reduction in drop efficiency, taken as 0.77. These functions are given in Eq. 3.2:

$$E_{kin} = R_u \cdot L_{pen} = \alpha_d \cdot m \cdot g \cdot \Delta h \tag{3.2}$$

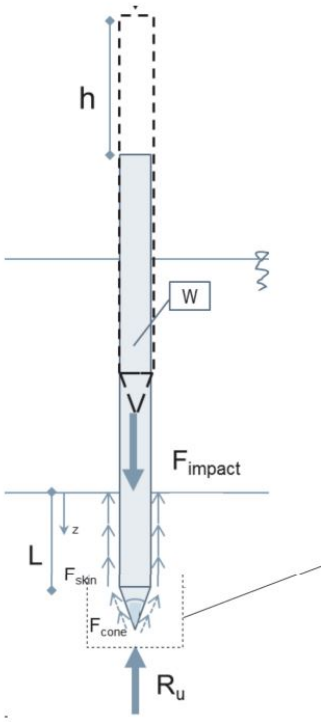

Figure 3.1: Spud dropping process [68].

For:

$$\begin{aligned} E_{kin} &= \text{kinetic energy of the spud upon contact with the soil,} \\ R_u &= \text{modified soil resistance,} \\ L_{pen} &= \text{penetration depth,} \\ \Delta h &= \text{spud dropping height.} \end{aligned}$$

The modified soil resistance R_u is dependent on the friction forces resulting from the cone and skin friction of the spud. These forces are given in Eq. 3.4 and 3.5:

$$R_u = F_{skin} + F_{cone} \tag{3.3}$$

$$F_{\text{skin}} = C_{spud} \cdot \int_0^{L_{pen}} \sigma'_{\text{v}} K_{\text{p}} \tan(\phi'_{\text{a}}) dz \tag{3.4}$$

$$F_{\text{cone}} = A_{\text{cone}} \cdot \sigma'_{\text{vb}} K_{\text{p}} \tan(\phi'_{\text{a}}) \cdot \cos^2(\omega) \tag{3.5}$$

Eq. 3.4 is integrated over the penetration depth and both Eqs 3.4 and 3.5 are substituted back into Eq. 3.2. This results in the following function with only the penetration depth as unknown variable:

$$\left[\left(2\pi r \cdot \frac{1}{2} \gamma' L_{pen}^3 \right) + \left(\gamma' L_{pen}^2 \cdot \pi r \frac{\left(h_c^2 + r^2\right)^{1.5}}{h_c^2} \right) \right] K_{\text{p}} \tan \phi'_{\text{a}} = \alpha_d \cdot m \cdot g \cdot \Delta h \tag{3.6}$$

The real roots of the polynomial in Eq. 3.6 result in the penetration depth of the spud for the respective dropping height Δh measured from the sea floor. Varying the dropping height

results in a distribution of the penetration depth over the dropping height, as shown in Fig. 3.2. In theory, the dropping height can be increased to the maximum height a spud can be hoisted up from the CSD, all the way to the sea floor. However, in practice this obviously would result in very high dropping heights in deep waters, requiring long hoisting times and a variety of problems with forces on the spud carriage and overly deep spud penetration. In the majority of cases the spud cone is not lifted out of the water at all, but instead hoisted for one 'stroke' of 3 meters to minimise the downtime during the moving of the spud. This means the total sum of the penetration depth and dropping height are 3 meters. A CSD has the option to perform multiple strokes in the event of very hard and dense soil to increase the penetration depth, but for this case only one stroke is considered. From Fig. 3.2 it can be seen that a dropping height of 0.85 m results in 2.13 m penetration depth (marked with red x). This will be used as the design penetration depth going forward.

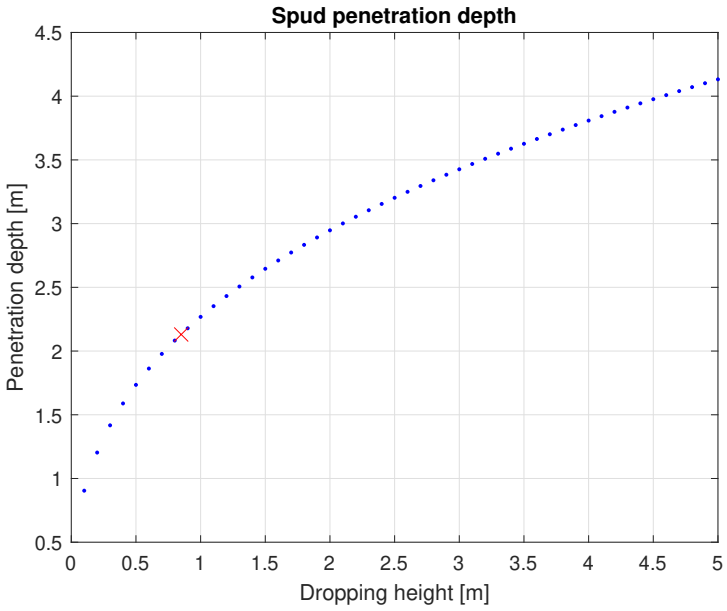

Figure 3.2: Spud penetration depths for spud diameter of 1014 mm in sand.

3.3. Spud-soil interaction

Many approaches exist to model a pile in soil, however the validity of these models are questionable for the situation of a spud with a fairly shallow penetration depth. The by definition temporary nature of the CSD's spud means most approximations used for permanent monopiles or jack-up installations cannot be used, such as the effective pile fixation depth at six times the diameter or the effective hinge point at three times the diameter below the mudline [80]. Therefore to establish a valid model approximation, the deflection and horizontal bearing capacity need to be solved. For this purpose the spud and its soil interaction is assumed to behave like a cylindrical semi-rough steel member under short-term, cyclic, predominantly lateral loads in an isotropic and homogeneous soil. Soil parameters still apply as stated in Table 3.1. Additional information on soil properties is given in Appendix B.

The p-y method as described in the API: Recommended Practice for Geotechnical Engineering (ISO 19901-4) [35] is the most commonly used method of describing a pile and its deflections when interacting with the surrounding soil. Also referred to as the Winkler method, the pile is modelled as multiple beam elements connected to each other by springs with a stiffness based on the flexural stiffness of the pile itself. These beam elements are then connected to

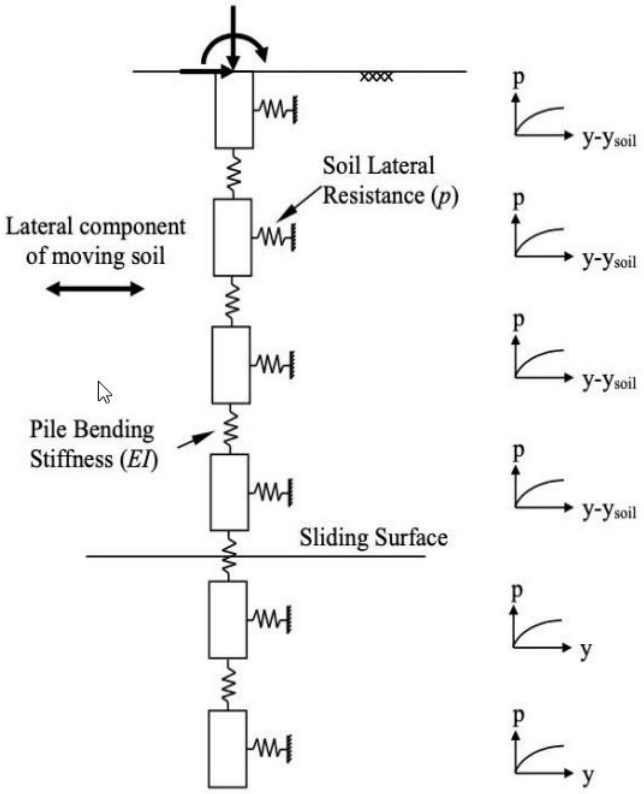

Figure 3.3: Winkler method of pile deflection using p-y curves [33].

the soil with a series of uncoupled non-linear springs along the length of the pile to represent the soil's lateral stiffness, as shown in Fig. 3.3. From the resulting soil reaction p the deflection y can be obtained with:

$$p_u = (C_1 z + C_2 D)\,\gamma' z \tag{3.7}$$

For:

$$C_1 = \frac{(\tan\beta)^2 \tan\alpha}{\tan(\beta - \phi')} + K_o \times \left[\frac{\tan\phi' \cdot \sin\beta}{\cos\alpha \times \tan(\beta - \phi')} + \tan\beta \cdot \left(\tan\phi' \cdot \sin\beta - \tan\alpha\right)\right] \tag{3.8}$$

$$C_2 = \frac{\tan\beta}{\tan(\beta - \phi^\circ)} - K_p \tag{3.9}$$

This method however was designed for long, slender piles with a large penetration depth compared to its diameter, commonly D < 1 m and L/D > 20 [35]. As shown in Section 3.2, penetration depths for CSDs are minimal, with the L/D unlikely to exceed values much higher than 2. A side-effect of the geometry below the mudline is the differences in the force response. Where a slender pile under lateral load will almost completely resist the force through bending of the pile, short and wide piles can almost be considered rigid elements and will move laterally without any noticeable bending. Experiments with shallow monopile installations show this rigid body rotation which can no longer be modelled using the API p-y curve method [11, 64]. Instead a new approach is proposed by Wang et al. [81], where the spud is constrained by a hinge and a rotational spring placed at 0.75 times the penetration depth, as shown in Fig. 3.4.

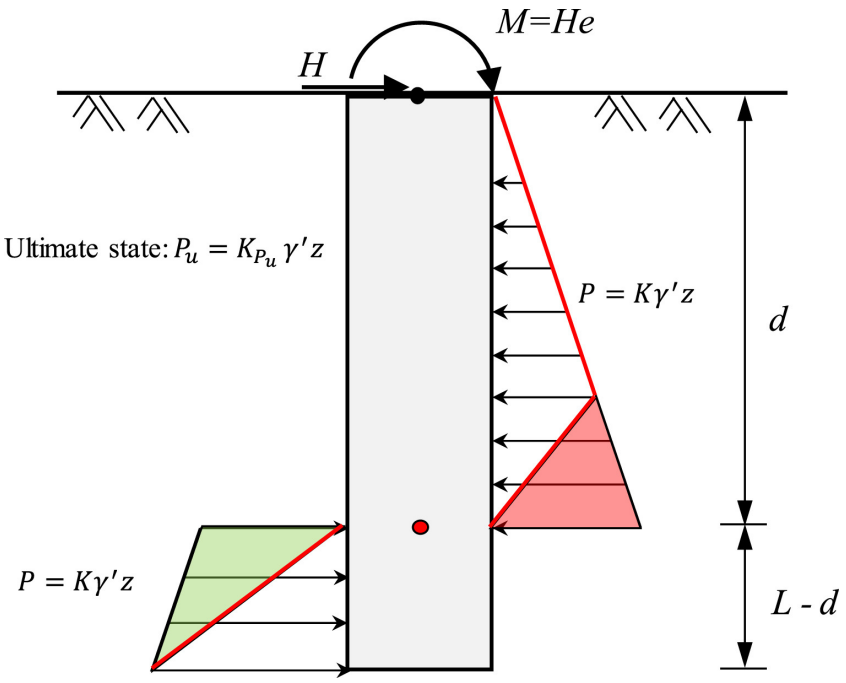

Figure 3.4: Rotational spring method proposed by Wang et al. [81].

This method originates from previous experiments [60, 82] with FEM analysis and physical testing which provide empirical formulations for the resulting deflections at the mudline. From these deflections the ultimate lateral soil pressure P_u can be calculated with $P_u = p_u/D$ for different pile diameters D. p_u is derived similarly to the p-y curve, as given in Eq. 3.7. From these experiments it was found that the point of rotation was always located between 0.7L and 0.8L, averaging out at 0.75L. Using this expression for d in Fig. 3.4, the ultimate lateral capacity H_{ult} and the ultimate moment capacity M_{ult} of the soil can be calculated:

$$H_{ult} = \left(d^2 - \frac{1}{2}L_{pen}^2\right) K_{P_u} D\gamma' = \left((d/L_{pen})^2 - \frac{1}{2}\right) K_{P_u} D L_{pen}^2 \gamma' \tag{3.10}$$

$$M_{ult} = H_{ult} \cdot (e+d) = \frac{\left(L_{pen}^3 - 2d^3\right) K_{P_v} D\gamma'}{3} = \frac{\left(1 - 2(d/L_{pen})^3\right) K_{P_u} D L_{pen}^3 \gamma'}{3} \tag{3.11}$$

Where K_{P_u} is the ultimate net pressure coefficient, equal to P_u/σ_v' and e is the distance from the sea floor to the application point of the lateral load. For the purpose of this chapter this loading eccentricity e is 10 m. The effects of varying e and other pile properties is shown in Fig. 3.5 [41, 81]. Using H_{ult} and M_{ult} provides an upper bound to the rotational stiffness K_θ of the proposed spring in Fig. 3.4, formulated by Shadlou & Bhattacharya [67]:

$$K_{\theta\text{-initial}} = C_k D L_{pen}^2 G_{0.75L} \tag{3.12}$$

Where $G_{0.75L}$ is the soil shear modulus at the point of rotation and C_k is a term which describes the relation between the L/D ratio and the profile of the shear modulus over the depth, given as [24]:

$$G_{0.75L} = \frac{500\sqrt{p' p_a}}{v_{sand} 1.3} \approx 75 \text{ MPa} \tag{3.13}$$

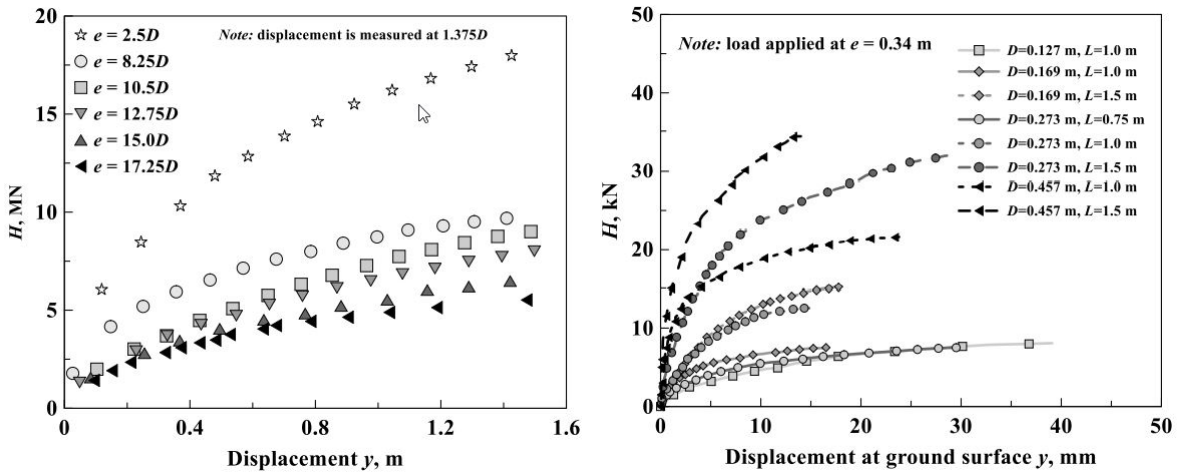

Figure 3.5: Ultimate lateral load H_{ult} with varying loading eccentricities and pile geometries [41, 81]

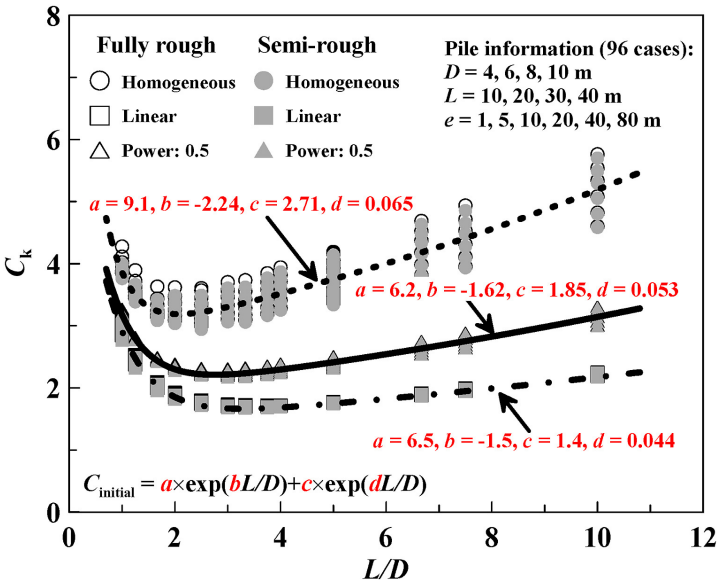

Figure 3.6: C_k values calculated from FE analysis [82].

$$C_k = a \cdot exp\left(b \times \frac{L}{D}\right) + c \cdot exp\left(d \times \frac{L}{D}\right) \text{ for } 10 \geq \frac{L}{D} \geq 1 \tag{3.14}$$

For $L/D < 6$, which is verified by Amar Bouzid [2]. For the purposes of CSD operation G_0 can easily be obtained through cone penetration tests at the work site. For a constant G_0 over the penetration depth as is used in this project the spud roughness coefficients become; a = 9.1, b = -2.24, c = 2.71 and d = 0.065 [82]. These expressions result from the curve fitted to empirically determined C_k values found in FEM analysis as shown in Fig. 3.6 [82]. Eqs 3.13 and 3.14 can be substituted back into Eq. 3.12 to find the initial stiffness for the case as presented in Table 3.1. For unknown C_k values, the following approximation is proposed by Amar Bouzid [2]:

$$K_{\theta-initial} = 4G_{0.75L}DL^2 \tag{3.15}$$

Shear modulus degradation for fairly large rotation in sand has a major impact on the actual

rotation stiffness during operation. The actual value of K_θ as a function of the rotation angle θ can be obtained from the degradation of the shear modulus (for medium-dense sand) found from [60]:

$$\frac{G}{G_0} = \frac{1}{1+\gamma/0.00025} \tag{3.16}$$

The resulting rotational stiffness is then provided as:

$$\frac{K_\theta}{K_{initial}} = \frac{1}{1+\theta/0.00025} \tag{3.17}$$

The shear modulus degradation and the total stiffness are presented in Fig. 3.7 and 3.8 [81]. It shows that the stiffness is relatively high for small rotation angles and can be approximated as equal to the initial stiffness. Soil degradation starts to take effect when the strain on the sand increases. This explains the non-linear nature of the curve. Together with the reaction forces from the hydrodynamic behaviour of the CSD pontoon and the cutter ladder on the spud, the mass-spring system can then be solved for the rotation of the spud at the mudline. A discrepancy of about 20% can be seen between the rotational stiffness methods of Shadlou and Bhattacharya, and Amar Bouzid. FEM data suggests good agreement between the model results and the C_k formulation given in Eq. 3.14 [67], so this K_θ distribution will be used going forward.

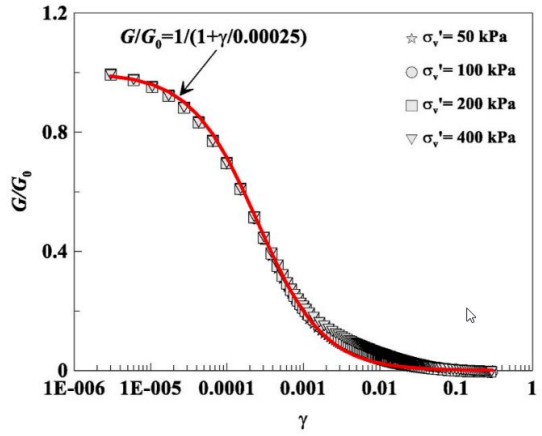

Figure 3.7: Shear modulus G_0 degradation in medium-dense sand [81].

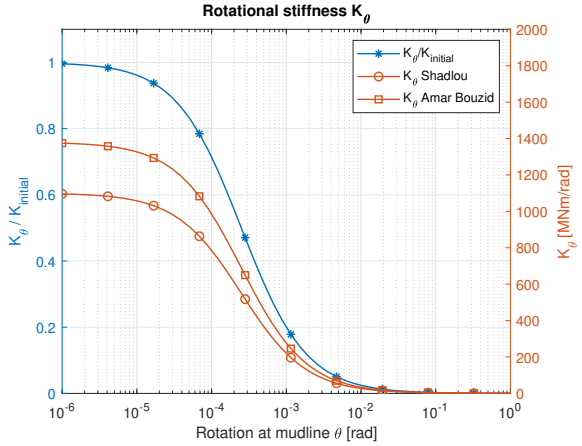

Figure 3.8: Rotational stiffness K_θ as a function of rotation angle θ.

The three assumptions made at the beginning of this section can now be verified. Firstly, the assumption that the spud can be regarded as a rigid pile in rotation, where the bending stiffness is very high compared to the soil stiffness for the pile section below the mudline, and therefore the pile deflection can be neglected compared to the rotation. Meyerhof et al. [48] proposes the following relation between the pile and soil stiffness where this assumption is valid, based on experimental data:

$$\frac{K_{rs}}{K_{soil}} > 1 \qquad \rightarrow \qquad \frac{E_p I_p}{E_{sand} D^4} = 3.84 \tag{3.18}$$

Where K_{rs} is the relative bending stiffness of the spud. From Eq. 3.18 it can be seen that it is safe to assume rigid rotation at a penetration depth of 2.13 m. Secondly, it is assumed that the method presented by Wang for shallow depth, wide piles can be used for the purpose of a CSD spud. For this use-case, the ultimate soil pressure that is allowed before soil failure is

achieved is the crucial parameter, which is used to determine operability in the eventual model simulation. Therefore the ultimate soil pressure is checked with [47]:

$$Q_{ur} = 0.12\gamma^{'} \cdot D \cdot L_{pen}^{2} \cdot K_p \tag{3.19}$$

Where Q_{ur} is the load on the tip of the spud. Comparing this to the stiffness given in Eq. 3.12, the resulting load for soil failure can be seen in Fig. 3.9. It shows how the load asymptotically approaches the limit found in Eq. 3.19. Therefore it is verified that this limit is accurate as an operational limit for soil failure.

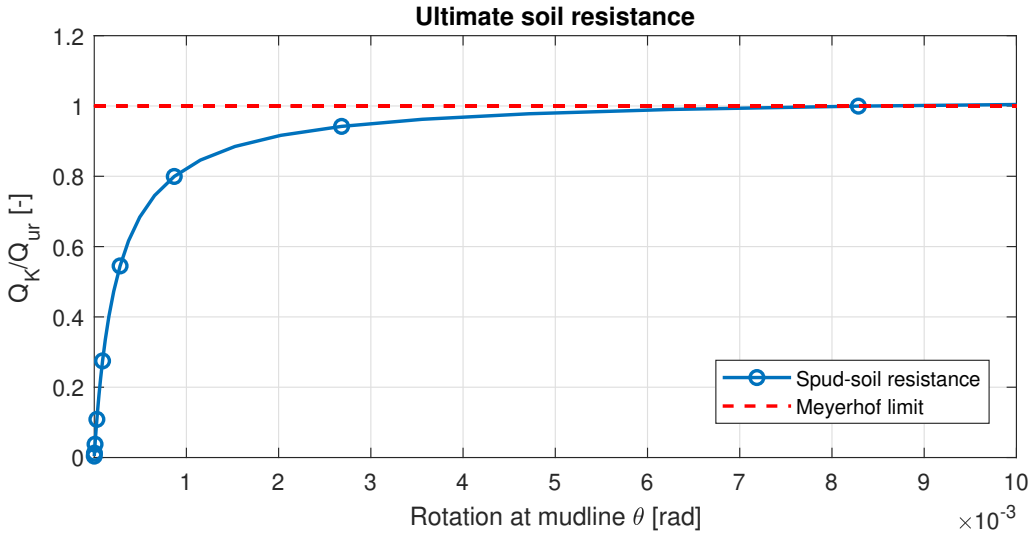

Figure 3.9: Verification of the ultimate soil load.

Lastly, the effect of cyclic loading on the ability of the soil to counteract the spud forces has to be checked. Up until this point, it was assumed that the rotation of the spud was situated in the elastic deformation region of the soil. However, it can be expected that in reality the movement of the soil after multiple loading cycles can cause the soil to shift away plastically from the spud and thereby reduce the overall soil stiffness. Experiments on this plastic deformation of sand under cyclic loading has been done by Okur et al. [58]. This study included cyclic triaxial tests to establish the boundaries between elastic and plastic behaviour of fine-grained soils. It was found that this threshold lies around 90% of the maximum small strain shear modulus G_{max}. To exclude any plastic behaviour from the model, the limit for soil failure will be reduced by 10% as argued by Okur.

3.4. Spud stiffness matrix

Due to the added complexity in modelling the spud interactions with the soil, the spud cannot be modelled in AQWA as it lacks the sub-soil resources to add complex boundary conditions. Therefore the model is decoupled into a pontoon-ladder system and a spud-soil system, modelled in AQWA and MATLAB respectively. To ensure an accurate approximation of the entire CSD system in AQWA, the spud needs to be represented in terms of its bending stiffness components. Here the expression by Wichers [84] will be used. It is assumed that the spud is free-sliding in vertical direction, and the CSD is free to move around the spud in yaw rotation:

$$c_{xx_s} = c_{yy_s} = \frac{3 \cdot EI}{L_i^3} \tag{3.20}$$

$$c_{x\theta_s} = c_{y\phi_s} = -\frac{3 \cdot EI}{L_i^3} \cdot (L_i + \overline{KG}) \tag{3.21}$$

$$c_{\theta x_s} = c_{\phi y_s} = -\frac{3 \cdot EI}{L_i^3} \cdot (L_i + \overline{KG}) \tag{3.22}$$

$$c_{\theta\theta_s} = c_{\phi\phi_s} = \frac{3 \cdot EI}{L_i^3} \cdot (L_i + \overline{KG})^2 \tag{3.23}$$

Due to the symmetry of the spud in x and y direction these components are equal. L_i refers to the height of the force application points from the bottom of the spud. The spud keeper system has two application points to be able to resist rotational movements of the CSD in its clamped configuration, 3 meters apart in vertical z-direction. These points are assumed to provide forces on the spud based on the direction the motion of the pontoon. Therefore L_i becomes:

$$L_1 = L_{pen} + h + 1.790 \tag{3.24}$$

$$L_2 = L_{pen} + h - 1.218 \tag{3.25}$$

Where L_{pen} is the penetration depth and h is the water depth. For this calculation the added effective spud length in bending due to the heave motion of the pontoon is neglected. As

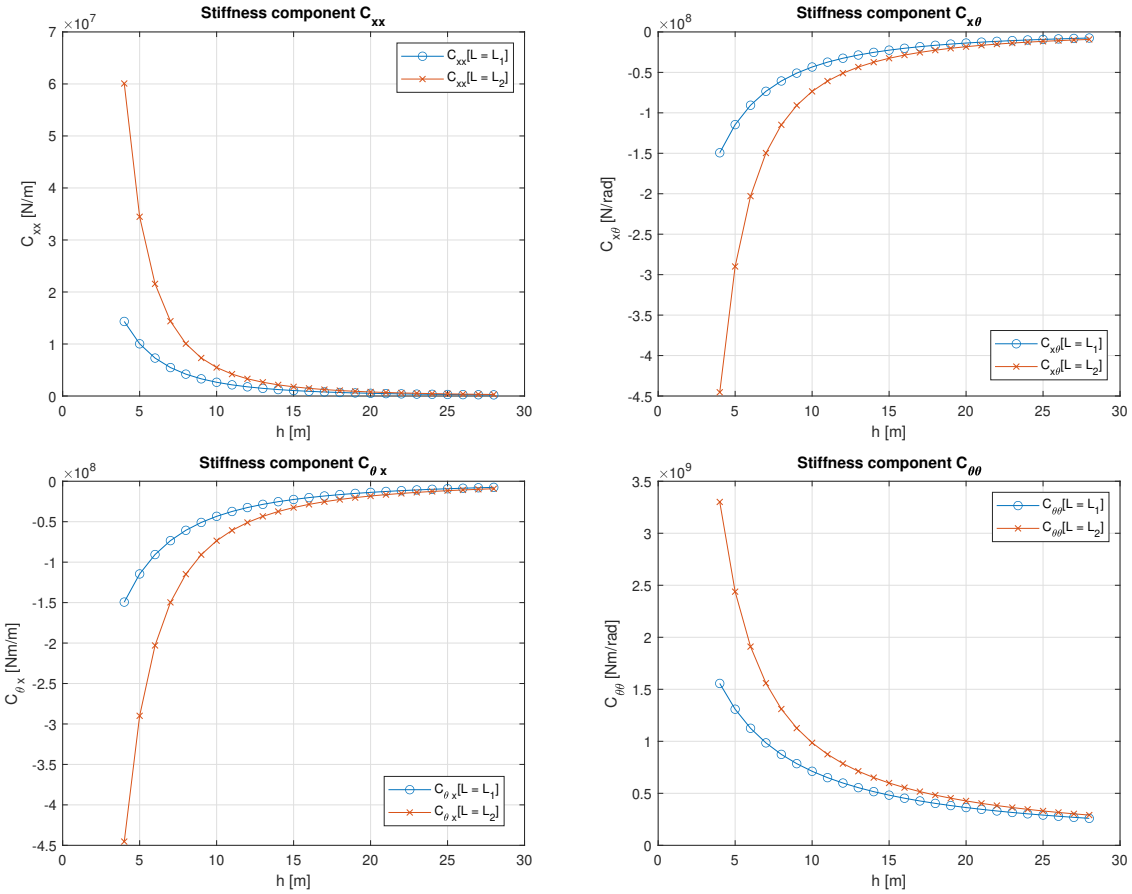

Figure 3.10: Distribution of spud bending stiffness for different water depths.

mentioned previously the matrix is symmetrical in x and y direction, as well as in rotation around the x and y-axis. The total distribution of the relevant matrix elements over the water depth for both application points are shown in Fig. 3.10. It can be seen that the stiffness decreases with an increase in the effective spud length, which is most noticeable at shallow depths. The stiffness for both application point converges for large water depths, when the water depth relative to the distance between the application points becomes very large.
With the bending stiffness E_pI_p of the spud, the resonant frequencies of the spud can be determined. At these frequencies the bending stresses are higher due to the cyclic loading caused by the wave forces. Fig. 3.11 shows the natural frequencies as a function of the water depth, with the most common wave periods highlighted in green. It shows that, for this spud configuration, resonance occurs mostly at water depths between 12 m and 20 m.

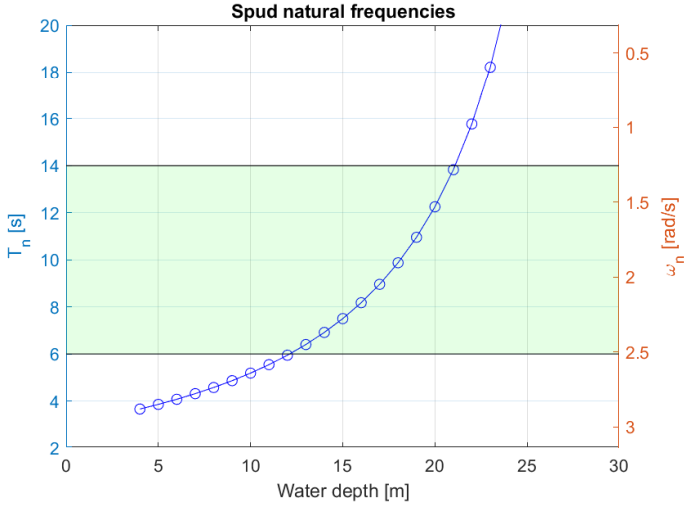

Figure 3.11: Spud natural bending frequencies.

3.5. Spud as Euler Beam

As one of the main failure mechanisms, correctly determining the shear and bending moments in the spud is paramount. Therefore the spud is uncoupled from the rest of the system so the bending moment induced by the pontoon can be integrated over the spud length to find the resulting deflection, irregardless of water depth. To do this, the spud will be modeled as a Euler beam in bending. To be able to apply this theory, it is assumed that any deflection angle is small compared to the spud geometry and that only lateral loads are applied. The only axial load in the system is the own weight of the spud, so these assumptions are valid. Secondly, it is assumed that the plane cross-sections of the spud remain plane in bending. The Euler-Bernoulli equation which relates deflection to applied load reads:

$$\frac{\mathrm{d}^2}{\mathrm{d}x^2}\left(EI\frac{\mathrm{d}^2w}{\mathrm{d}x^2}\right) = q \tag{3.26}$$

Wherein EI is the flexural stiffness of the spud, $w(z)$ is the deflection at height z and q is the applied load. Translating this over the spud length, the shear and moment distributions can be calculated, as shown in Fig. 3.12 [40], resulting in a deflection as shown in Fig. 3.13. A spud is comprised of multiple wall thicknesses along its length, based on where the maximum bending moment will occur. The bending stiffness of the spud is therefore the sum of the bending stiffness of the 'active' sections. The area moment of inertia of one of these sections

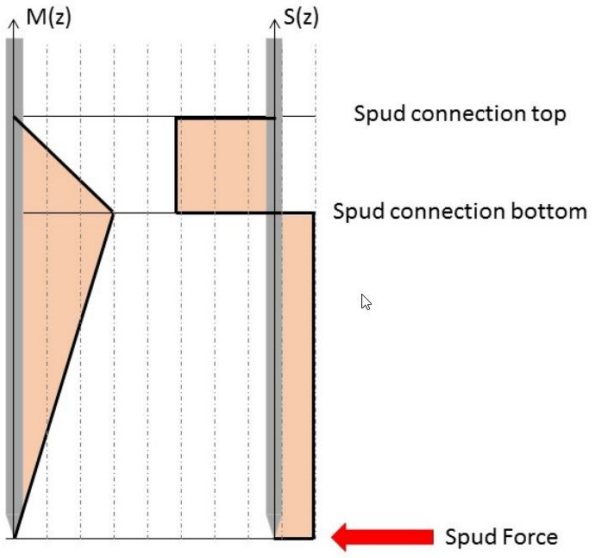

Figure 3.12: Shear and moment distribution over the length of the spud [40].

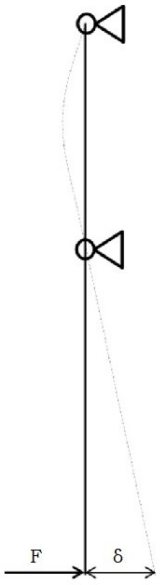

Figure 3.13: Spud deflection in clamped configuration.

is described as:

$$I_x = I_y = \frac{\pi}{4} \cdot \left(R_2^4 - R_1^4\right) \tag{3.27}$$

$$I_z = \frac{\pi}{2} \cdot \left(R_2^2 - R_1^2\right) \tag{3.28}$$

Table 3.2 shows a possible wall thickness distribution for a spud pole of 27 m, and its weighted wall thickness to find the average. It can be seen that the wall thicknesses roughly follow the distributions of Fig. 3.12. The total displacement of the spud is the sum of the rotation due to the spring connection with the soil, and the deflection due to bending.

Section	Length [mm]	Wall thickness [mm]	Weighted thickness
1	3000	35	3.89
2	3000	40	4.44
3	5400	35	7.00
4	4600	32	5.47
5	11000	19	7.74
Sum	27000	-	28.53

Table 3.2: Spud wall thickness distribution.

Fig. 3.14 shows the numerical process needed to find the eventual rotation and displacement of the spud. A lateral load H and moment M will be applied which causes the rotational stiffness of the soil to change due to the new displacement w_1. A new displacement will then be calculated using the new rotational stiffness found at that spud angle. This continues until the solution converges to the final displacement w_N.

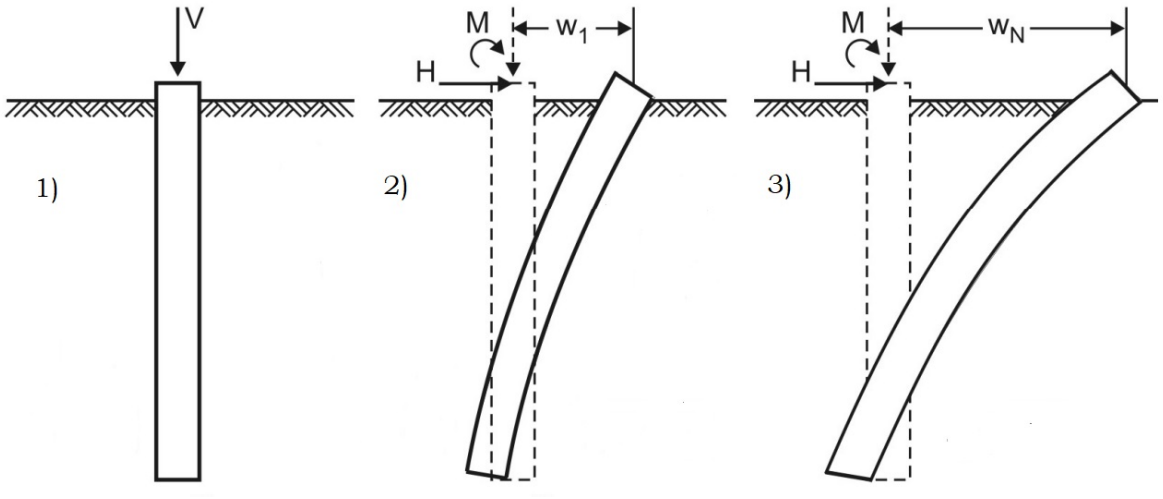

Figure 3.14: Sketch of the spud motion determination process.

3.6. Cutter forces

Cutter forces from the cutter head can be divided into two parts: operational loads and reaction forces from the ladder due to pontoon motions. The cutting process will produce both shear and moment loads which can influence the motion of the CSD, but mostly induce large loads on the ladder hinge. This section will establish these loads and the resulting stresses in critical components. The movement of the cutter head is a function of the pontoon motion and the Morison forces on the ladder itself. The submerged weight of the cutter head is so large that there is no real lift of the ladder from the soil surface, but there is a large component of soil reaction forces preventing the head to bury itself into the soil. This reaction force can be characterised as a spring reaction, where the stiffness is determined by the type of soil. This section will outline these forces and establish the relevant soil stiffness.

3.6.1. Operational forces

The operational forces are very much dependent on the soil that is being cut, in both force amplitude and the force profile over the width of the cut [78]. The reaction forces are transferred from the ladder through either the spud or the side wires to keep the CSD in place. These forces can be divided into three components: a horizontal and vertical force, as well as an axial force through the ladder. A simple linear relation exists that relates the cutter power to the reaction forces that are encountered for specific soils [78]. These relations are as follows:

$$\frac{F_{hor}R_{cutter}}{M_{cutter}} = c_h \quad \frac{F_{ver}R_{cutter}}{M_{cutter}} = c_v \quad \frac{F_{ax}R_{cutter}}{M_{cutter}} = c_a x \tag{3.29}$$

Where M_cutter is related to the specific energy, the thickness of the slice being cut and the characteristics of the swing motion. Further elaboration upon the magnitude of these forces is given in Appendix B. In general the design values for these constants are: c_v = 0.9, c_a = 0.4 and c_h = 1 or 0.6 for under-cutting and over-cutting respectively. These three forces are implemented as fixed forces on the tip of the ladder in the AQWA model that do not change with CSD motion. Characteristic values pertaining to the torque and dimensions of the cutter specific for the CSD700 are presented in Appendix A.

Lastly, it should be mentioned that there are significant differences in the operational forces of the cutter depending on the direction of rotation of the cutter head. This under- or overcutting not only alters the direction of the operational forces, mainly horizontally, but become large enough that they govern the swing motion of the CSD in the overcutting case. In this situation, the swing winches have to pull opposite of the swing motion to counteract the self-propelling nature of the cutter head's movement. In practice, CSD operators can choose to solely use undercutting to eliminate these overcutting forces, which is done frequently for harder soil materials. For this model, only undercutting is considered, meaning all horizontal operation forces are opposite to the swing direction. A more in-depth breakdown of the difference between the cutting directions is given in Appendix B.

3.6.2. Cutter-soil interaction

As discussed in Section 3.3, the soil pressure and the lateral movement of the soil are linked through their unique p-y relation. Therefore, when the force on the cutter head due to the pontoon motion is known, the resulting soil movement can be calculated. In sand, this relation is described as:

$$p = Ap_u \tanh\left(\frac{kD}{Ap_u}y\right) \tag{3.30}$$

With A being a factor to account for loading conditions (0.9 for shallow depth cyclic loading), P_u the ultimate soil resistance (as given in Eq. 3.7) and k the initial modulus of the subgrade reaction of sand, as provided by API [35]. The specific p-y relation for medium-dense sand with the properties given in Table 3.1 is shown in Fig. 3.15. The spring stiffness of the sand can be found by differentiating Eq. 3.30:

$$K_{sand} = \frac{\mathrm{d}}{\mathrm{d}y}\left[Ap_\mathrm{u}\tanh\left(\frac{kx}{Ap_\mathrm{u}}\right)\right] = Ap_\mathrm{u}\frac{kx/Ap_\mathrm{u}}{\cosh^2\left(\frac{kxy}{Ap_\mathrm{u}}\right)} \tag{3.31}$$

Fig. 3.15 shows the result of the p-y curve analysis for cuts up to 1 m depth in sand. The straight lines in the right image indicate the spring stiffness of the sand at that depth when considering the linear-elastic behaviour only. The behaviour can be approximated as a straight line up to the ultimate soil reaction force, which therefore is a linear spring system.

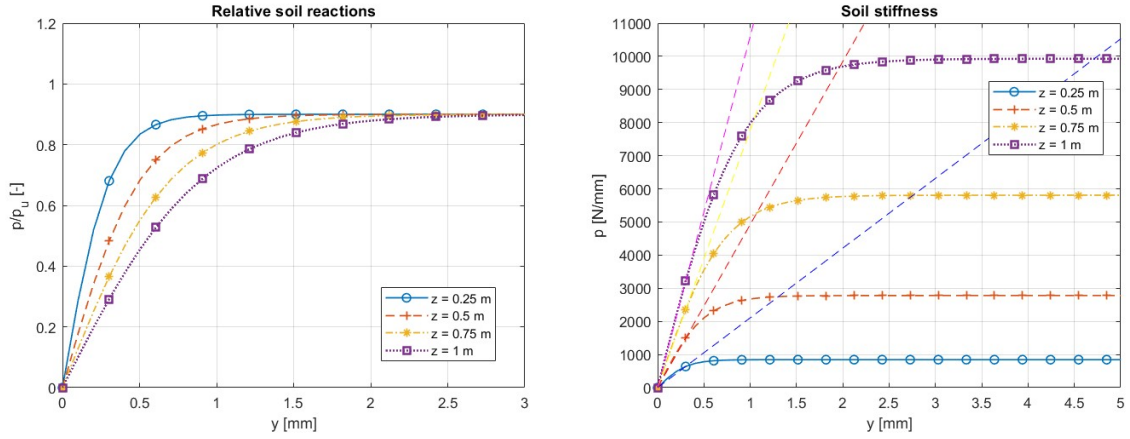

Figure 3.15: *Left:* Relative p-y relation of sand up to 1 m depth. *Right:* Complete p-y curve of sand at multiple depths and the resulting elastic soil stiffness.

3.7. Swing wires

The swing wires control the swing motion of the CSD, but also provide a noticeable stability component due to their pretension. Therefore they become the main component in preventing unwanted yaw motion of the CSD around the spud, together with the cutter head. The operational limits of the swing wires can be divided into two parts: the ultimate stress capacity of the wires and the power needed to operate the winches. The main failure modes for these aspects are breakage of the wire itself due to increased tension from wave and current forces, or exceedance of the power the winch can generate to both restrict unwanted yaw motion while employing the swing motion needed for operation. Failure of the anchor or anchor connection will not be considered as this is too conditional on incorrect placement or local differences in soil properties.

To determine the wire tension at any given moment, first the configuration of the wires has to be established. When performing the swing motion, the wires change orientation and with that, change their relative angle with the incoming wave angle. This is illustrated in Fig. 3.16 and 3.17 [50].

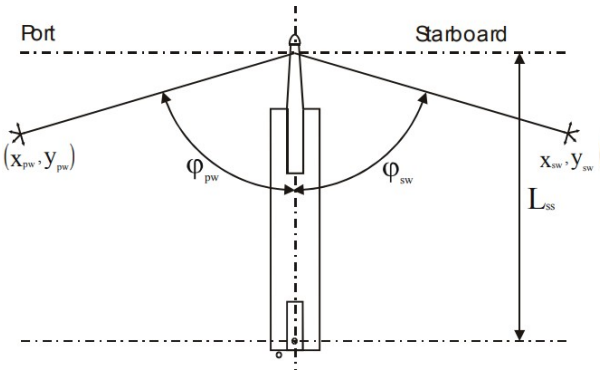

Figure 3.16: Configuration in swing angle $\phi_s = 0°$.

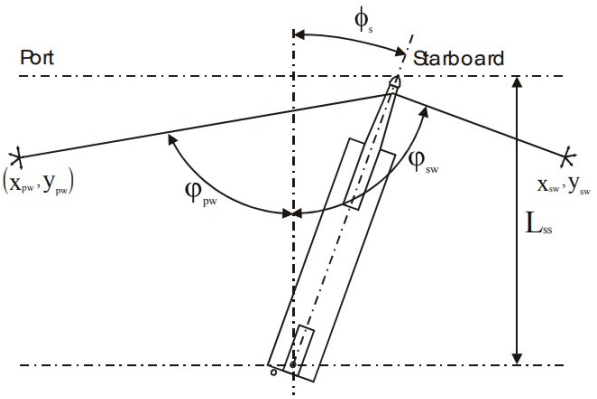

Figure 3.17: Configuration in swing angle $\phi_s = 30°$.

It can be seen that the wire angle has changed significantly when the CSD is at the end of its swing motion. This effect is exaggerated if the anchors are placed further away from the connection to the ladder in x-direction. The total tension found in the x-y plane can be found using the sum of all moments around the spud [50]:

$$\begin{aligned} \Sigma M_{spud} &= (T_0 + \Delta T)L_p - (T_0 - \Delta T)L_s + F_{wave}L_G - F_{cutter}L_{cutter} = 0 \\ \rightarrow \quad & I_\psi \cdot \ddot{\psi}_s = M_{wave} + M_{cutter} + M_{wires} \end{aligned} \tag{3.32}$$

Where T_0 is the wire pretension, ΔT is the tension due to the wave and operational forces, L_G is the distance from the spud to the CoG of the vessel, and $\ddot{\psi}_s$ is the yaw acceleration around the spud. Some assumptions are made when this is implemented into the model: the wires are approached as perfect linear springs with a constant stiffness. Secondly, the wires are assumed to be always taut, regardless of tension. In reality however, some catenary effects can be observed when the tension gets very low, where the wire drags along the floor and locally alter its behaviour. This is beyond the scope of this model and will not be considered. Practically all swing wires and their accompanying winches are designed in a way such that both fail at a similar tension. Winches use the same type wire regardless of what soil is cut or where is being operated, so economically it would not be logical to install winches with a much higher capacity. Assuming that the relation between the horizontal and the tangential force remains constant, the side winch power can be found [78]:

$$\frac{P_c}{P_s} = \frac{F_c}{F_h} \frac{\frac{2\pi n R_c}{60}}{v_w} = \frac{F_c}{F_h} \cdot \frac{\pi n R_c}{30 v_w} \tag{3.33}$$

Where F_c is the tangential force, F_h is the horizontal swing force, P_c/P_s is the ratio between the cutter power and the swing power, n is the cutter head speed, R_c is the cutter radius, and v_w is the swing speed. Vlasblom [79] showed that there exists a relation between the ratio of the normal force and the cutting force, and that this relation directly influences the relation between the cutter power and the side winch power. Using Eq. 3.32, the swing power in the horizontal plane becomes:

$$P_s = M_h \frac{v_h}{R_{sp}} = (F_h R_{sp} - M_c \sin\beta + W \cdot R_w) \frac{v_h}{R_{sp}} \tag{3.34}$$

This assumes the vertical tensions are negligible and friction in the winch is negligible. For the model the wires are modelled as springs in 3D, so the overall elongation will include tension in all three directions.

4

Multibody Dynamics

This chapter will expand on the CSD geometry and the operating conditions into specific hydrodynamic coefficients which are used to find the forces resulting from the wave loading. These forces can then be used to find the hydrodynamic response to waves in the model. First, the concept of the equation of motion for the CSD will be introduced and it will be elaborated how each component is calculated for both frequency and time domain simulations. An approach is proposed to find viscous damping which is neglected in potential theory and needs to be added into the model manually. Afterwards, these coefficients are used to find the external wave forces due to the fluid motion to complete the equation of motion.

4.1. Geometry and conventions

A full overview of the characteristics of the CSD700 are given in Appendix A, including dimensions and operational parameters. The CSD geometry will be modelled consisting of three main parts:

- **Main barge and pontoons.** This includes the vessel containing all mechanical drive systems on board, as well as the spud carriage connecting all floating components to the spud. Due to its large surface area intersecting with the waterline, this section absorbs most of the hydrodynamic forces on the system. As the stresses and deformations found in this part are not as critical as the spud, the pontoon is modelled as a rigid body.
- **Cutter ladder and cutter head.** The cutter ladder is subject to large buoyancy and current forces, as well as the cutter head being the main application point for the operational cutter forces. It is separated from the barge to give insight into the hinging movement between the two bodies and the associated forces on the hinge. There can be significant stresses in the ladder, however these are beyond the scope of this project, therefore the ladder is modelled as a rigid body.
- **Spud.** The spud is the main failure component in the CSD-spud system in waves, therefore extra attention will be provided to stresses and possible deformations in this part. The spud will be modelled as an Euler beam, as discussed in Ch. 3.

Features on the CSD that do not have any significant wave interaction due to their own body shape are modelled as boundary conditions using spring and damping elements. Most notably the swing and hoisting wires have a negligible surface area, but are integral in the motion response and operability analysis of the CSD. Relevant mass and geometry parameters for the remaining components are given in Section 4.2 to establish the equilibrium position without

external forces. Furthermore all hydrodynamic coefficients will be stated for the two main separate components in the model: the pontoon, and the cutter ladder.

To fully describe the motion of the CSD, standard notations of motion for a body in space will be used. The naming conventions used for ships specifically are shown in Fig. 4.1 and Table 4.1. The model will include all 6 DOFs of the pontoon, as well as the pitch of the cutter ladder as it is an important aspect in describing the workability limits of the entire system. Two coordinate systems need to be defined before being able to describe the ship motions accurately. Firstly, the body-bound coordinate system $G(x_b, y_b, z_b)$ has an origin coinciding with the center of gravity (COG) of whichever body it applies to. Secondly, the earth-bound frame $O(x_0, y_0, z_0)$ is locked in place, irregardless of ship motion, with the x-y plane on the still water plane. This allows for the description of relative motion between the CoGs of the pontoon and the ladder, but also actual distance responses relevant for time domain analysis. Three important terms will be used interchangeably with their respective wave headings: beam seas for waves that hit the side of the CSD at 90° or 270°, head seas for waves that hit the front of the CSD at 180° and quartering waves that approach diagonally from 45° or 135°.

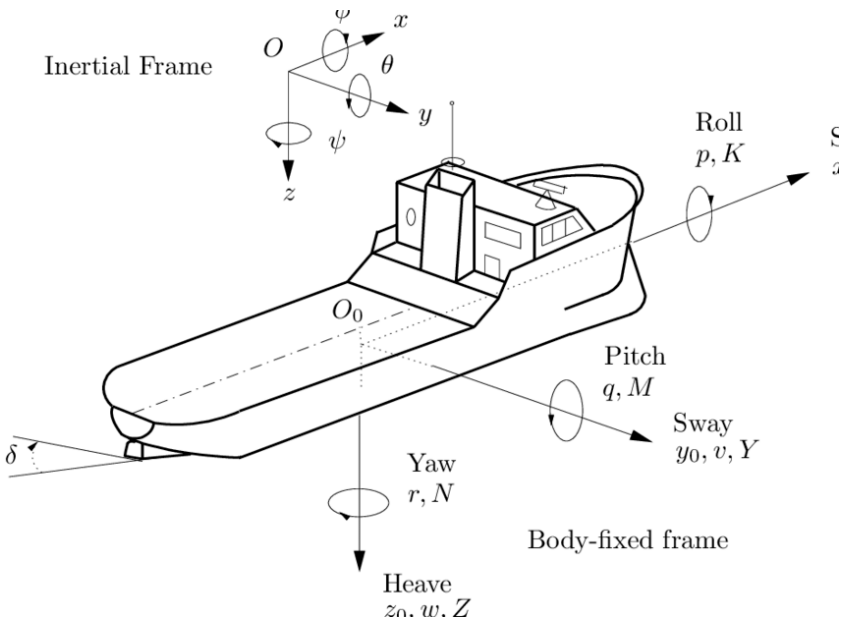

Figure 4.1: Conventions of standard notation in ship motions [69].

DOF	Name	Symbol	Unit	Description
1	Surge	x	[m]	Translation along x
2	Sway	y	[m]	Translation along y
3	Heave	z	[m]	Translation along z
4	Roll	ϕ	[rad]	Rotation about x
5	Pitch	θ	[rad]	Rotation about y
6	Yaw	ψ	[rad]	Rotation about z
7	Ladder pitch	θ_L	[rad]	Ladder rotation about y

Table 4.1: Conventions of CSD motions.

Finally, three boundary conditions have to be added to describe the interaction of the waves and the pressure fields found in Ch. 2 with the surface of the CSD. First, the kinematic boundary condition on the body of the CSD ensures no water particles pass through the hull. At the instantaneous position of the hull the fluid motion in the direction of the normal to the body (perpendicular to the surface) have to be equal to the body motion in this normal direction [37]:

$$\vec{\nabla}\Phi \cdot \vec{N} = \vec{V} \cdot \vec{N} \tag{4.1}$$

Where $\vec{\nabla}\Phi \cdot \vec{N}$ represents the motion of the fluid and $\vec{V} \cdot \vec{N}$ represents the motion of the body. Next, because potential theory does not take into account fluid viscosity, any waves that reflect of the CSD would travel forever. To counter this the radiation condition is used within AQWA, where at large distances away from the CSD, after the wave has interacted with the CSD, any remaining body and diffraction potentials have to fully dissipate [32, 74]. Lastly, the symmetric and anti-symmetric boundary condition for potential theory is used:

$$\begin{aligned} \Phi^{(2)}(-x,y) &= -\Phi^{(2)}(+x,y) \\ \Phi^{(3)}(-x,y) &= +\Phi^{(3)}(+x,y) \\ \Phi^{(4)}(-x,y) &= -\Phi^{(4)}(+x,y) \end{aligned} \tag{4.2}$$

This condition describes that, due to the symmetry of the CSD in the xz-plane, the resulting motions from any wave loading have to be equal or equal and opposite for sway, heave and roll. This condition does not count for the remaining DOF, as there are obvious asymmetries in the yz-plane. It can however be used to half the necessary wave directions that are to be modelled; a beam sea will have the exact same motion response regardless of if its wave angle is 90° or 270°. This majorly reduces computing time.

4.2. Equation of motion

As with most dynamics analyses, the equation of motion is based on Newton's law of dynamics to describe the accelerations of the system:

$$M \cdot \ddot{\vec{x}} = \vec{F} \tag{4.3}$$

Wherein F is a sum of all external forces, and M and x are a mass-geometry matrix and a motion matrix respectively:

$$M = \begin{bmatrix} \rho\nabla & 0 & 0 & 0 & 0 & 0 \\ 0 & \rho\nabla & 0 & 0 & 0 & 0 \\ 0 & 0 & \rho\nabla & 0 & 0 & 0 \\ 0 & 0 & 0 & I_{xx} & 0 & 0 \\ 0 & 0 & 0 & 0 & I_{yy} & 0 \\ 0 & 0 & 0 & 0 & 0 & I_{zz} \end{bmatrix} \tag{4.4}$$

$$\vec{x} = \begin{bmatrix} x \\ y \\ z \\ \phi \\ \theta \\ \psi \end{bmatrix} \tag{4.5}$$

In Eq. 4.4, the masses are derived from Archimedes' Law (as the topsides masses and distributions are not exactly known yet) to preserve a draught of 1.5 m, and I_{ij} are the respective second area moments of the water plane in i,j direction for the radius of gyration k_{ij}:

$$\begin{aligned} I_{xx} &= k_{xx}^2 \cdot \rho\nabla = \int \rho\left(y^2 + z^2\right)\, dA \\ I_{yy} &= k_{yy}^2 \cdot \rho\nabla = \int \rho\left(x^2 + z^2\right)\, dA \\ I_{zz} &= k_{zz}^2 \cdot \rho\nabla = \int \rho\left(x^2 + y^2\right)\, dA \end{aligned} \tag{4.6}$$

In hydrodynamic analysis, the external force vector F includes three parts: the hydrodynamic reaction forces, the hydrodynamic restoring forces and the wave excitation forces. For all six degrees of freedom this provides the general solution of the equation of motion in the frequency domain:

$$M \cdot \ddot{\vec{x}} = -A_{ij}(\omega)\ddot{\vec{x}} - B_{ij}(\omega)\dot{\vec{x}} - C_{ij}\vec{x} + \vec{F}(\omega)sin(\omega t + \epsilon) \tag{4.7}$$

In Eq. 4.7 $A_{ij}(\omega)$ is the added mass matrix, $B_{ij}(\omega)$ is the damping matrix and C_{ij} is the restoring force matrix resulting from the hydrostatic stiffness of the water. Further derivations of the hydrodynamic coefficients $A_{ij}(\omega)$, $B_{ij}(\omega)$ and C_{ij} will be given in Section 4.3. The external force vector includes all accelerations and forces of the pontoon and the ladder as a result of wave excitation and Morison forces, as well as mooring forces from the spud, the cutter and the swing wires as presented in Section 3.7. To describe a time simulation a convolution integral is added, made up of retardation functions as first presented by Cummins [15] to include the 'memory effects' of water. Therefore this formula is often referred to as the Cummins' equation of motion for all six degrees of freedom i:

$$\sum_{i=1}^{6}\sum_{j=1}^{6}\left\{\left(M_{ij} + A_{ij}\right)\ddot{x}_j + \int_{-\infty}^{t} R_{ij}(t-\tau)\dot{x}_j(\tau)\mathrm{d}\tau + C_{ij}x_j\right\} = F_{ext}(t) \tag{4.8}$$

With the retardation function $R_{ij}(t)$:

$$R_{ij}(t) = \frac{2}{\pi}\int_0^{\infty} B_{ij}(\omega)\cos(\omega t)d\omega \tag{4.9}$$

An example of the pitch-pitch retardation function is given in Fig. 4.2. It can be seen that the initial impulse response is very large, but trails off quickly to a fraction of the initial value. Eventually this will approach zero. This effect will become apparent in the TD results where the model will display a start-up period with large fluctuations in displacements and forces, which quickly dampen out towards the steady-state solution.

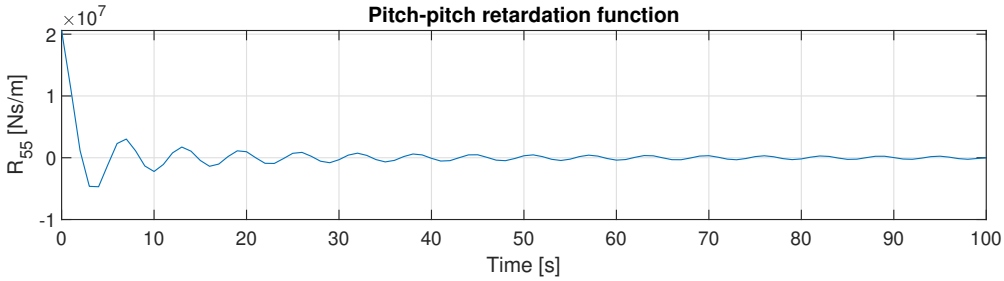

Figure 4.2: Retardation function R_{55}.

4.3. Hydrodynamic coefficients

As presented in the previous section, the equation of motion requires mass and inertia inputs based on the mass and geometry of the system, however there are also components that are not covered by these matrices. In particular these are the added mass and damping components that have to be added to provide the full picture of reaction forces from the water on the CSD. This section will provide the background on the method of acquiring these components for the two main floating structures.

4.3.1. Added mass

Added mass is an extra component of inertia that floating structures have to move when they start accelerating. A portion of the surrounding fluid has to be moved with the structure to satisfy the conservation of mass in the fluid. In reality, every fluid particle near the moving structure has to move at least slightly to accommodate the movement, however it can be approximated by adding the mass of some volume of fluid to the mass of the structure. The added mass coefficient is found by taking the mass of this volume of fluid and dividing it by the displaced fluid mass [30]. This coefficient is dependent on multiple factors, including the structure geometry, the wave frequency and the water depth. Fig. 4.3 and 4.4 show the added masses as a function of the incoming wave frequency for all 6 DOF. It can be seen that for motions where more water has to be displaced and where these displacements are relatively large, the added mass is the largest, in this case mainly in heave and pitch motions.

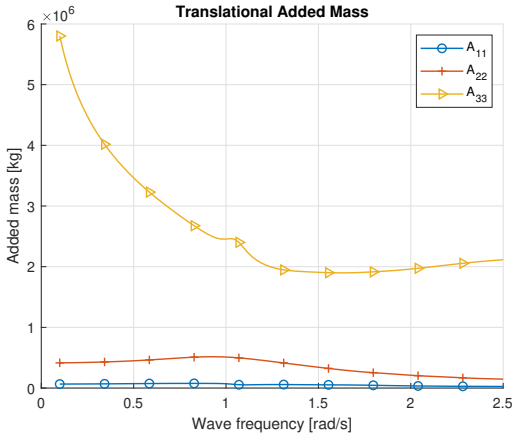

Figure 4.3: Added mass for translational motions.

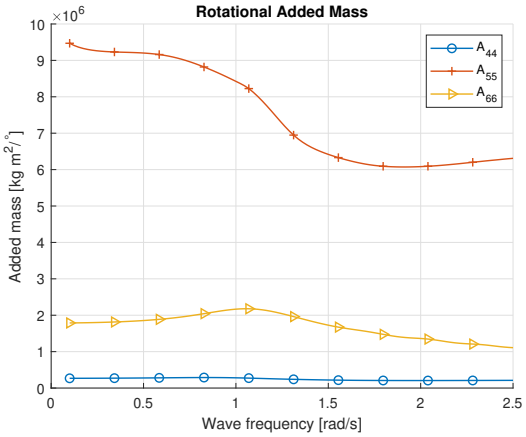

Figure 4.4: Added mass for rotational motions.

In the time domain the added mass can no longer be defined using wave frequency. The most common method to remove the frequency dependency is the use of retardation functions like Eq. 4.9. The added mass can then be replaced for the added mass at an infinitely high frequency [26]:

$$A(t) = a(\omega = \infty) + \frac{1}{\omega} \cdot \int_0^\infty R(\tau) \cdot \sin(\omega\tau) \cdot d\tau \tag{4.10}$$

Where $R(\tau)$ is the previously mentioned retardation function. As $R(\tau)$ is a function of the frequency-dependent total hydrodynamic damping coefficient $B(\omega)$, this will be discussed in Section 4.3.2. As the wave frequency increases to the added mass will converge to a certain value where the added mass is independent of the wave frequency. This is validated in the results in Fig. 4.3 and 4.4, where it can be seen that the added mass converges to a single value for high frequencies.

Finally, the effects of shallow water on the added mass should be checked. Model experiments done on moored barges show that even small decreases of water depth can lead to a large increase in added mass [87], especially when the water depth decreases to below 1.5T. This effect is largest in heave, roll and pitch, as these motions actively decrease the distance to the sea floor and thus increase added mass. Fig. 4.5 shows this effect for the pitch motion of the CSD. It can be seen that the increase is largest for very shallow water, with the most exaggerated effect for low frequency waves. However, also the higher frequencies are affected and should therefore not be neglected.

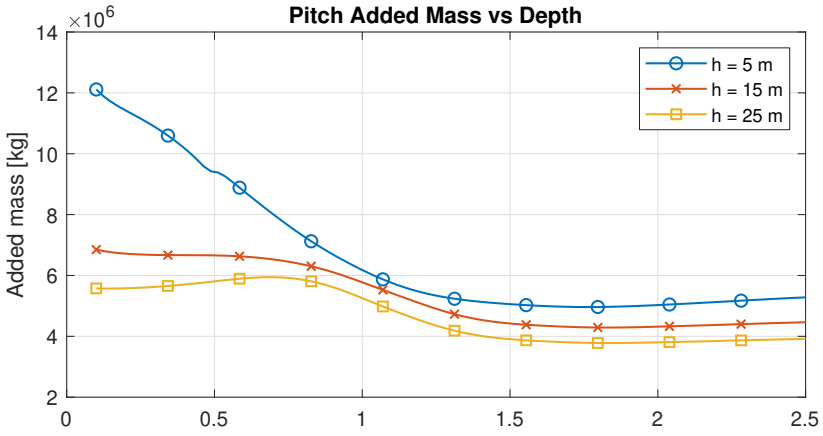

Figure 4.5: Added mass as a function of depth.

4.3.2. Viscous damping

In Section 2.1 it was stated that the viscosity of water had to be ignored in order to use potential theory, which is most obvious in rotational motions of a ship. When the CSD rolls, it creates large waves radiating away from the hull which dissipate a lot of the energy which otherwise would have caused a very large roll motion. Due to the width and the rectangular shape of a barge-like vessel like a CSD, this is a lot more prominent than in vessels with rounded hulls. Research shows that especially the increased velocity of flow when in situations with shallow water depth can cause an overestimation of the motion response in both analytic formulations as well as common diffraction software [12]. A full analysis of the frequency domain response of a rectangular barge for the AQWA software is given in Appendix C.
To accommodate the real damping into the equation of motion a linearised viscous damping term is added as a fraction of the critical damping:

$$B_{visc} = \xi \cdot B_{crit} = \xi \cdot 2 \cdot \sqrt{(A(\omega) + M(\omega) \cdot C} \tag{4.11}$$

The fraction ξ has to be determined separately for each degree of freedom through experimental data, however research suggests some common values for rectangular barges, which can be seen as a good approximation for a CSD [31]. Clauss et al. [12] found negligible values for the damping coefficient for surge, sway, heave and yaw, which is verified in the experiments by Brown presented in Appendix C. A pitch correction was done with 2% of critical damping and a roll correction with 5% of the critical damping respectively. This roll motion response is therefore the most important degree of freedom to consider in the viscosity damping. To better approximate ξ in roll an expression is proposed based on the geometry of the pontoon [9]:

$$B_{44} = B_f + B_e + B_w + B_L + B_{BK} \tag{4.12}$$

For:

$$\begin{aligned} B_f &= \text{Hull skin friction damping,} \\ B_e &= \text{Hull eddy shedding damping,} \\ B_w &= \text{Free surface wave damping,} \\ B_L &= \text{Lift force damping,} \\ B_{BK} &= \text{Bilge keel damping.} \end{aligned}$$

Due to the different use of a CSD compared to a regular ship, some of these components can be neglected: B_{BK} is zero due to the absence of a bilge keel and B_L is zero as there is no forward speed of the CSD during operation. The free surface wave damping is the only damping component that is not neglected in potential theory and will result from the radiation damping analysis in the AQWA software. The relative magnitude of the different components can be seen in Fig. 4.6, with respect to the Froude number $Fn = v/\sqrt{gL}$.

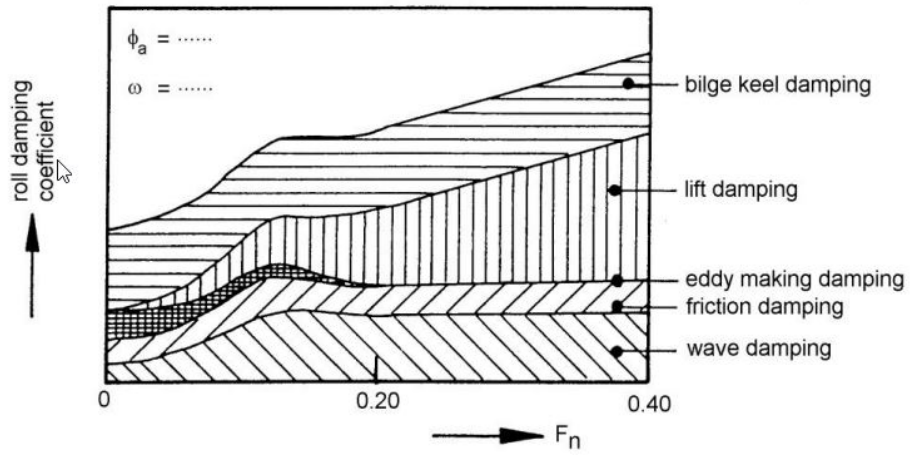

Figure 4.6: Components of viscous roll damping [37].

From this Fig. 4.6 it can be seen that the addition of a bilge keel could severely increase the resistance to roll the CSD has, but this is outside the scope of this project. The relevant damping components are defined as [38]:

$$B_f = \frac{4}{3 \cdot \pi} \rho S r_e^3 \phi C_f \omega \tag{4.13}$$

Wherein S is the wetted surface of the pontoon, C_B is the block coefficient and C_f is the friction coefficient, which is based on the effective bilge keel radius r_e resulting from the sharp edge of the pontoon:

$$S = L\left(1.7T + C_B B\right) \tag{4.14}$$

$$C_B = \frac{\nabla}{LBT} \tag{4.15}$$

$$C_f = 1.328 \left(\frac{2\pi v}{3.22 r_e^2 \phi^2 \omega} \right)^{\frac{1}{2}} \tag{4.16}$$

$$r_e = \frac{1}{\pi} \left(\left(0.887 + 0.145 C_B\right) \frac{S}{L} - 2 \cdot OG \right) \tag{4.17}$$

The flow separation at the edges of the pontoon account for another large part of the damping at low Froude numbers due to the shedding of eddies. Many expressions were discovered for different ship shapes and different operating conditions, but the one used for this purpose was found by Ikeda [31] for sharp-edged barge-like structures:

$$B_e = \frac{2}{\pi} \rho L T^4 \left(H_0^2 + 1 - OG/T\right) \left(H_0^2 + (1 - OG/T)^2\right) \phi \omega \tag{4.18}$$

The free surface wave damping (or radiation damping) is not a viscosity-based function of damping, but depends on the wave parameters themselves. Therefore, it can easily be added to the damping matrix found in potential theory as long as the wave shape is known. This damping force is created from the creation of waves that radiate away from the CSD when it oscillates, which dissipates energy. The AQWA software already implements this as follows [32]:

$$B_w = 12B_{w0} \cdot [((A_2+1)+(A_2-1)\cdot \tanh(20(\tau-0.3))) \\ +(2A_1-A_2-1)\cdot \exp(-150(\tau-0.25)^2)] \tag{4.19}$$

Where:

$$\begin{aligned} A_1 &= 1+\zeta_d^{-1.2}\cdot \exp(-2\zeta_d) \\ A_2 &= 0.5+\zeta_d^{-1.0}\cdot \exp(-2\zeta_d) \\ \zeta_d &= \omega^2 d/g \\ \tau &= U\cdot\omega/g \end{aligned} \tag{4.20}$$

The eddy-shedding damping in Eq. 4.12 is non-linear and consequently the total viscous damping is reliant on the current roll amplitude ϕ_a of the pontoon. This general non-linear component of viscous damping can also be implemented into Eq. 4.11 as suggested by Journée [36]:

$$\xi = \xi_1 + \xi_2 \cdot \phi_a \tag{4.21}$$

$$\xi_1 = 0.0013 \cdot \left(\frac{B}{T}\right)^2 \quad \text{and} \quad \xi_2 = 0.50 \tag{4.22}$$

This method is verified with the experimental data for a sharp-keeled barge in roll from the study by Brown [7]. Using a simple rectangular barge, the critical damping factor was determined. A barge-like structure like a CSD should have viscous damping in the range of 3 - 7% [9]. Fig. C.8 shows different percentages of critical damping and how they agree with the experimental data. It can be seen that the best fit for the experimental data is a damping factor of 5%, which is within the right range. This verifies the approach presented above to find the viscous damping for a CSD. The total resulting damping for the CSD including the (linear) radiation damping and non-linear viscous damping are given in Fig. 4.7 for a water depth of 5 m.

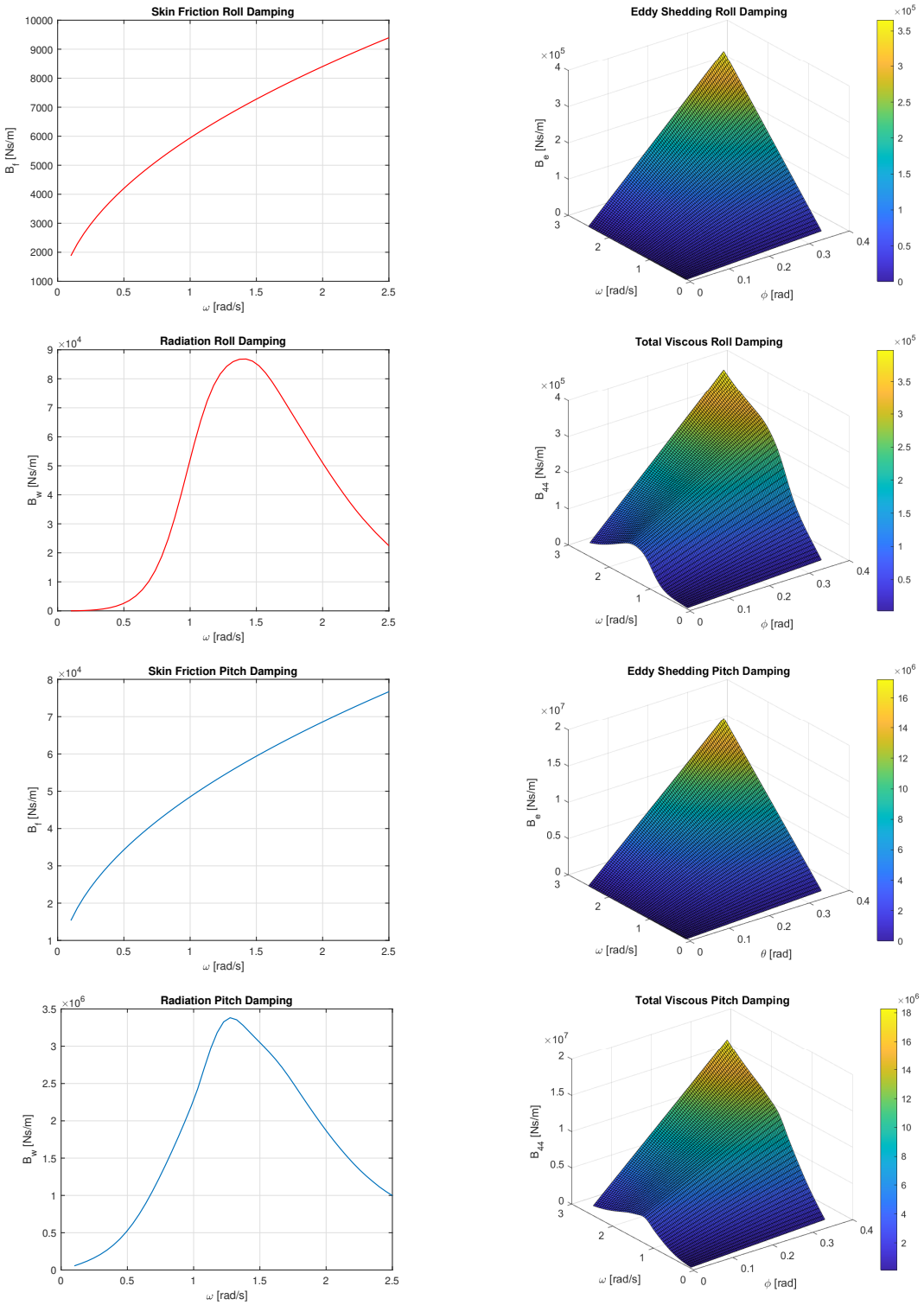

Figure 4.7: Total viscous roll and pitch damping of the CSD for h = 5 m.

4.3.3. Hydrostatic stiffness

The hydrostatic stiffness of a vessel describes predominantly the way force due to gravity is counteracted by the buoyancy. In the case of any vertical motion, be it in heave, pitch or roll, a spring stiffness component has to be added to the C_{ij} matrix (which is independent of wave frequency) that relates this new equilibrium. This matrix is shown in Eq. 4.23 for water plane area A and second moment of the water plane area I_{ij}. The total stiffness of the CSD is found by adding the stiffness of the boundary conditions onto this matrix. Due to its independence of wave frequency, the hydrostatic is easily calculated using Archimedes:

$$\boldsymbol{C_{ij}} = \begin{bmatrix} 0 & 0 & 0 & 0 & 0 & 0 \\ 0 & 0 & 0 & 0 & 0 & 0 \\ 0 & 0 & K_A^{33} & K_A^{33}y & -K_A^{33}x & 0 \\ 0 & 0 & K_A^{33}y & K^{44} & -K_A^{33}xy & (F_{eq})\,x \\ 0 & 0 & -K_A^{h}x & -K_A^{h}xy & K^{55} & (F_{eq})\,y \\ 0 & 0 & 0 & 0 & 0 & 0 \end{bmatrix} \tag{4.23}$$

Where:

$$\begin{aligned} K_A^h = \rho g A_c, \qquad K_A^r = \rho g I_{xx}, \qquad K_A^p = \rho g I_{yy} \\ F_{eq} &= mg - \rho g \nabla \\ K_h^{44} &= -mgz_g + F_B z_B + K_A^r + K_A^h y^2 \\ K_h^{55} &= -mgz_g + F_B z_B + K_A^p + K_A^h x^2 \end{aligned} \tag{4.24}$$

4.4. External forces

This section will cover any external forces needed to complete the equation of motion given in Eq. 4.7, which are forces that are not defined by movement of the CSD. For floating bodies, the first-order wave forces can be divided into drag components (form drag and friction drag) and inertial components (diffraction forces, Froude-Krylov forces and radiation forces). These inertial forces are an expression of the forces that are generated by the hydrodynamic coefficients. Depending on the size of the structure and the wave height and length, it can be calculated if and which one of these two forces dominates over the other. This is done using the Keulegan-Carpenter number KC [39]:

$$KC = \frac{U_{max} \cdot T}{l} = 2\pi \cdot \frac{\zeta_a}{l} \tag{4.25}$$

Where U_{max} is the maximum fluid velocity, ζ_a is the wave amplitude and l is the characteristic length of the structure in the direction the wave is travelling. The assumption can be made that the motions and forces of a structure are inertia-dominant if $KC \leq 1$ [80]. Taking a worst-case scenario for a large wave of H_s = 2 m, ζ_a = 1 m:

$$KC_{beam} = 0.524 \qquad KC_{head} = 0.140 \tag{4.26}$$

Both KC numbers are less than 1, therefore drag forces can be neglected. This means the fluid undergoes minimal flow separation and therefore has no considerable vortex shedding or other drag-related forces are present.

4.4.1. Inertial forces

The inertial forces are made up of forces arising from potential flow theory and can thus be expressed in terms of wave potentials. The total wave potential in this case:

$$\Phi = \Phi_I + \Phi_D + \Phi_R \tag{4.27}$$

Where Φ is the total wave potential, Φ_I is the undisturbed wave potential, Φ_D is the diffraction potential and Φ_R is the radiation potential. Φ_I describes the flow of the undisturbed wave, which creates Froude-Krylov forces (FK) due to the pressure difference. Φ_D describes the way in which the flow is altered due to the presence of a structure. These potentials are expressed as [83]:

$$\Phi_I = \mathsf{Re}\left\{\phi_W \cdot i\omega\zeta_a e^{i\omega t}\right\} \tag{4.28}$$

$$\Phi_D = \mathsf{Re}\left\{\phi_D \cdot i\omega\zeta_a e^{i\omega t}\right\} \tag{4.29}$$

Where ϕ_W is the space-dependent part of Φ_I:

$$\phi_W = \frac{\zeta_a g}{\omega^2} e^{kz} e^{i(kx\cos\mu + ky\sin\mu)} \tag{4.30}$$

$$\frac{\partial \phi_D}{\partial n} = \frac{\partial \phi_W}{\partial n} \tag{4.31}$$

Eq. 4.28 and 4.29 evaluate from the kinematic boundary condition: fluid cannot travel through the wetted surface of the CSD, so the flow has to alter to comply with the conservation of mass. AQWA is used to find these potentials, which makes use of Green's Theorem to integrate the pressure over the wetted surface S. As both FK and diffraction forces are due to non-viscous components, they can be combined with:

$$\vec{F_D} + \vec{F_W} = -\iint_S (p \cdot \vec{n_k})\,\mathsf{d}S = \rho\zeta_a\omega^2 \cdot e^{i\omega t} \iint_S (\phi_W + \phi_D)\,\mathsf{d}S \tag{4.32}$$

$$\vec{M} = -\iint_{S_H} p \cdot (\vec{r} \times \vec{n})\mathsf{d}S_H \tag{4.33}$$

Where r is the position of normal vector n. When integrated over the entire surface S it describes the shape and position of the body in the fluid flow. The pressure results from the appropriate wave theory and is therefore governed by the dynamic pressure field, as that is the main component in the wave pressure field. The combination of the force due to diffraction and the FK forces are a function of the wave frequency, which means they can be described as a function of this frequency:

$$F_W = F_{A,\zeta_a} \cdot \zeta_a \cos\left(\omega t - \varepsilon_{F,\zeta}\right) \tag{4.34}$$

Where F_W is the force per meter wave amplitude of the non-viscous wave forces. This concept of expressing force per meter wave amplitude is further elaborated on in Section 5.2.

The radiation potential Φ_R is a function of the added mass and the damping terms in the equation of motion, governing the wave-making ability of a structure. A wave causes the floating structure to oscillate, which in turn creates waves at the frequency of the oscillation which radiate away from the structure [37]. These radiated waves counteract motion by dissipating energy and because it is dependent on the damping term, is different for each DOF. It is defined as [83]:

$$\frac{\partial \Phi_R}{\partial n} = \sum_{j=1}^{6} v_j \cdot f_j(x,y,z) \quad \text{with} \quad f_j = \frac{\partial \phi_j}{\partial n} \tag{4.35}$$

4.4.2. Morison's equation

An adequate way of determining the drag and inertia forces on slender structures is through the use of the Morison equation. For the CSD this affects hydrodynamic forces on the cutter ladder and the submerged part of the spud. The effect of an oscillating flow like a wave on a slender structure can be visualised as the structure having a pressure difference between the side where the wave hits (high pressure) and the wake (low pressure). This induces a force on the structure. In reality these forces are very hard to compute due to the flow around a slender structure being very complex and forming vortices and eddies around its surface. The Morison equation is empirically calculated and therefore an approximation of these effects. For a structure to be considered slender in this approach, the diameter of the structure should not exceed 0.2 times the wavelength of the incoming wave [52]. The empirical Morison equation becomes:

$$f = \rho C_M \frac{\pi D^2}{4} \dot{u} + \frac{1}{2} \rho C_D |u| u \tag{4.36}$$

Including a current velocity U:

$$f = \rho C_M \frac{\pi D^2}{4} \dot{u} + \frac{1}{2} \rho C_D |u + U| (u + U) \tag{4.37}$$

Where f is the force on the structure per meter depth, C_M is the inertia coefficient defined as the added mass coefficient C_a plus one, C_D is the drag coefficient, and u and $\dot{u}$ are the horizontal water particle velocity and acceleration respectively, which are governed by the applicable wave theory. In the case the body itself oscillates in the wave, as is the case for the cutter ladder, the inertia of the body should be added as well [10]:

$$f = m\ddot{x} + C_M \rho \frac{\pi}{4} D^2 \dot{u} + \frac{1}{2} C_D \rho D |u| u \tag{4.38}$$

Whenever Morison cannot be used, diffraction theory will be applied. The limits to the Morison relation can be seen in Fig. 4.8.

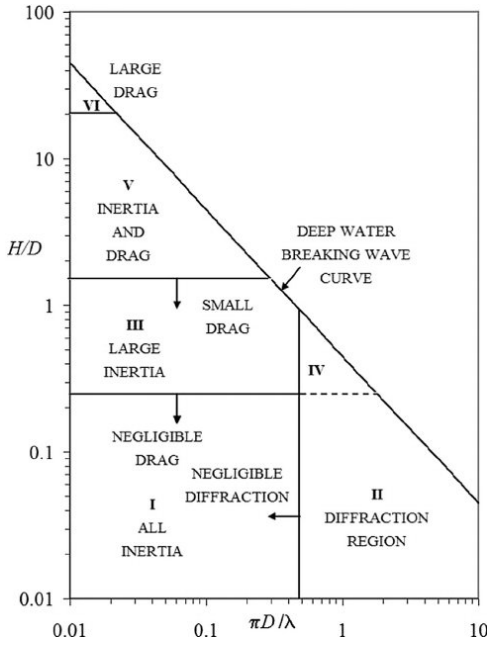

Figure 4.8: Limits of diffraction and Morison theory [10].

4.4.3. Second-order forces

Second-order wave forces are forces found from the incident wave which do not correspond to the frequency of that wave, be it either higher or lower. Together with the first-order forces they provide a full view of the wave forces. These forces and their induced second-order motions can be divided into three components. First, the mean wave drift force which describes the way a vessel tends to float in the direction of wave propagation. This force is characterised by resonance of wave groups with very low-frequency natural frequencies of the vessel, most notably for surge, sway and yaw motions. The force is proportional to the incident wave amplitude squared and constant, creating a slowly changing equilibrium position described using the horizontal motions and the yaw angle. This yaw angle is especially important as this changes the angle at which the dominant wave direction hits the vessel. As these forces are strongly correlated with the natural frequencies of the system, they will first be given in the frequency domain and then transformed into the time domain. From Eq. 2.1 the wave amplitude squared ζ^2 can be found:

$$\zeta^2(t) = \sum_{i=1}^{N} \sum_{j=1}^{N} \zeta_i \zeta_j \cos(\omega_i t + \varepsilon_i) \cos(\omega_j t + \varepsilon_j) \tag{4.39}$$

Where the subscripts i and j indicate the wave parameters for two interacting waves and ε indicates the phase difference between the waves. The mean wave drift force can be found using the pressure field across the surface, as seen in Eq. 2.49. The general mean wave drift force then follows as [37]:

$$\vec{F}^{(2)}_{MWD} = -\int_{-T}^{\zeta} p \cdot \vec{n}\, dS \tag{4.40}$$

Where T is the draught of the CSD and n is the vector normal to the wetted surface. To verify the value of the mean wave drift force, it can also be derived from the kinetic energy from the wave. This provides an upper limit to the mean wave drift force, assuming the wave is fully reflected (reflection coefficient R_{ref} = 1):

$$F^{(2)}_{MWD,upper} = \frac{1}{2}\rho g \cdot (R_{ref} \cdot \zeta_a)^2 \tag{4.41}$$

The second and third components needed to find the second-order forces are oscillating components for frequencies lower or higher than the wave frequency. These forces are determined by using Quadratic Transfer Functions (QTFs). The first of these oscillating components has a linear character as it is caused by first-order wave loads. As the CSD oscillates vertically it oscillates using the natural period of the restoring stiffness found in 4.23. This effect is larger if the wave period approaches this natural period. The second oscillating component occurs in the low-frequency region, mostly for horizontal motions. It is a result of non-linear elements of irregular wave groups, for example due to a very low-frequency oscillation from wave groups instead of singular waves. The resulting force increases when these frequencies approach the natural frequencies of the mooring system. For the CSD this effect is most defined for the natural frequencies of the swing wires and the stiffness of the spud. As most definitions of the second-order wave forces are for the total forces, it is complex to decouple the oscillating components from the mean drift force mentioned above as they are encapsulated together in the QTFs. Research done by Pinkster [63] shows that the complete second-order forces can be described by a five part equation:

$$\begin{aligned}\vec{F}^{(2)} = &-\frac{1}{2}\cdot\rho g\oint_{wl}\left(\zeta_r^{(1)}\right)^2\cdot\vec{n}\cdot\,dl\\ &+\iint_{S_0}\left\{\frac{1}{2}\rho\left(\vec{\nabla}\Phi^{(1)}\right)^2+\rho\frac{\partial\Phi^{(2)}}{\partial t}\right\}\cdot\vec{n}\cdot dS\\ &+m\cdot R^{(1)}\cdot\ddot{X}_g^{(1)}\\ &+\rho\iint_{S_0}\left(\frac{\partial\Phi^{(2)}}{\partial t}\right)\cdot\vec{n}\cdot\,dS\end{aligned} \tag{4.42}$$

The moments used in describing the rotational motions can be found by using the cross-product of $\vec{n}$ with the positional vector $\vec{r}$ instead of n. As these equations are dynamic, the wetted surface S now consists of the sum of a static surface S_0 which is the area under the water line and a dynamic surface area s, which is the added area due to the motion of the CSD causing parts to become submerged. The five components in Eq. 4.42 consist of the following [37]:

- The force found from the relative wave height ζ_r; the difference between the wave height of the incident wave and the vertical motion of the CSD:

$$\vec{F}_A^{(2)} = -\frac{1}{2}\cdot\rho g\oint_{wl}\left(\zeta_r^{(1)}\right)^2\cdot\vec{n}\cdot\,dl \tag{4.43}$$

- The second part is a function of the dynamic second-order pressures $p^{(2)}$, caused by the pressure drop due to the first-order wave potentials.

$$\vec{F}_B^{(2)} = \iint_{S_0}\left\{\frac{1}{2}\rho\left(\vec{\nabla}\Phi^{(1)}\right)^2+\rho\frac{\partial\Phi^{(2)}}{\partial t}\right\}\cdot\vec{n}\cdot dS \tag{4.44}$$

- The third is the dynamic contribution term of the hydrostatic pressure. Because the hydrostatic pressure is defined for zero heave motion, this term has to be zero and can therefore be ignored.

$$\vec{F}_C^{(2)} = -R^{(1)}\cdot\iint_s\left(p^{(0)}\cdot\vec{n}\right)\cdot dS = 0 \tag{4.45}$$

- The fourth part is the inertia term linking the first-order rotations to the translational motions.

$$\vec{F}_D^{(2)} = \rho\iint_{S_0}\left(\frac{\partial\Phi^{(2)}}{\partial t}\right)\cdot\vec{n}\cdot\,dS \tag{4.46}$$

Where dl is a differential length along the waterline around the CSD. The matrix $R^{(1)}$ is as follows:

$$R^{(1)} = \begin{bmatrix} 0 & -x_6^{(1)} & +x_5^{(1)}\\ +x_6^{(1)} & 0 & -x_4^{(1)}\\ -x_5^{(1)} & +x_4^{(1)} & 0\end{bmatrix} \tag{4.47}$$

Where x_i are components of the motion matrix in Eq. 4.5.

- The final part is contribution of the second-order potential, providing the force exerted by the difference in frequency of waves within a wave group and the period of the wave group as a whole. This potential can be very complex due to the non-linearity of the boundary conditions for potential theory, so it is approximated with the assumption that this effect is dominated by the contribution of the undisturbed wave potential $\Phi_W W^{(2)}$. Using the expression for the first-order wave potential found in Eq. 2.45, we find the second-order potential $\phi^{(2)}$ as:

$$\Phi_{WW}^{(2)} = -\sum_{i=1}^{N}\sum_{j=1}^{N} \zeta_i^{(1)}\zeta_j^{(1)} \cdot A_{ij} \cdot \frac{\cosh\left\{\left(k_i - k_j\right)\left(X_3 - h\right)\right\}}{\cosh\left(k_i - k_j\right)h} \cdot \sin\left\{\left(k_i - k_j\right)X_1 - \left(\omega_i - \omega_j\right)t + \left(\widetilde{\varepsilon}_i - \widetilde{\varepsilon}_j\right)\right\} \tag{4.48}$$

Where A_{ij} is a coefficient based on the wave frequencies of the interacting waves and the water depth. This results in the following approximation for the second-order potential wave force:

$$F_{ij}^{(2)} = \frac{\zeta_i^{(1)}\zeta_j^{(1)} \cdot A_{ij}\left(\omega_i - \omega_j\right)}{g} \cdot F^{(1)} \tag{4.49}$$

4.4.4. Quadratic Transfer Functions

The QTFs can now be filled in using two parts as a sum or difference of the quadratic parts of the second-order forces mentioned above and the forces from the second-order potential. An example will be given for this process for the forces from the relative wave height $\vec{F}_A^{(2)}$, but these operations can be performed for every second-order force which is based on first-order motions. Performing double Fourier transforms allows the expression from Eq. 4.42 to be translated into the time domain:

$$\begin{aligned} F_A^{(2)}(t) = &\sum_{i=1}^{N}\sum_{j=1}^{N} \zeta_i^{(1)}\zeta_j^{(1)} P_{ij} \cdot \cos\left\{\left(\omega_i - \omega_j\right)t + \left(\widetilde{\varepsilon}_i - \widetilde{\varepsilon}_j\right)\right\} \\ &+ \sum_{i=1}^{N}\sum_{j=1}^{N} \zeta_i^{(1)}\zeta_j^{(1)} Q_{ij} \cdot \sin\left\{\left(\omega_i - \omega_j\right)t + \left(\widetilde{\varepsilon}_i - \widetilde{\varepsilon}_j\right)\right\} \end{aligned} \tag{4.50}$$

Where P_{ij} and Q_{ij} are transfer functions of the interaction between two waves of different wave frequencies. Herein P_{ij} denotes the in-phase forces and Q_{ij} the out-of-phase forces such that:

$$P_{ij} = \oint_{wl} \frac{1}{4}\rho g \cdot \zeta_{r_i}^{(1)'}(l) \cdot \zeta_{r_j}^{(1)'} \cdot \cos\left\{\widetilde{\varepsilon}_{r_i}(l) - \widetilde{\varepsilon}_{r_j}(l)\right\} \cdot n_1 \cdot dl \tag{4.51}$$

$$Q_{ij} = \oint_{wl} \frac{1}{4}\rho g \cdot \zeta_{r_i}^{(1)'}(l) \cdot \zeta_{r_j}^{(1)'} \cdot \sin\left\{\widetilde{\varepsilon}_{r_i}(l) - \widetilde{\varepsilon}_{r_j}(l)\right\} \cdot n_1 \cdot dl \tag{4.52}$$

The squared low-frequency wave elevation from the interaction of two wave groups is then given by [37]:

$$\left(\zeta_{LF}^{(1)}(t)\right)^2 = \sum_{i=1}^{N}\sum_{j=1}^{N} \frac{1}{2}\zeta_i^{(1)}\zeta_j^{(1)} \cdot \cos\left\{\left(\omega_i - \omega_j\right)t + \left(\widetilde{\varepsilon}_i - \widetilde{\varepsilon}_j\right)\right\} \tag{4.53}$$

Due to the complex nature of using a large amount of wave frequencies within a given spectrum, AQWA will be used to determine the QTFs by first finding the new equilibrium position to the the mean wave drift forces and using the remaining second-order force components within the time domain simulation. AQWA makes use of the same method of finding the sum and difference QTFs as provided by Pinkster [32, 63].

5

Modelling

This chapter will go in-depth into the way the CSD is modelled in ANSYS AQWA and how the concepts presented in the previous chapters are used to ultimately find the CSD motions and the way operability changes for different spud keeper configurations. The model is divided into three parts: first, a frequency domain (FD) analysis of all 7 DOF of the CSD, verified by an analytical comparison of a free-floating CSD compared to the model data. Secondly, these results are transformed to a time domain (TD) simulation based on the non-linear wave shape presented in Chapter 2. This allows for the addition of non-linear wave interactions which cannot be modeled in FD, but are crucial in coastal waves. Finally, an operability analysis is performed which relates the results from both models to the operational limits of a CSD proposed in this thesis and in the literature. These three steps will be repeated for three different spud keeper configurations with differing levels of flexibility, using the current clamped configuration as a control to compare the proposed configurations to.
To be able to apply the theoretical background set up in the previous chapters, the model is decoupled between the spud and the pontoon-ladder system. The main model consists of the pontoon and ladder modeled in ANSYS AQWA, where all mooring systems such as spud, swing wires and the cutter-soil interaction are modeled as boundary conditions to counteract the incoming wave forces. The spud is not modeled as a separate body as the AQWA software does not allow for deflection within a multibody system. The spud force is therefore calculated from the pontoon forces on the spud joint, after which the rotation and deflection are calculated with a MATLAB script, according to the process shown in Fig. 3.14.

5.1. Flexible spud keeper configurations

Using the model presented in this thesis, three types of spud keeper configurations will be analysed in terms of their response to a coastal wave climate and operability window within these conditions. All configurations are moored to the same spud with the same interactions between the swing wires and cutter with the soil. This leaves the connection between the spud and the soil as the only parameter within the equation of motion that is varied between models. The three spud keeper configurations that will be analysed are:

- **Clamped spud (CS).** This is the current situation for most CSDs working on dredging projects inland or sheltered waters. It allows for free heave and yaw movement, but all other translations and rotations are directly translated as deflection and rotation of the spud. Therefore the operability is limited almost completely by the bending stress induced in the spud, or possibly through failure of the soil caused by the spud shifting

under the cyclic loading. As it is the current design, new configurations can be compared relative to this response to gauge the possible improvements in operability.

- **Fully flexible connection (FS).** Most easily visualised as a ball and socket connection inserted in between the current spud clamp and the pontoon, where the pontoon is still allowed to move in heave and yaw with respect to the spud. The contribution of this new connection to the stiffness matrix K_c can then be described with:

$$K_{eq} = \frac{K_{spud} \cdot K_c}{K_{spud} + K_c} \tag{5.1}$$

  Where K_{eq} will be presented as a fraction of the original spud stiffness K_{spud} found in Section 3.4. Different amounts of flexibility will be tested to find the optimal amount of stiffness.
- **Force-limited connection (FLS).** A technique which has been used as a way of damage prevention for CSDs, the force-limited spud connection is a hydraulic suspension system which behaves like the clamped spud during normal operation where the spud force does not exceed the maximum bending force of the spud. When this force is exceeded, a pressure relief valve is opened, allowing some rotation of the pontoon, effectively becoming a flexible system. This allows the inertia of the pontoon to compensate for the excessive forces instead of the spud or other mechanical components. The amount of possible movement in this system is limited however, only allowing two degrees of rotation in roll and pitch [26]. This technique has been adopted by larger, specialised dredgers, most notably by Royal IHC in their Spud Guard technology [4]. In the IHC design however, the extra rotation is treated as beyond the operability limit of the CSD.

5.2. Response Amplitude Operators

The Response Amplitude Operator (RAO) is a transfer function relating the motion response of the CSD to the amplitude and frequency of the incoming wave. It makes use of the coefficients defined in the EOM to express the motion response in proportion to a set wave amplitude of 1 m in FD. An additional benefit to the FD approach and the use of regular waves is the use of the superposition principle to easily add multiple DOF responses together into the full structure response. This RAO-based response is therefore synonymous with the first-order response to a linear wave, as it is based solely on the effects of a single wave. This method can be expanded to include an irregular wave, as long as this wave can be described as a sum of multiple regular waves with the superposition principle. The limit to FD however comes from higher-order wave responses, which are fundamental to coastal wave climates. To accurately describe these, a TD analysis is required. From the EOM, the RAO follows as:

$$RAO(\omega) = \frac{a}{\zeta_a} = \frac{F_0}{C - (M + A(\omega))\omega^2 + iB(\omega)\omega} \tag{5.2}$$

where F_0 is the amplitude of the sum of all external forces as presented in Section 4.4. When the spectral distribution of the wave is known, this can be transformed into the response spectrum with:

$$S_i(\omega) = \int_{-\pi}^{\pi} S_\zeta(\omega, \mu) \cdot RAO_i(\omega, \mu)^2 d\mu \tag{5.3}$$

One of the advantages of this approach is that all mooring systems can be expressed in terms of how they affect the hydrodynamic coefficients of the total system. Starting from a free floating CSD without any mooring, mooring features can be added in terms of their additions

to the mass, damping and stiffness matrices. The same will go for the flexible spud keeper configurations, as they can be reduced to changes in the damping and stiffness matrix of the spud-moored CSD. The approach to find the RAO for the 6 DOF of the ladder-pontoon system, as well as the determination of the hydrodynamic coefficients in Section 4.3 is verified in Fig. 5.1 with the analytical solution. It shows the response of a free-floating CSD to a wave with a wave angle of 135° and 1 m amplitude.

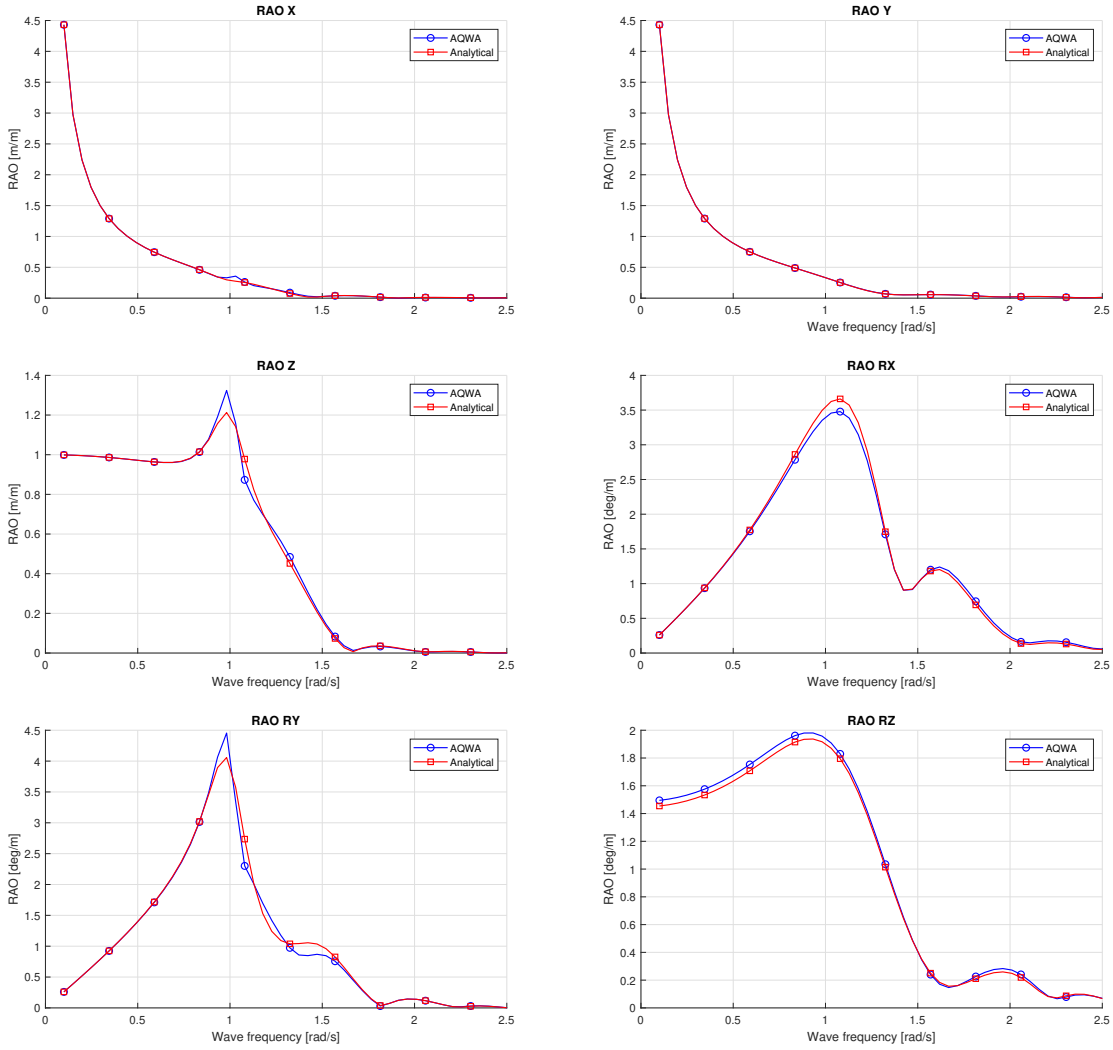

Figure 5.1: Verification of free-floating RAOs.

This comparison shows good agreement between the analytical solution and the AQWA RAOs, especially for any frequencies outside of the resonance peak. Slight discrepancies are seen, mostly in the resonance peak for heave and pitch, amounting to a difference of 4% in heave and 3% in pitch and roll. This is likely explained by imperfections in the mesh and the addition of the external lid, but is deemed sufficiently accurate. The external lid and its implementation, as well as the mesh input will be further elaborated on in Section 5.3.

5.3. ANSYS AQWA

ANSYS AQWA is a diffraction software tool used to find the hydrodynamic response of floating objects in specific sea-states. As part of the ANSYS toolkit, AQWA allows for the use of modules pertaining to other engineering disciplines such as mechanical or structural to be

implemented alongside the diffraction analysis. AQWA makes use of potential theory and panel methods to discretise a structure or vessel into source elements which interact with the velocity potentials existing within the fluid. For each panel in the mesh, a source strength is calculated to ensure the body boundary condition (Eq. 4.1 is met together with the influence of the sources of surrounding panels. For this purpose Green's theorem is used [32]. Green's theorem relates the velocity of a water particle to the source distribution over the surface:

$$G(\vec{x},\vec{\xi}) = \frac{1}{\sqrt{(x-\xi)^2+(y-\eta)^2+(z-\varsigma)^2}} + \frac{1}{\sqrt{(x-\xi)^2+(y-\eta)^2+(z+2h+\varsigma)^2}} \tag{5.4}$$

The size of the panels is controlled by the density of the mesh, but have to abide by a number of rules:

- The diffracting surface has to be split along the waterline. This allows AQWA to calculate the hydrostatic stiffness from the diffracting elements below the waterline.
- Any panel is defined by 4 nodes.
- Panel centroids cannot be close to the centroids of other panels, such that:

$$d_{min} = \sqrt{\frac{A_{panel}}{\pi}} \tag{5.5}$$

- Minimise the size difference between panels at all times, while the shape of the panel has to remain regular, be it either rectangular or triangular.
- Any panel has to be smaller that 1/7th of the shortest wavelength.

Table 5.1 shows the mesh properties of the CSD700. The panel size and defeaturing tolerance were chosen such that the shortest allowable wave frequency would be 2.5 rad/s. Any shorter waves were deemed negligible as they are not present in the wave scatter diagram of Table 2.2. The total frequency range will therefore cover 0.1 rad/s to 2.5 rad/s in 100 increments.

Mesh property	Value
Maximum element size	1 m
Defeaturing tolerance	0.5 m
No. of nodes	4478
No. of panel elements	4297
No. of diffracting elements	3559

Table 5.1: Mesh input for the CSD700 model in AQWA.

5.3.1. Project schematic

Fig. 5.2 shows the schematic sequence which is used within the AQWA software to calculate both the FD and TD results. The Geometry and Mesh modules are both ANSYS Component Systems modules, using the CAD software ANSYS Spaceclaim to translate a 3D model of the CSD into a surface element. Due to the way the hydrostatic stiffness is calculated in AQWA solid body elements are not supported. This means the mass of the CSD has to be added later, including its radii of gyration. From this, the FD analysis is done in the Hydrodynamic Diffraction module. Distinct mooring elements are only considered by AQWA in a TD analysis, so important mooring effects on the stiffness and damping matrices need to be input manually. As they cannot be modelled as distinct elements, the spud stiffness and the viscous damping

are modelled in this manner. The viscous damping is added through the sum of a linear and a non-linear value, as was elaborated on in Section 4.3. Lastly, the permanent metocean conditions are added, including water depth, the size of the water plane to be considered around the CSD and any variation in the geometry of the sea floor. For this model, the sea floor is considered flat. The HD module then calculates the motion and force RAOs for every DOF based on linear potential theory.

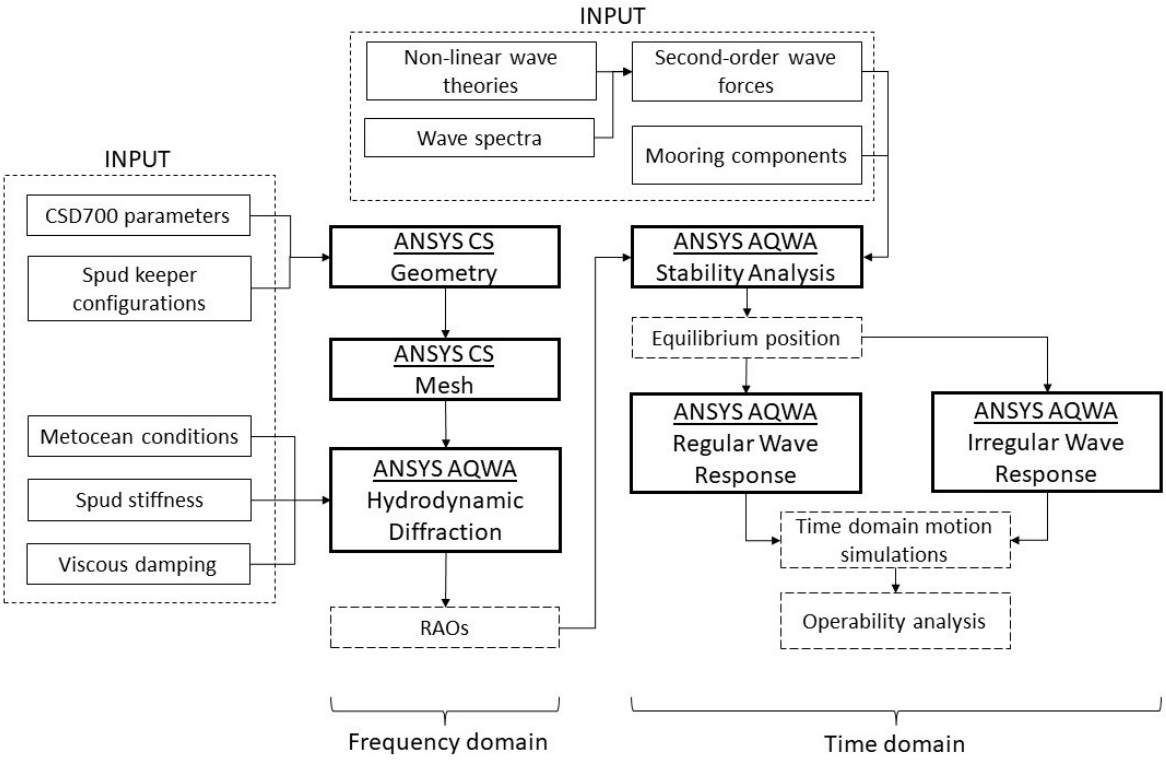

Figure 5.2: Outline of the modelling process in ANSYS AQWA.

The resulting RAOs of the motion and first-order wave forces can then be used, together with inputs for the non-linear wave forces and additional mooring components, to establish the equilibrium position of the CSD with the Stability Analysis module. In this step all mooring elements are used, including the swing wire springs and the cutter-soil spring connection. Finally, the TD simulation is performed with first the Regular Wave Response module, to find the increase in wave forces and motion response between LWT and Stokes 2nd order waves. Second, the Stokes 2nd order wave shape is used in a JONSWAP spectrum in the Irregular Wave Response module to simulate a real-world wave record.

The operability analysis is performed using the results from both the Regular and Irregular Wave Response results. A normal operability analysis makes use of a three-hour stable sea state to provide a complete image of the extremes found in a certain wave record. For the TD model used in this project, this was deemed not feasible, as the large number of time steps and panel elements would increase the computing time needed to impractical amounts. It is therefore chosen to use a reduced time domain method [46]. For all wave records that are to be analysed, a three hour wave record is generated in MATLAB. Within this record, a 300 s section is selected that contains the highest waves, as these are most likely to result in the highest operational stresses. The highest waves are defined as the largest difference in peaks

before and after a zero-crossing. This 300 s wave record is then exported as a CSV file into AQWA. Fig. 5.3 shows an example of the reduced wave train for a JONSWAP spectrum with H_s = 1 m and T_p = 8 s. It shows that even though the significant wave height is 0.5 m, the maximum wave height in a three hour wave record can be as high as 0.728 m.

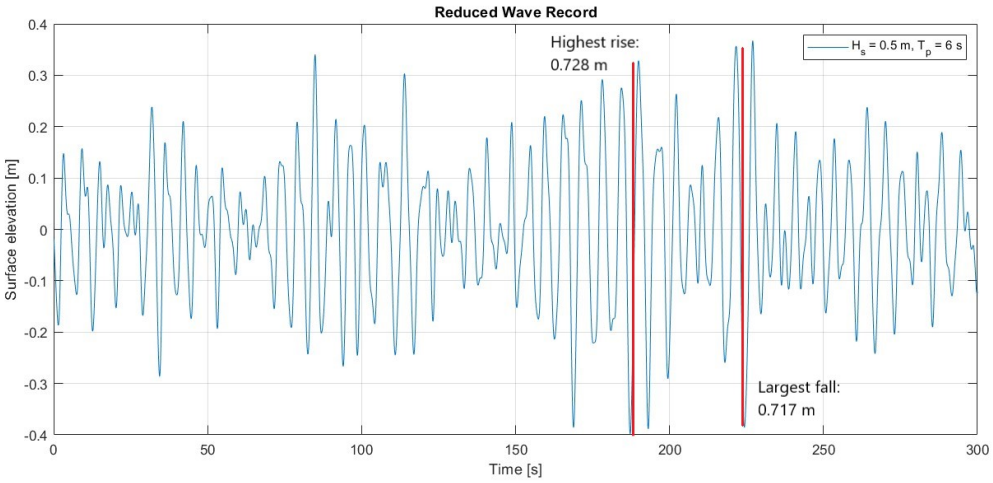

Figure 5.3: Reduced wave record of a JONSWAP spectrum.

5.3.2. Internal and external lids

Upon creating a mesh in the Mesh module, AQWA adds an internal lid into the waterplane area of the surface. Multiple bodies do not interact in FD simulation, causing them to move through other bodies which can cause irregularities in the hydrodynamic coefficients [21]. These collisions alter the RAOs of both structures which cause strange motions in the eventual TD model. The internal lid is therefore applied for the pontoon, as this surface intersects with the waterplane.

Due to the way waves diffract and radiate without any viscosity, large resonance occurs in enclosed, open-water areas within models in AQWA. To combat this, an external lid is implemented over the ladder cut-out of the pontoon, with a gap equal to the width of the cut-out and a damping factor of 75%. The effect of the external lid and the absence of a lid can be seen in Fig. 5.4 and 5.5.

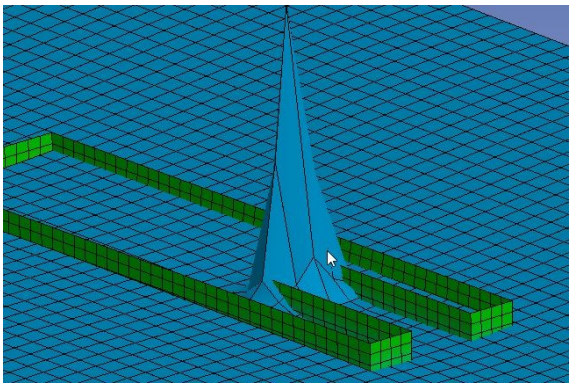

Figure 5.4: Standing wave resulting from resonance above the ladder.

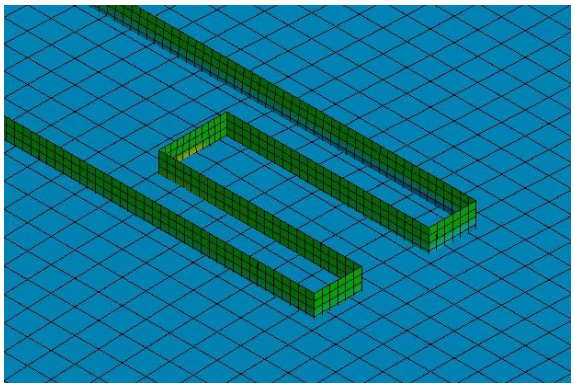

Figure 5.5: Wave interaction after implementation of the external lid.

A disadvantage of this method is that a wave frequency is damped out which is likely to correspond to a resonance frequency of the structure, as the wavelength correlates with one of the characteristic lengths of the CSD, in this case the gap in the pontoon. This is necessary however, as the model would be dominated by the standing wave if it is not damped and would become unusable.

6

Results and Discussion - FD

This chapter will present the output of the ANSYS AQWA model, using the boundary conditions and load cases presented in the previous chapters. The results will first focus on verification results of the model, including establishing the hydrodynamic coefficients of the clamped spud (CS) configuration and the resulting first-order wave forces. These values are then used to find the RAOs of the CS configuration in different water depths, which will be used as a benchmark to which different spud keeper configurations will be compared. Finally, the method is repeated for flexible spud keeper (FS) configurations to find the operability results needed to answer the main research question. As the force-limited (FL) configuration is a combination of the CS and FS designs, it cannot be expressed in FD due to its non-linear response when the transition point from clamped to flexible is reached.

Due to the way ANSYS AQWA implements connection and boundary elements, all FD models can only contain the added mass, damping and stiffness additions to its free-floating equation of motion, but no physical elements. The diffraction effects of the spud and the swing wires are therefore not included in the model. Similarly, the stiffness and operational forces of the cutter are dependent on the motion of the cutter head and therefore non-linear. This cannot be added into the FD model, which will likely cause the yaw RAO and the cutter head motion RAO to be higher than what can be expected realistically. Real-world motions can therefore not be inferred from the FD results, which further emphasises the importance of TD modelling.

To eliminate any unwanted influence on the results from external effects the model will be kept the same as much as possible. Every model will be placed in the same place in the ocean space in AQWA with a swing angle of ϕ_s = 0°. This eliminates any possible change in swing wire stiffness when the wires would otherwise be longer or shorter. Secondly, it is assumed that, because the increase in length of the swing wires for deeper water is relatively small compared to the overall swing wire length (4.8% increase between 5 m and 25 m water depth), the change in the stiffness component due to the swing wire lengthening is negligible. The variation in water depth can therefore be summarised by the following effects it has on the FD model:

- Due to the influence of the sea floor the description of the wave changes, most notably shortening the wavelength when the wave enters the shallow water region.
- The geometry of the CSD changes based on the water depth, mainly through the ladder angle with the sea floor. This provides an effective lengthening of the overall CSD in shallow water.

- As described in Section 3.4, the overall spud stiffness increases for shallow water as the length of the spud decreases.

For clarity, this chapter will mainly include the most significant results and filter out results that are less relevant, for example the roll response in head seas. These results can however be used as a base level of verification of the model. They are therefore included in Appendix D.

6.1. Hydrodynamic coefficients

As mentioned in Ch. 5, the main hydrodynamic stiffness change across different water depths is caused by the change in the spud stiffness components. The added mass and damping coefficients however do change significantly for shallow water, as was shown in Section 4.3. Fig. 6.1 and 6.2 show the added mass and linear radiation damping coefficients for the CS configuration in 5 m water depth for the pontoon, the ladder and the complete multibody model.

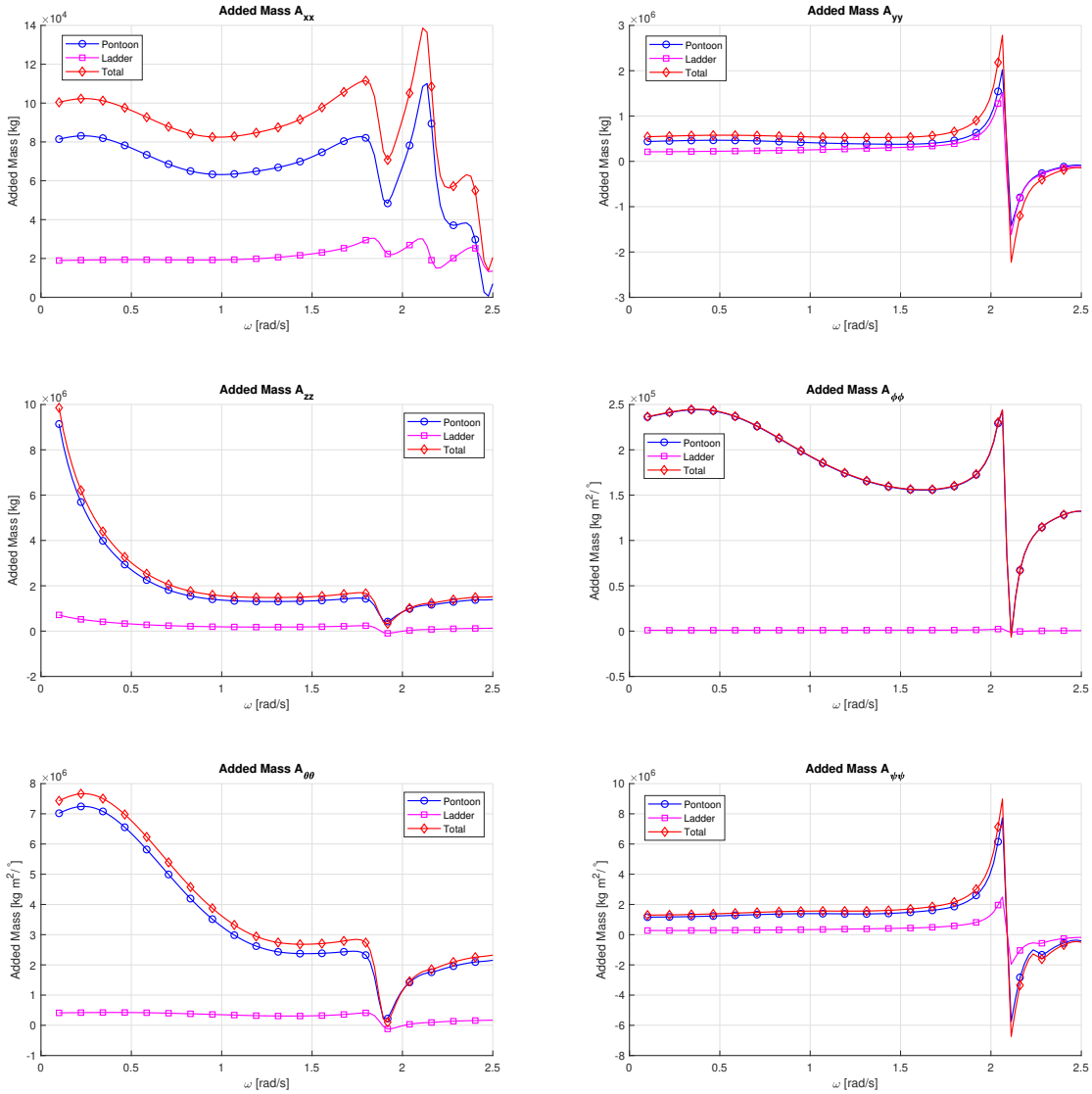

Figure 6.1: Added mass of the CSD in clamped spud configuration.

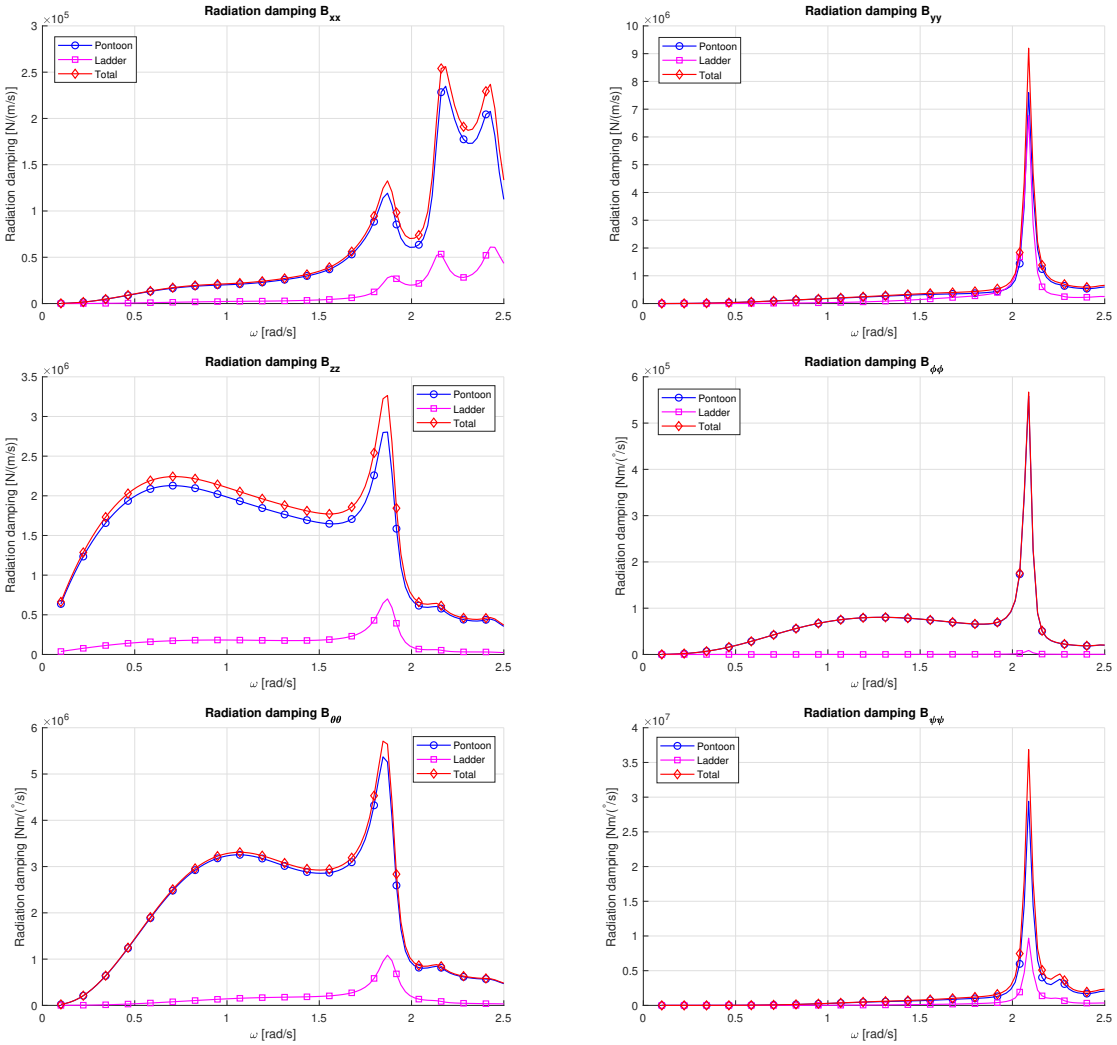

Figure 6.2: Linear radiation damping of the CSD in clamped spud configuration.

Fig. 6.1 and 6.2 show a clear decrease in added mass when comparing the clamped CSD to the free-floating CSD presented in Fig. 4.5. Furthermore, a clear increased damping frequency can be seen in both figures around ω = 2 rad/s, which is near the natural frequency of the swing wire stiffness added to the model. This damping frequency is most prominent in any motion which can induce a sway motion, in sway, roll and yaw, creating a large amount of radiation damping in this frequency when compared to the radiation damping of the free-floating CSD. These motions create the most elongation of the swing wires. These peaks have two implications for the TD model. First, there is a clear single peak around 2 rad/s, but no clear peaks for lower frequencies. As the TD model will use a JONSWAP spectrum of real-world wave data of the North Sea, it is very unlikely waves of this frequency will occur. If they do, they will be heavily damped due to these coefficients, especially for inertial forces due to the decreased added mass. Secondly, to be able to use the Cummins' EOM to transfer the FD results to a TD model, the use of retardation functions require the added mass to converge to a single value at an infinitely high frequency. It can be seen in Fig. 6.1 that this does occur.
Both these coefficients mostly impact the model by amplifying or dampening existing motion. Again, because the resonance peaks are located at very high frequencies, it is unlikely that they will have a significant effect on the TD model.

6.2. First-order wave forces

Using the hydrodynamic coefficients the first-order forces can be computed with respect to the wave frequency. Fig. 6.3 shows the distribution of the diffraction and FK forces for both the pontoon and the ladder at 5 m water depth.

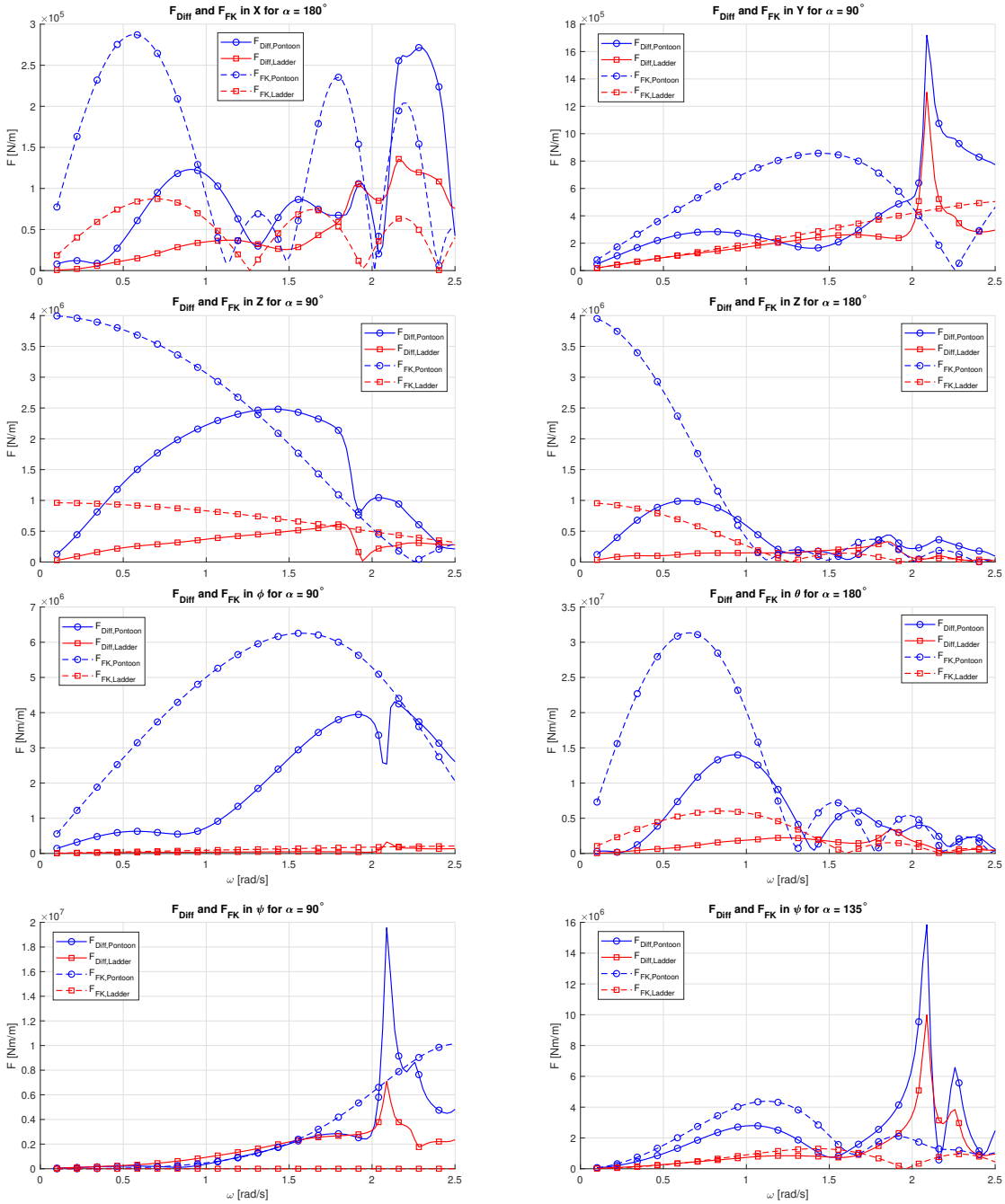

Figure 6.3: Diffraction and FK forces in FD for the clamped spud configuration.

Combining the diffraction and FK forces with the dissipation of kinetic energy due to wave radiation and viscous damping, the total wave forces can be determined. Fig. 6.4 shows the total wave forces for the CSD700 and its components.

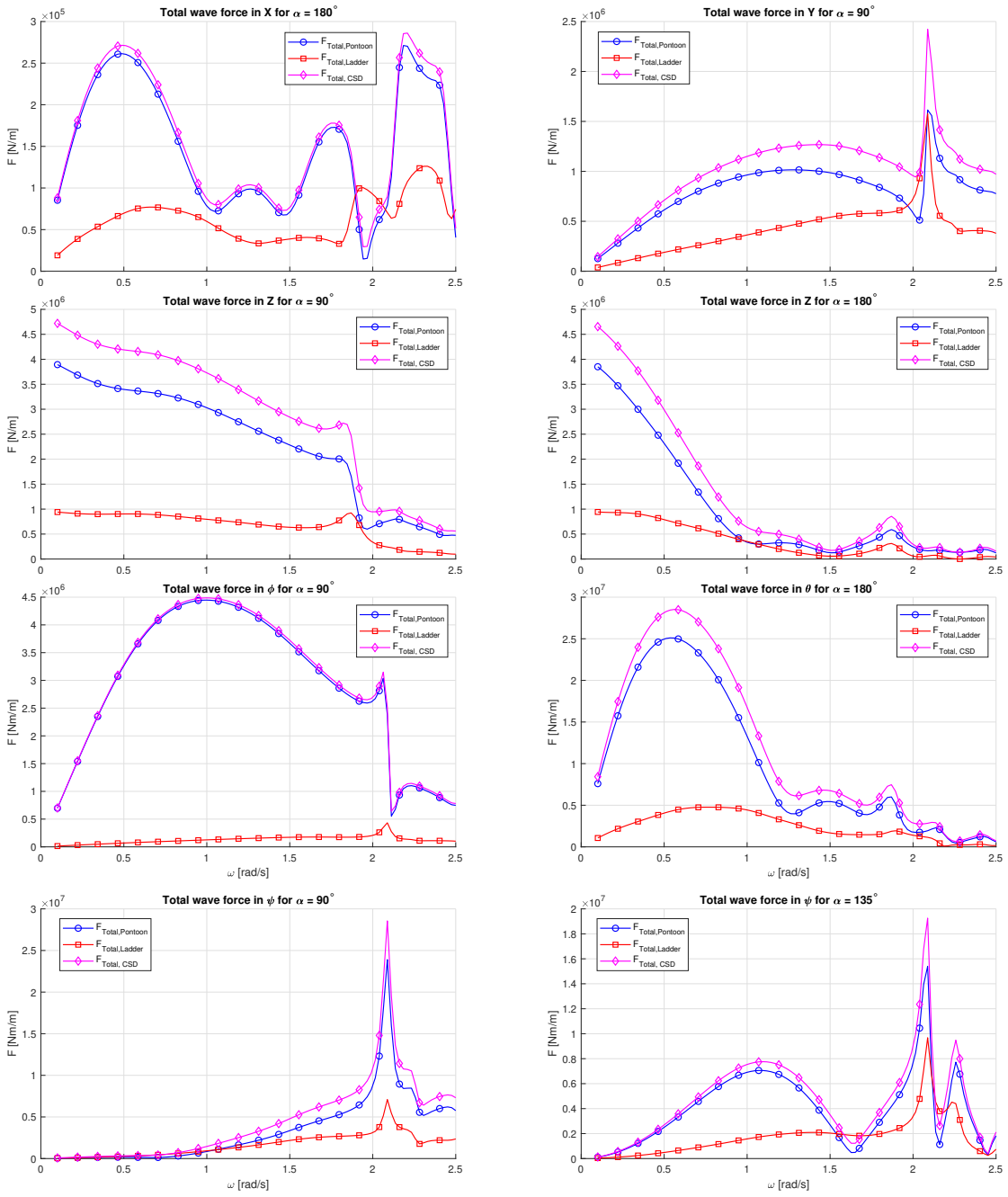

Figure 6.4: RAO results in FD for the clamped spud configuration.

The total forces cannot be simply summed, as the bodies interact with each other. For example, the ladder is only half exposed to beam waves, the other half covered by the pontoon. This reduces the total wave force the CSD compared to the sum of the forces on the individual parts. The summed forces follow from the AQWA output.

Fig. 6.3 shows that the vast majority of wave forces are induced by waves interacting with the pontoon. The wave forces exerted on the ladder will have the largest relative impact on

the heave an pitch motion of the CSD. This can be explained by the geometry of the ladder: it has the a large length compared to its breadth and is therefore more susceptible to forces which are largest in head waves, in this case most notably in pitch. The sway and yaw plots again show a peak of increased height slightly above ω = 2 rad/s, similar to the added mass and radiation damping plots in Fig. 6.1 and 6.2. These are likely caused by resonance from the added stiffness from the spud and swing wires. The position of the peak in the frequency spectrum however is such that they have little impact on the overall TD model, as real-world waves have a very low energy density at these high wave frequencies.

From the total force plots in Fig. 6.4 it can be seen that the largest translational wave forces are found in sway, which are up to ten times higher than the surge wave forces. This is caused by the fact that the area projected perpendicular to the wave direction is much larger on the side of the CSD compared to the front or back. Similarly, this effect can be seen in the heave wave force plots, where the force response is equal for low frequencies, but decays much faster in head seas than in beam seas. This could indicate an increase in operability in head seas compared to beam seas. The yaw force distribution mainly affects the stress the swing wires will be under, as they are the main counterpart to wave-induced yaw motion, together with the operational and mooring effects of the cutter ladder. It is shown that beam seas exert the largest yaw forces on the CSD, but for fairly high wave frequencies. Oblique waves at α = 135° exert a larger wave force for a wave around ω = 1 rad/s, which is a more common wave frequency in real-world wave records.

6.3. Clamped spud RAOs

Using the hydrodynamic coefficients found in this chapter and their resulting external wave forces, the RAOs for all 6 DOF of the CSD can be derived for the CS configuration. This section aims to provide insight into the effect of different water depths between 5 and 25 m on the FD response of the clamped CSD. The wave angle α for different motions is chosen based on the largest wave forces found in Fig. 6.4 in the previous section. The full spectra of wave direction RAOs, as well as base verifications of these results, are given in Appendix D.

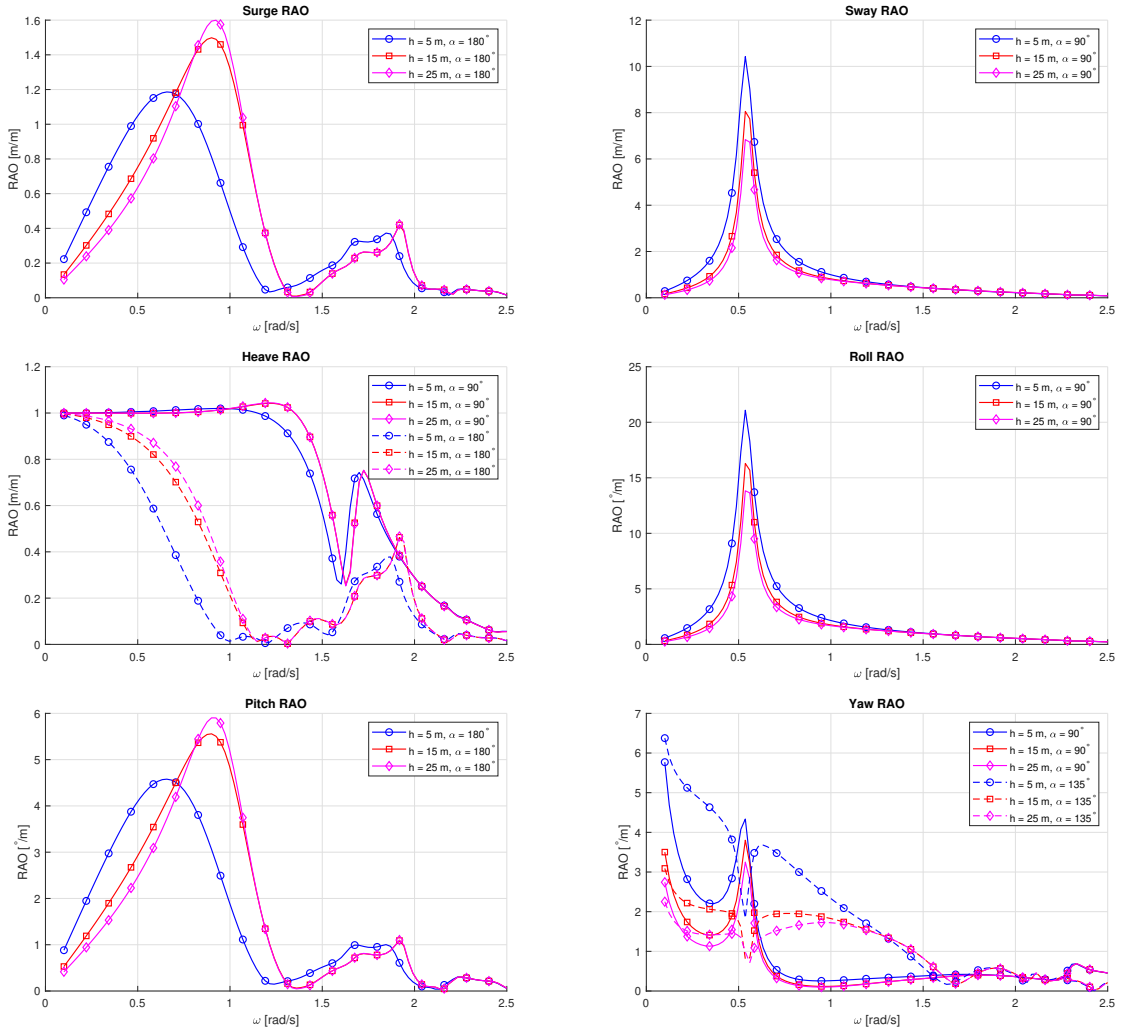

Figure 6.5: RAO results in FD for the clamped spud configuration.

Fig. 6.5 shows the RAOs of all 6 DOF of the clamped CSD in 5, 15 and 25 m water depth. As was shown in the spectral definition of a wave record in Section 2.4, the most common wave frequencies range between 0.5 and 1.5 rad/s. Every DOF of the CSD has a resonance peak in this range. It can be seen that the position of the peak varies based on if it is a head or beam sea dominant motion. The main difference in the deep sea response to the shallow water response is seen in the surge and pitch motion response. A clear shift can be seen in the resonant motion peak to lower frequencies compared to deeper seas. The amplitude of the peak is lower, but the motion response is higher in all frequencies below ω = 0.6 rad/s. This is interesting, as the overall spud stiffness is higher for shallow water due to its decreased length, and would therefore likely induce a shift to higher frequencies due to this increased stiffness. This effect is observed however in other moored vessels in shallow water [87]. The

largest pitch motion occurs when λ = 0.5 $\cdot$ L_{CSD}, as this means one end of the CSD is lifted to the amplitude of the wave peak, while the other end is in the lowest point of the wave trough. When transitioning from deep to shallow water, a wave of identical frequency changes shape due to the influence of the sea bottom and thus shortens, as was shown in the dispersion relation. A wavelength that induces this resonant pitch motion therefore has to have a longer wave period in shallow water than in deep water, thereby moving the pitch RAO of the CSD toward the lower frequency region. Secondly, it was shown that the added mass component increases for shallow water. As the natural frequency of the CSD is inversely proportional to the square root of the sum of the mass and the added mass, thereby explaining the decrease in natural frequency due to the increased added mass. This effect can also be seen in the heave motion RAO, where the heave motion is slightly reduced in shallow water, and the resonant peak around ω = 1.7 rad/s is moved to the left for 5 m water depth compared to 15 or 25 m.

In contrast to the pitch and heave motion, the sway and roll motion seem to increase in shallow water. These motions are mostly affected by a change in the projected side area and beam respectively. As the CSD moves from deep to shallow water, the ladder angle has to change such that the cutter head is in contact with the sea floor. This decreased angle both increases the side area of the CSD near the waterline, as well as the overall length of the CSD near the waterline. The fluid motion of the water is largest at the free surface (as shown in Fig. 2.3) which could describe this increase in induced sway and roll motion. As the yaw motion is heavily linked with the sway motion, the increase in yaw motion in shallow water can be explained with the same arguments. This effect can most notably be seen for α = 90°, for wave frequencies below 0.5 rad/s.

6.4. Flexible spud RAOs

Using the clamped RAOs as a benchmark to test the effectiveness of the flexible spud keepers, the RAOs for different flexible spud connections are shown in Fig. 6.6. The amount of flexibility is presented as a percentage of the original spud stiffness of the clamped configuration. Four different configurations are displayed: 0%, 5%, 10% and 20%. 0% stiffness in this case denotes added identical stiffness to the clamped spud in K_{xx} and K_{yy}, but is free to rotate in pitch and roll.

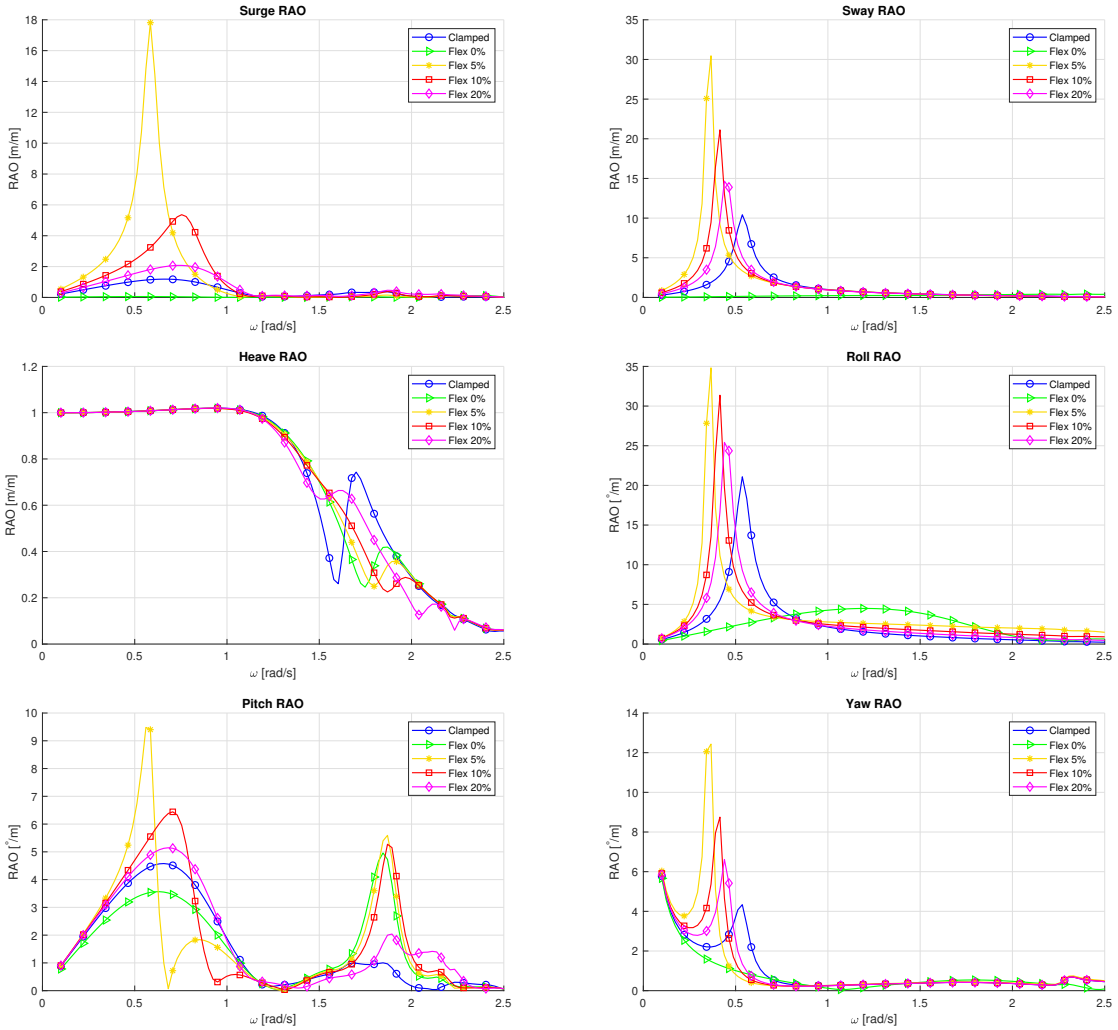

Figure 6.6: Motion RAOs of flexible spud keeper configurations at h = 5 m.

Fig. 6.6 shows the RAOs of the different flexible spud keeper connections in all 6 DOF of the CSD at a water depth of h = 5 m. The effect of this connection on the cutter head movement and the ladder angle will be discussed in Section 7.2.4, as the mooring effects of the cutter cannot be taken into account in FD. Furthermore, any flexible connections with stiffness larger than 20% only had negligible difference with the CS configuration and are therefore not considered.

From Fig. 6.6 it can be seen that the reduced stiffness has an effect on both the amplitude of the resonance peak of the RAO, as well as the position of the peak in the frequency range. Because the CSD can be described as a mass-spring system, reducing the stiffness of this spring also has to increase its natural period. The least impacted DOF is heave, as the CSD is

free to move in the heave direction the only effect the reduced stiffness has is on the coupled stiffness between heave and another DOF. Likely this DOF is pitch, due to the CSD rotating around the spud and thereby inducing an automatic heave motion when it pitches.

The remaining DOF exhibit a clear shift towards the low-frequency range. As the sway, roll and yaw RAO were already near the lower end of the wave frequencies found in most standard JONSWAP spectra, the reduced stiffness could therefore exclude any resonance in these DOF for standard waves. A risk however is resonance occurring for frequencies linked with second-order wave forces. A QTF study in TD is therefore required to accurately determine the real motion response.

A further difference can be seen in the pitch plot, where a second resonance peak emerges around 1.8 rad/s, similarly to the peak found in the free-floating CSD pitch RAO. This peak coincides with the peaks seen in the heave and pitch added mass and radiation damping plots in Fig. 6.1 and 6.2. Hydrostatic analysis of the CSD determines this peak is likely found from the hydrostatic stiffness of the CSD, which together with the total mass of the CSD would derive to a natural heave frequency of 1.71 rad/s. The fact that this peak only occurs in heave and pitch also point to this being a hydrostatic stiffness-induced peak, as these motions are strongly coupledfor a CSD.

Lastly, because the coupled stiffness components for surge-pitch and sway-roll have also been altered, the motion RAO for surge, sway and yaw have also changed with the FS configurations. In reality however, the surge and sway motion are limited to the bending displacement from the spud. The yaw motion around the spud is unrestricted in terms of the added stiffness, but is still limited due to the swing wire stiffness and the cutter-soil interaction. These plots are still shown to indicate possible changes in resonance for these motions. The motion RAOs can therefore not be one-to-one translated to real-world motions of the CSD.

7

Results and Discussion - TD

This chapter presents the results of the TD model developed in ANSYS AQWA, based on the FD model results found in Ch. 6. These results serve a dual purpose, first to verify the model to find any anomalies, and secondly to identify the components needed for the operability analysis which is needed to answer the research question. Using both these results, the full operability analysis for the different spud keeper configurations can be performed.

The Regular wave response section will first verify the choice to use Stokes 2nd order waves and other non-linear wave effects, and investigate its effects on critical elements of the operability analysis. Afterwards, example results for the four operability limits are given in the Irregular wave response section using a full JONSWAP wave record. Finally, the Operability analysis section will present the complete operability analysis for a select number of spud keeper configurations.

7.1. Regular wave response

This section compares the response of a CSD to linear, regular waves as they are used in LWT, with the response to Stokes 2nd order waves (S2). The difference in wave shape of shallow water waves compared to deep water waves is the main driving force behind the hypothesis that TD modelling is necessary for accurate modelling of a CSD in operation. This section therefore investigates the effects of this altered wave shape.

Fig. 7.1 shows the difference between the wave record used in LWT and S2. The LWT wave is purely sinusoidal, with an amplitude of 0.25 m and a period of 8 s. The S2 wave contains a single extra term added to the sinusoidal wave, based on the steepness of the wave as explained in Section 2.2.1. Using both a shoaling coefficient for a water depth of 5 m and this steepness term, the resulting wave is made up of a peak amplitude of 0.261 m and a trough amplitude of -0.244 m. This shows the difference in shape between the two wave theories; S2 waves have a sharper peak and a shallower trough. The total wave height has increased by 1.01%. This metocean condition can accurately be described to be in shallow water and the S2 zone, according to the definition by Le Mehaute [44] as shown in Fig. 2.16. The difference however is not as pronounced at it could be in extreme shallow water conditions. The full 300 s wave record for both theories is shown in Fig. 7.1.

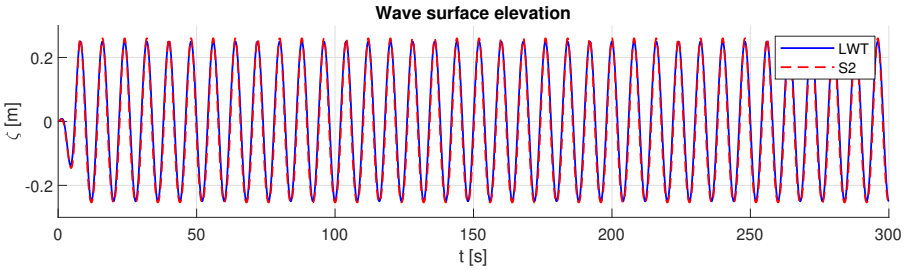

Figure 7.1: Wave surface elevation in LWT and S2, for H = 0.5 m, T_p = 8 s.

These wave records will be used to compare the wave force and motion response on the CSD, as well as the effects this has on the stress in the spud. Fig. 7.2 shows the total wave forces for heave, roll and pitch on the CSD due to either a LWT or a S2 wave. The wave directions have been chosen to reflect the largest force response for that specific DOF, similarly to Ch. 6.

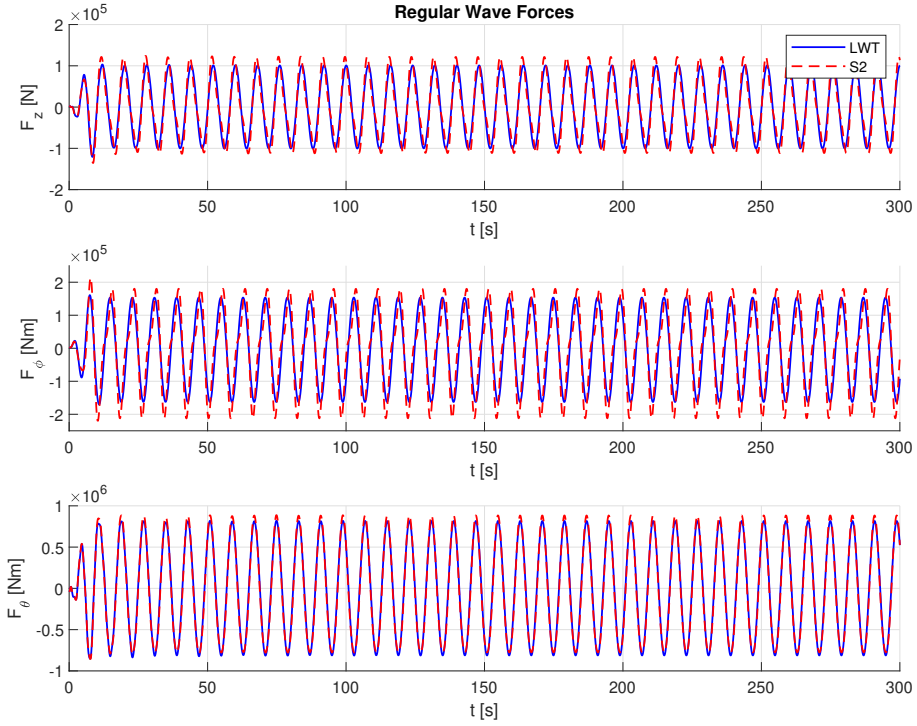

Figure 7.2: TD force response of LWT and S2 waves, for H = 0.5 m, T_p = 8 s.

The overall maxima and minima are presented in Table 7.1. The last column indicates the percentage difference from the force response of the S2 wave compared to the LWT wave. For example, the 12.5% Z_{Min} response indicates that the lowest minimum heave force response from the S2 wave is 12.5% lower than the minimum heave force response due to the LWT wave. The leftmost columns indicate the absolute value of the maximum and minimum response, indicating the highest and lowest value in the wave record.

	LWT		S2		Difference [%]	
	Min	Max	Min	Max	Min	Max
F_Z [$\cdot 10^5$ N]	-1.208	1.033	-1.359	1.242	12.5	2.0
F_ϕ [$\cdot 10^5$ Nm]	-1.703	1.609	-2.201	2.135	29.2	32.7
F_θ [$\cdot 10^5$ Nm]	-8.525	8.197	-8.572	8.878	0.5	8.3

Table 7.1: Difference in minima and maxima of the force analysis.

The forces are significantly higher in S2 compared to LWT, most notably in roll, which has a maximum roll wave force 32.7% higher in S2. These higher forces indicate that, to achieve force equilibrium, the counteracting forces from the spud or the swing wires will be higher than they would be in LWT, or the motion of the CSD has to increase.

Fig. 7.3 shows the motion in heave, roll and pitch of the CSD in response to both wave records. Again, the wave records from Fig. 7.1 have been used.

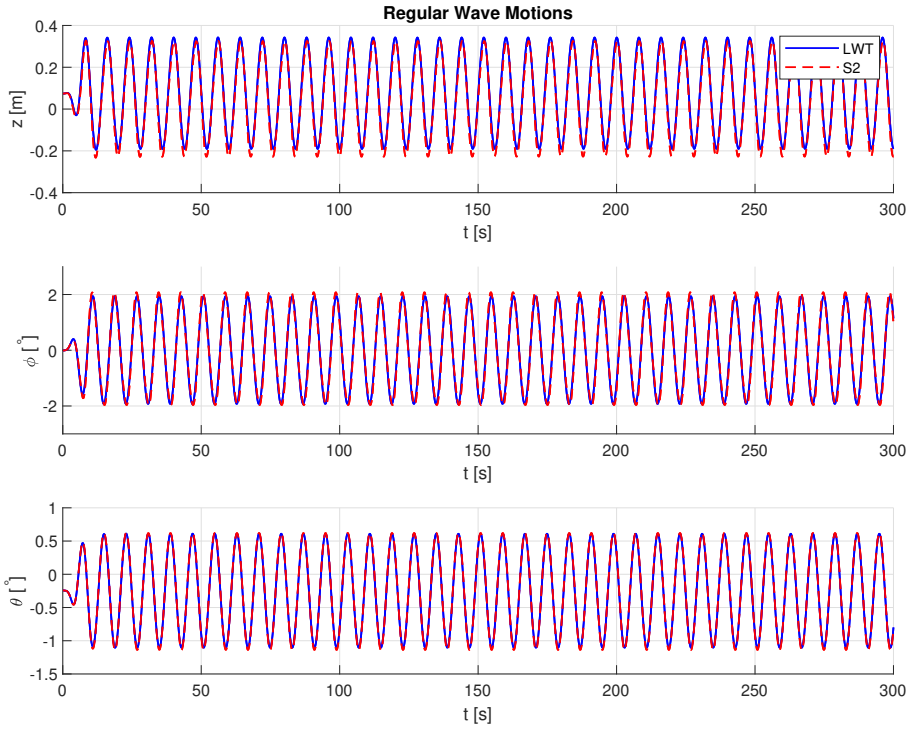

Figure 7.3: TD motion response of LWT and S2 waves, for H = 0.5 m, T_p = 8 s.

The motion maxima and minima are presented in Table 7.2. Again, the last column indicates the increase in motion due to a S2 wave compared to the LWT wave. Negative motions indicate a motion in the negative direction.

	LWT		S2		Difference [%]	
	Min	Max	Min	Max	Min	Max
Z [m]	-0.195	0.342	-0.232	0.327	19.2	-4.9
ϕ [°]	-1.926	1.940	-1.965	2.1	2.0	7.2
θ [°]	-1.105	0.612	-1.139	0.623	3.1	1.7

Table 7.2: Difference in minima and maxima of the motion analysis.

Both the pitch and roll motion response are increased in the S2 wave compared to the LWT wave. Remarkably however, the heave motion response peak is about 5% lower for S2 than LWT, even though the overall heave wave force has increased. The minimum heave response is 19.2% lower for S2 than LWT. This indicates that the CSD will tend to lift less in shallow water, but submerge further. This is interesting considering that a S2 wave has both a higher peak and a higher trough compared to LWT. For all three DOF it is clear that the S2 wave increases the overall motion of the CSD.

Using the force equilibrium principle and the motion response from Fig. 7.3, the bending stress on the spud can be calculated. Fig. 7.4 shows the bending stress σ_b in X and Y direction, relative to the maximum bending stress of S355 steel. An extra limit is given in the maximum allowable bending stress for steel of σ_{MA} = 0.66 · σ_{max}, where σ_{max} is the maximum bending stress of the spud, as used by DNV [18] for steel tubular members. The stresses have been calculated from the complete range of wave forces for all 6 DOF.

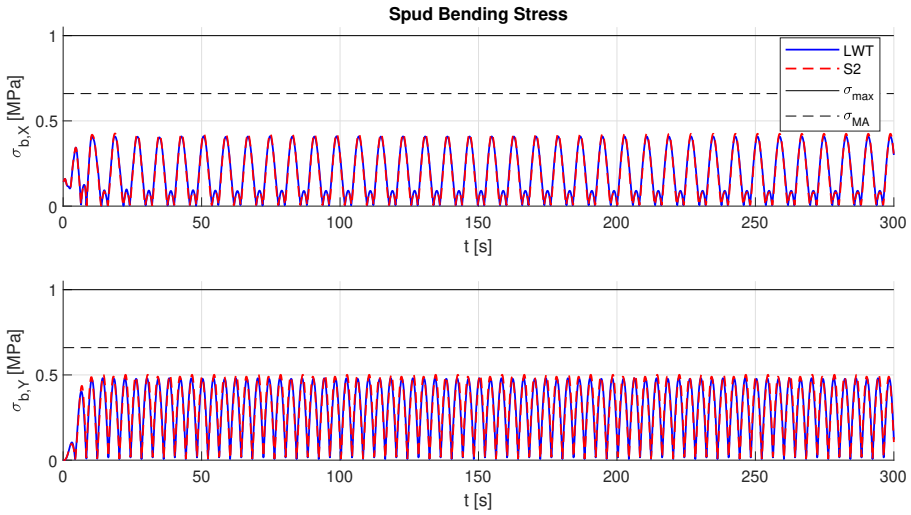

Figure 7.4: Spud bending stress response of LWT and S2, for H = 0.5 m, T_p = 8 s.

Table 7.3 shows the difference between the minima and maxima of the spud stress over the complete wave record. Negative stresses denote a stress in the negative direction.

	LWT		S2		Difference [%]	
	Min	Max	Min	Max	Min	Max
$\sigma_{b,X}$ [MPa]	-44.47	145.46	-45.61	151.30	2.5	4.0
$\sigma_{b,Y}$ [MPa]	-169.50	170.75	-174.33	177.97	2.89	4.2

Table 7.3: Difference in minima and maxima of the spud stress analysis.

Fig. 7.4 and Table 7.3 indicate an increase in spud stress for all DOF. The asymmetry of the CSD and the effects can clearly be seen on the stress plot. A beam wave induces a stress in both the positive and negative y-direction over the course of a single wave in equal amount. The stress in x-direction however mostly occurs in bending in the positive x-direction.

Similar to the wave forces and motions, the stress maxima have increased more than the increase in wave height (4.2% stress increase vs. a 1.01% increase in overall wave height). The altered wave shape therefore does impact these results more than a simple increase in the wave height of a linear wave would have done. It can therefore be concluded that a LWT wave cannot accurately describe the force, motion or stress response of the CSD in shallow water. As this thesis aims to highlight the shallow water response, all remaining results will be modelled using S2 wave shapes.

7.2. Irregular wave response

In the remaining TD simulations, a JONSWAP wave record is used with peak enhancement factor γ = 3.3, which is deemed most suitable for coastal waters in the North Sea. A 3-hour wave record is created, and using the reduced time domain method put forth in Section 5.3.1, a 300 s section is chosen containing the highest individual wave amplitude, such that the TD analysis can be performed with a reduced computing time, while still being able to investigate the most extreme wave conditions found within that wave record. The resulting CSV-file is then imported into ANSYS AQWA. Fig. 7.5 shows an example of a generated wave record using this method, for H_s = 0.5 m and T_p = 8 s.

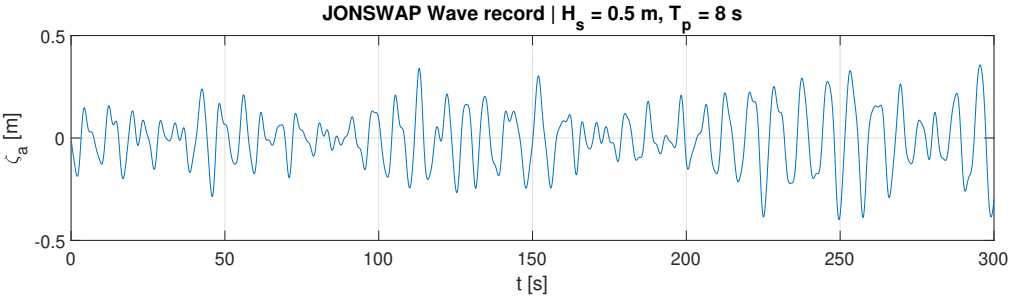

Figure 7.5: JONSWAP wave record using the reduced time domain method.

This section will investigate the results of the TD model and use these results to create an operability analysis for a CS configuration and the flexible spud connections provided in Ch. 6. The force-limited connection described in Ch. 5 is analysed afterwards as it is a combination of the previous configurations.

The four main aspects of a CSD in operation that will be investigated are:

- **Pontoon motion and acceleration:** Excessive motion and acceleration of the pontoon can cause dangerous situations for personnel on board due to shifting items on deck, or due to the way it changes important operational aspects such as the side angle of cables within their pulleys.
- **Spud stress and soil failure around the spud:** The spud is the main contributor to the station keeping of the CSD and is therefore the sole counteracting force for most wave forces endured by the CSD. As discussed in Section 3.3, the force on the spud tip below the mudline acts as an extra operability check to prevent plastic soil deformation.
- **Cutter head movement:** In order for the CSD to be able to operate, the cutter head should always be in contact with the breach. This operability limit will be checked based on the angle of the ladder and the resulting vertical motion of the cutter head.
- **Swing wire tension and winch failure:** Using the undercutting method, the swing wires need to be able to withstand the tension from operational forces, as well as major wave forces as they provide the main counter force to any wave-induced yaw motion.

The absolute values that constitute the operability limits are arbitrary, as this project aims to compare the different spud keeper configurations with the original CS construction and their relative differences. These aspects were chosen as they were deemed to see the largest change when the spud keeper flexibility is altered. This is however not the full picture when investigating CSD operability. Other important conditions such as the stress on the floating pipeline, the stress in the auxiliary spud or local forces on the cutter teeth are not taken into account. Proper operability analysis should include the full spectrum of operability conditions,

but they were deemed beyond the scope of this project. Furthermore, due to the large amount of simulations that have to be run to complete a full operability analysis, it was chosen to limit the wave directions to head and beam seas with the CSD positioned in the center of the swing. The actual operability might be reduced when the CSD reaches one of the swing angle extremities, but these are also considered beyond the scope of the project.

7.2.1. Second-order wave forces

The FD analysis of flexible spud keeper connections have shown a shift in the motion response of the CSD toward the lower frequency spectrum. This effect would remove part of the resonance from the first-order wave spectrum, however it might cause a larger response from low-frequency wave forces. As was shown in Section 4.4.4, the second-order wave forces can be analysed in the form of a QTF-matrix. The QTF-matrices will be described in two parts: the sum QTF-matrix, which includes high-frequency effects from wave interaction, and the difference QTF-matrix which includes the low-frequency effects. Especially the difference QTF can have a significant impact on FS configurations due to the aforementioned shift in the motion RAO. Fig. 7.6 shows the combined sum and difference QTFs for a number of spud keeper configurations in pitch motion.

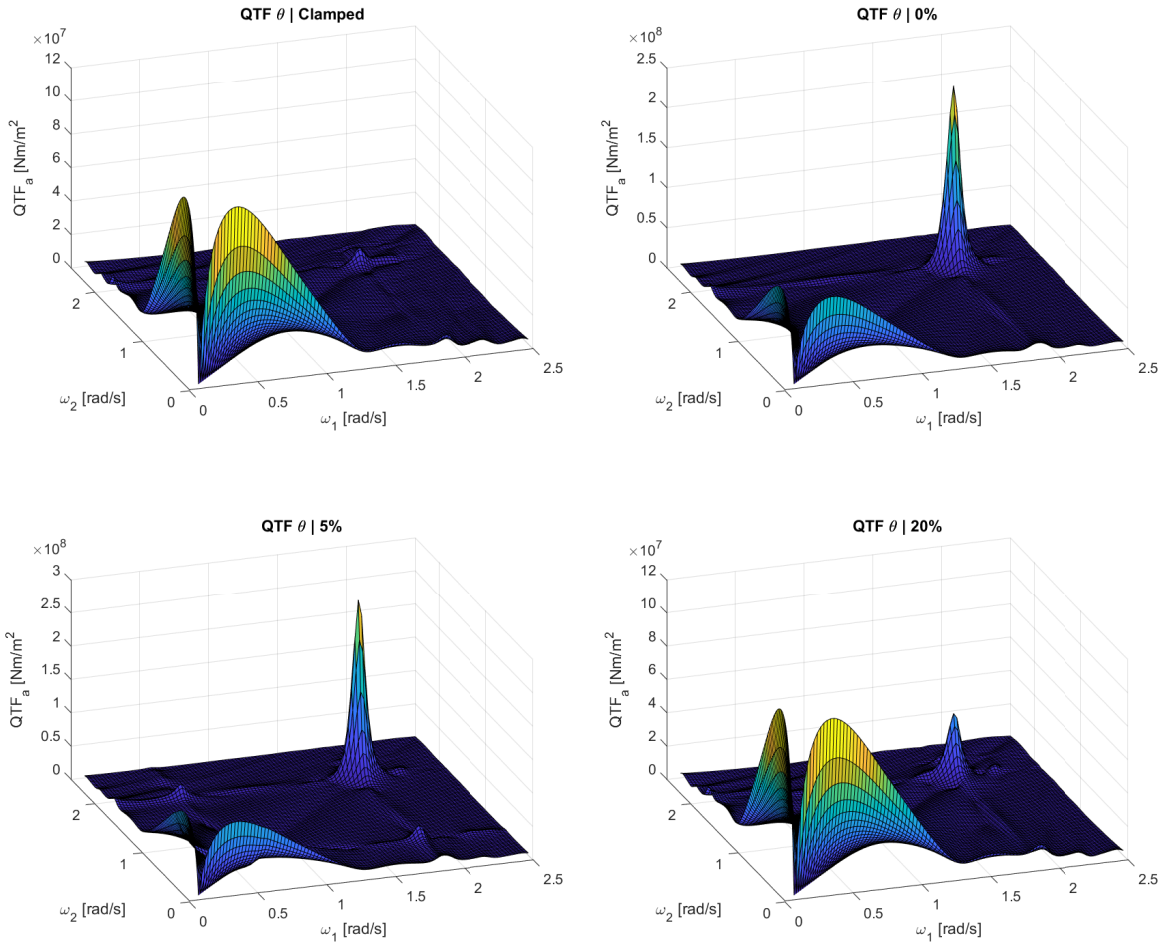

Figure 7.6: Sum and difference QTFs in pitch.

From Fig. 7.6 it can be seen that there are no real differences in the low-frequency response, regardless of the flexibility of the spud keeper connection. A major peak is seen at the combination of 0.4 rad/s for either wave frequency with a very low frequency of the other wave. The

flexibility has no effect on either the amplitude or the resonant frequency of this peak. The sum QTF however results in a peak at higher frequencies, if both interacting waves have a frequency of 1.86 rad/s. This peak corresponds to the same peak seen in the pitch motion RAO at 1.86 rad/s in Fig. 6.6 for any configurations with increased flexibility. It is therefore logical that two interacting waves at this frequency have a significant response.

7.2.2. Spud forces

Fig. 7.7 and 7.8 show an example of the maximum wave force and moment exerted on the clamped spud CSD during a 300 s wave record for translational and rotational motions respectively. Together with the known forces from the swing wires and the cutter, the force on the spud is found from the force equilibrium.

Hs											
2	1,76E+06	3,91E+05	3,16E+05	4,14E+05	7,98E+05	7,20E+05	5,70E+05	5,99E+05	6,49E+05	6,19E+05	6,04E+05
1,9	1,38E+06	3,46E+05	2,92E+05	3,78E+05	7,34E+05	6,72E+05	5,28E+05	5,56E+05	5,83E+05	5,67E+05	5,71E+05
1,8	1,21E+06	3,04E+05	2,68E+05	3,63E+05	6,79E+05	6,31E+05	4,84E+05	5,17E+05	5,30E+05	5,07E+05	5,30E+05
1,7	1,04E+06	2,62E+05	2,44E+05	3,43E+05	6,01E+05	6,08E+05	4,43E+05	4,75E+05	4,78E+05	4,40E+05	4,90E+05
1,6	8,86E+05	2,26E+05	2,23E+05	3,21E+05	5,66E+05	5,69E+05	4,00E+05	4,31E+05	4,34E+05	3,74E+05	4,32E+05
1,5	7,49E+05	1,91E+05	2,03E+05	2,98E+05	5,35E+05	5,24E+05	3,63E+05	3,86E+05	3,88E+05	3,13E+05	3,81E+05
1,4	6,34E+05	1,65E+05	1,84E+05	2,64E+05	4,97E+05	4,63E+05	3,33E+05	3,56E+05	3,43E+05	2,85E+05	3,51E+05
1,3	5,32E+05	1,48E+05	1,67E+05	2,40E+05	4,46E+05	4,14E+05	2,89E+05	3,30E+05	3,09E+05	2,57E+05	3,19E+05
1,2	4,50E+05	1,32E+05	1,49E+05	2,12E+05	4,08E+05	3,61E+05	2,55E+05	3,06E+05	2,67E+05	2,28E+05	2,91E+05
1,1	3,70E+05	1,21E+05	1,36E+05	1,85E+05	3,86E+05	3,20E+05	2,34E+05	2,74E+05	2,30E+05	2,00E+05	2,60E+05
1	3,00E+05	1,07E+05	1,23E+05	1,64E+05	3,64E+05	2,86E+05	2,08E+05	2,41E+05	2,06E+05	1,73E+05	2,31E+05
0,9	2,51E+05	92669	1,11E+05	1,47E+05	3,28E+05	2,49E+05	1,87E+05	2,08E+05	1,83E+05	1,49E+05	1,93E+05
0,8	2,14E+05	79428	1,00E+05	1,31E+05	2,95E+05	2,12E+05	1,65E+05	1,75E+05	1,59E+05	1,31E+05	1,59E+05
0,7	1,77E+05	70980	88698	1,17E+05	2,51E+05	1,76E+05	1,47E+05	1,49E+05	1,43E+05	1,13E+05	1,33E+05
0,6	1,44E+05	63109	78921	1,00E+05	2,18E+05	1,37E+05	1,29E+05	1,26E+05	1,22E+05	98687	1,06E+05
0,5	1,14E+05	57465	67995	84989	1,86E+05	1,08E+05	1,13E+05	1,04E+05	1,04E+05	85117	85450
0,4	86944	55711	59488	71801	1,49E+05	86711	97835	85051	87917	72258	69980
0,3	70391	54425	55751	57376	1,18E+05	74528	81077	72626	71566	63323	62362
0,2	62581	52828	52872	49379	92099	64207	64956	63030	60279	58915	58158
0,1	55424	51286	50672	49565	58128	52064	54742	53955	54389	54251	53924
Tp	3,5	4,5	5,5	6,5	7,5	8,5	9,5	10,5	11,5	12,5	13,5

Figure 7.7: Translational wave forces on the CSD, for α = 180°.

Hs											
2	6,46E+06	3,91E+06	4,01E+06	4,93E+06	5,26E+06	4,24E+06	3,99E+06	3,45E+06	3,37E+06	3,32E+06	3,43E+06
1,9	5,71E+06	3,69E+06	3,86E+06	4,68E+06	4,91E+06	3,90E+06	3,61E+06	3,27E+06	3,19E+06	3,13E+06	3,25E+06
1,8	5,11E+06	3,52E+06	3,63E+06	4,50E+06	4,57E+06	3,68E+06	3,33E+06	3,09E+06	3,01E+06	2,95E+06	3,06E+06
1,7	4,61E+06	3,32E+06	3,41E+06	4,21E+06	4,25E+06	3,47E+06	3,06E+06	2,92E+06	2,83E+06	2,77E+06	2,87E+06
1,6	4,16E+06	3,13E+06	3,20E+06	3,95E+06	3,94E+06	3,26E+06	2,82E+06	2,74E+06	2,67E+06	2,60E+06	2,69E+06
1,5	3,69E+06	2,93E+06	2,99E+06	3,66E+06	3,67E+06	3,05E+06	2,56E+06	2,56E+06	2,49E+06	2,42E+06	2,51E+06
1,4	3,36E+06	2,73E+06	2,62E+06	3,36E+06	3,36E+06	2,84E+06	2,33E+06	2,38E+06	2,31E+06	2,25E+06	2,33E+06
1,3	3,02E+06	2,53E+06	2,45E+06	3,15E+06	3,09E+06	2,63E+06	2,16E+06	2,21E+06	2,14E+06	2,07E+06	2,16E+06
1,2	2,67E+06	2,34E+06	2,28E+06	2,90E+06	2,81E+06	2,42E+06	2,00E+06	2,03E+06	1,97E+06	1,90E+06	1,98E+06
1,1	2,36E+06	2,15E+06	2,11E+06	2,67E+06	2,58E+06	2,21E+06	1,84E+06	1,86E+06	1,80E+06	1,73E+06	1,80E+06
1	2,04E+06	1,98E+06	1,91E+06	2,45E+06	2,34E+06	2,01E+06	1,67E+06	1,69E+06	1,62E+06	1,57E+06	1,63E+06
0,9	1,75E+06	1,79E+06	1,73E+06	2,22E+06	2,15E+06	1,80E+06	1,52E+06	1,51E+06	1,46E+06	1,40E+06	1,45E+06
0,8	1,48E+06	1,61E+06	1,55E+06	1,99E+06	1,97E+06	1,59E+06	1,37E+06	1,34E+06	1,29E+06	1,24E+06	1,28E+06
0,7	1,22E+06	1,42E+06	1,37E+06	1,76E+06	1,75E+06	1,39E+06	1,22E+06	1,17E+06	1,12E+06	1,07E+06	1,11E+06
0,6	9,93E+05	1,22E+06	1,18E+06	1,53E+06	1,54E+06	1,19E+06	1,07E+06	1,00E+06	9,62E+05	9,15E+05	9,45E+05
0,5	7,87E+05	1,02E+06	9,95E+05	1,28E+06	1,29E+06	1,01E+06	8,83E+05	8,36E+05	7,97E+05	7,54E+05	7,77E+05
0,4	5,84E+05	8,30E+05	8,03E+05	1,04E+06	1,02E+06	8,40E+05	7,07E+05	6,67E+05	6,35E+05	5,94E+05	6,10E+05
0,3	4,17E+05	6,28E+05	6,12E+05	7,93E+05	7,62E+05	6,46E+05	5,33E+05	4,99E+05	4,74E+05	4,37E+05	4,47E+05
0,2	2,82E+05	4,23E+05	4,11E+05	5,39E+05	5,26E+05	4,46E+05	3,71E+05	3,33E+05	3,12E+05	2,99E+05	2,83E+05
0,1	1,45E+05	2,15E+05	2,06E+05	2,73E+05	2,65E+05	2,33E+05	1,87E+05	1,59E+05	1,51E+05	1,55E+05	1,35E+05
Tp	3,5	4,5	5,5	6,5	7,5	8,5	9,5	10,5	11,5	12,5	13,5

Figure 7.8: Rotational wave moments on the CSD, for α = 180°.

From the force equilibrium of the complete system the resulting bending stress in the spud can be determined. Fig. 7.9 shows the bending stress of a range of spud keeper configurations and how they relate to the maximum allowable bending stress σ_{MA}. $\sigma_{b,X}$ was measured for α = 180° and $\sigma_{b,Y}$ for α = 90°. The force used to calculate the bending stress is found using the square root of the x- and y-component of the wave force squared.

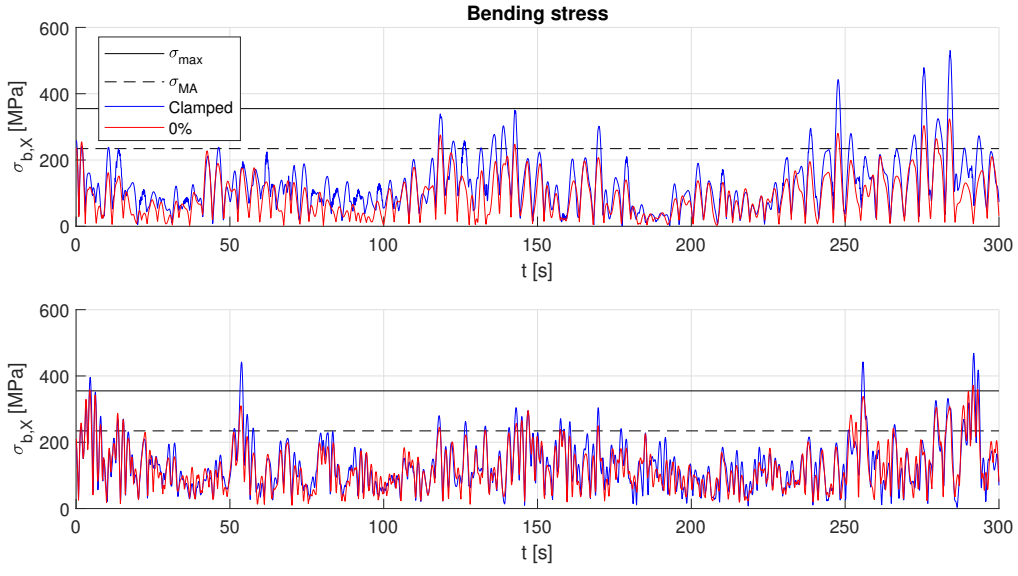

Figure 7.9: Spud bending stress, for H_s = 1 m and T_p = 9 s.

From Fig. 7.9 it can be seen that there is a significant difference in the bending stress of the spud for both wave directions. A 9 s wave period is characteristic for pitch motion, as

was shown in its motion RAO, but the bending stress response for beam seas is of a similar magnitude, with a higher average stress. This could indicate that the best operability for a CSD occurs when pointing directly into the incoming waves. Standard practice and empirical evidence already suggest this, but it can be confirmed using this data.

The differences among the different spud keeper configurations are most pronounced in head seas, with the maximum bending stress for a 0% FS configuration for this particular time series being only 61.1% of the maximum bending stress in the CS configuration. The reduction in stress for a flexible connection in beam seas is still significant however, at 79% maximum stress of the original CS connection. This is most likely caused by the fact that motion in head seas purely consists of induced surge and pitch motion, but in beam seas there is an extra pitch component alongside the sway and roll motions, due to the asymmetry of the CSD when pitching around the spud. Using this data, the operability analysis for spud bending stress is performed, as shown in Fig. 7.10 and 7.11. For this analysis the response in head seas is highlighted, as this is the preferred dredging method in almost all cases.

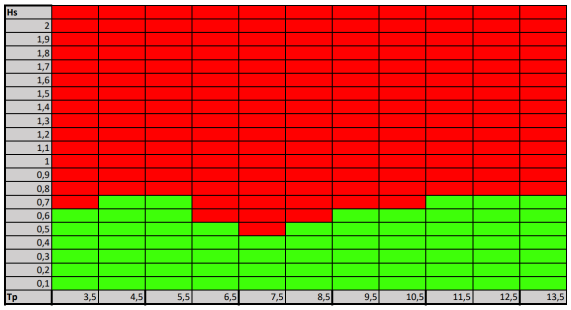

Figure 7.10: Spud bending stress operability for CS configuration, α = 180°.

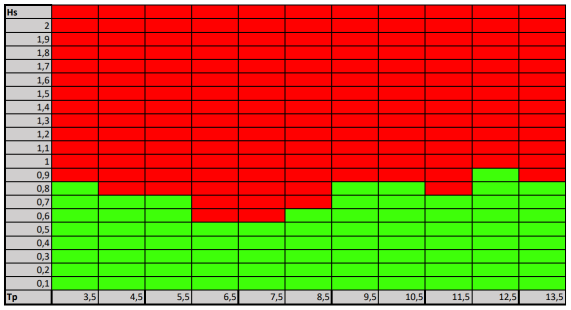

Figure 7.11: Spud bending stress operability for 0% FS configuration, α = 180°.

The operability scatter tables show a clear increase in operability for the 0% FS configuration compared to the CS connection. This effect is especially noticeable for wave periods below 11 s, where the added flexibility causes a larger operability window for almost all cases. The shift in motion RAO can also clearly be seen, as the 0% FS connection is not as limited around 7.5 s. The new resonance peak's effect on the stress is seen at 11.5 s, where a slightly reduced operability is shown compared to CS.

The operability of the spud is limited by the allowable bending stress of the spud itself, but also the lateral load capacity of the soil, as discussed in Ch. 3. The ultimate soil capacity for the rotational spring model was found in Section 3.3. It was determined that plastic soil deformation was unlikely to occur if the force at the spud tip remains below 90% of the ultimate lateral load capacity. The exceedance of this soil failure limit can now be done using [88]:

$$H_u = \frac{\int_0^{L_{pen}} (p_u \cdot D_{spud} \cdot z)\, dz}{e} \tag{7.1}$$

Where H_u is the force at the spud tip and e is the loading eccentricity. Using the penetration depth of 2.13 m and the ultimate lateral load capacity p_u of 178 kN/m, the maximum load at the spud tip results in H_u = 410 kN.
The effect of the implementation of the rotational soil spring model is checked using the stiffness found for a constant shear stress distribution G_0, as was shown in Section 3.3, Fig. 3.8. This results in the following moment-rotation relation, as shown in Fig. 7.12.

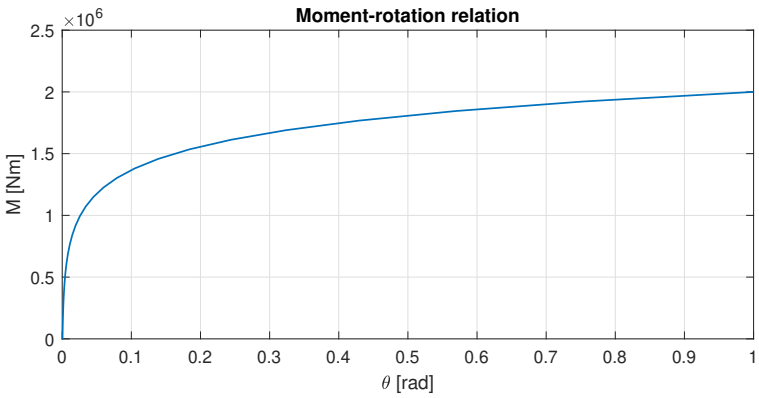

Figure 7.12: Relation between the moment and the rotation of the rotational spring model.

Using this relation, the spud rotation and the resulting horizontal motion at the mudline are investigated in Fig. 7.13.

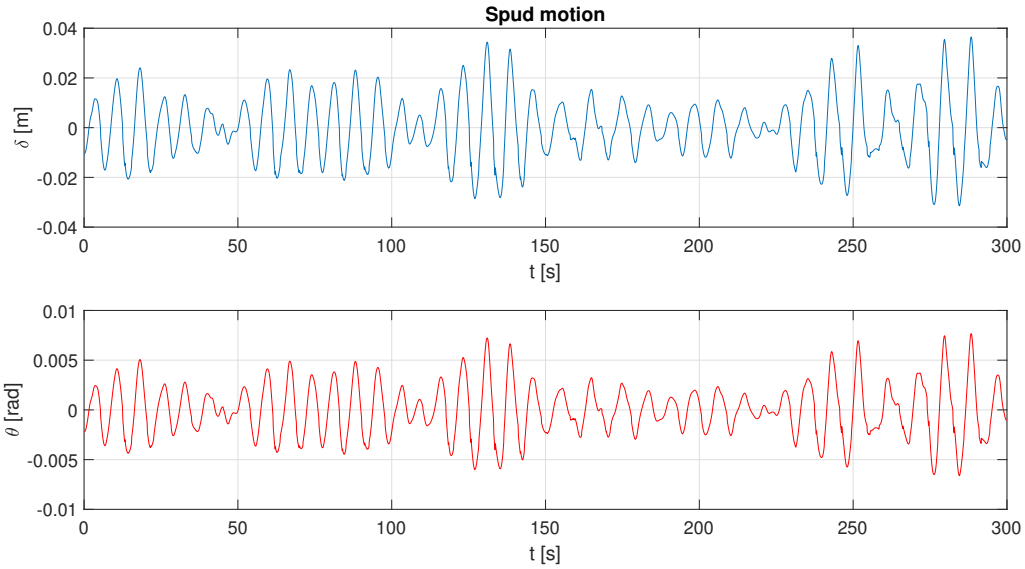

Figure 7.13: Spud motion and rotation in head seas, for H_s = 1 m and T_p = 9 s.

These results show the spud motion response in the exact wave record used to analyse the spud bending stress. The rotation found is very small, maximising at 0.0077 rad or 0.44°, which corresponds to a 3.6 cm deflection at the mudline, or a 12.1 cm horizontal shift at the spud clamp. The maximum bending stress in this situation has however long been exceeded. It can therefore be assumed that if the limiting spud tip force is exceeded, the spud would have failed in bending first.

7.2.3. Motions

Increased flexibility will likely lead to increased motion of the CSD, which makes it an important operability limit. The spud force analysis showed the largest bending stress is induced due to pitch motion of the CSD, so this section will also investigate the pitch and heave motion. The actual motion limit is fully dependent on the specific design of the components on deck, so an arbitrary limit of 2° allowable pitch rotation was chosen. These motions govern limits such as wire angles in pulleys and the motion response of the cutter ladder, but indirectly influences

extra operational limits such as the stress in the floating pipeline. An example of the heave and pitch response is shown in Fig. 7.14.

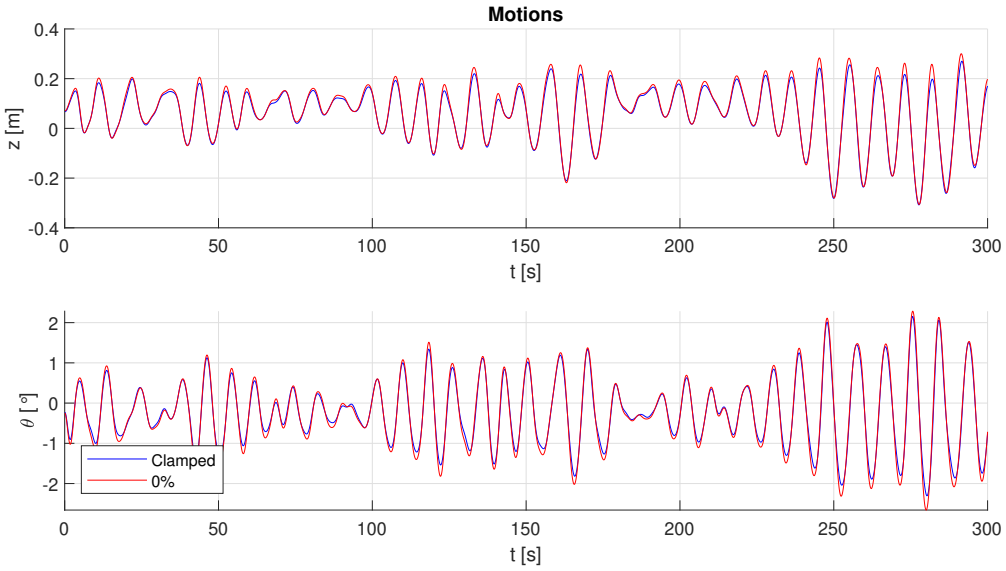

Figure 7.14: Heave and pitch motions in head seas, for H_s = 1 m and T_p = 9 s.

From Fig. 7.14 it can be seen that there is a clear increase in both heave and pitch motion for a 0% FS configuration compared to a clamped spud. Investigation of pure heave motion shows that the increase in heave is primarily caused by the increased pitch motion, as opposed to significant difference in the heave response. The operability scatter tables follow from the motion response as shown in Fig. 7.15 - 7.18.

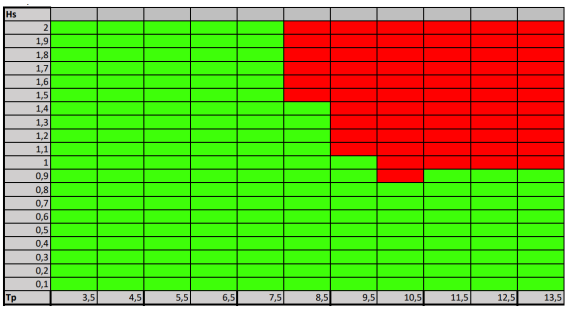

Figure 7.15: Heave motion operability limit for CS configuration.

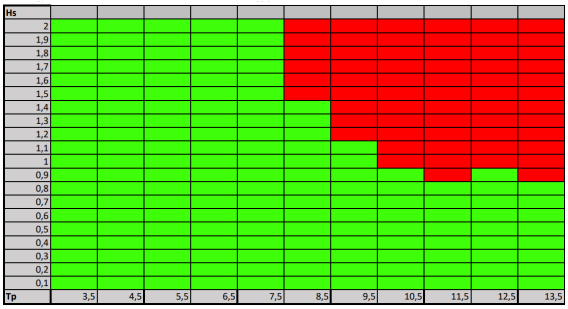

Figure 7.16: Heave motion operability limit for 0% FS configuration.

The operability scatters show the largest difference in response is found in the pitch motion. Interestingly, the main increase in pitch motion for the FS configuration is seen in very small wave periods. This response was also shown in the secondary peak which emerged in the pitch motion RAO from the FD results. The lowest allowable wave height is seen at H_s = 0.8 m and T_p = 8.5 s, corresponding to the main resonance peak of the pitch motion RAO. The overall shape of the operability limit is fairly similar for both heave and pitch with no practical difference for wave periods above 5.5 s, except for a slight decrease in operability for pitch motion for T_p = 10.5 s, where the CS configuration induces a larger pitch motion. This could indicate that the shift in the resonance peak towards lower frequencies for the FS configurations could result in smaller motions in real sea-states.

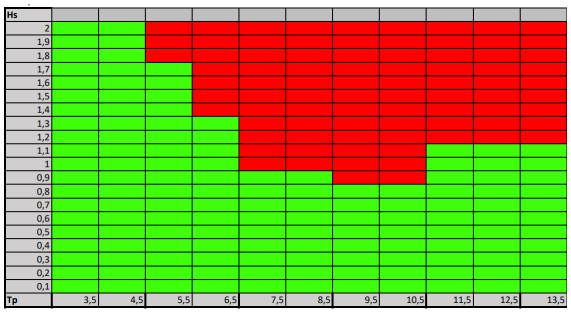

Figure 7.17: Pitch motion operability limit for CS configuration.

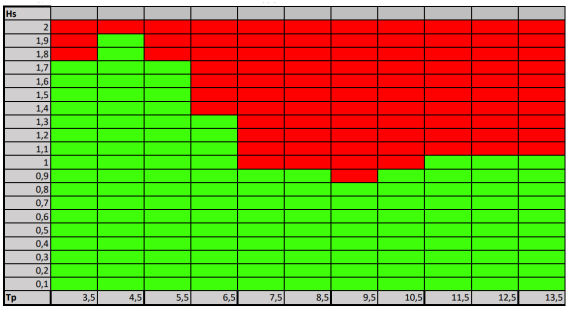

Figure 7.18: Pitch motion operability limit for 0% FS configuration.

Absolute motion limits can however differ wildly depending on the specifics of the design of the mechanical components on deck. Most working vessels therefore use acceleration limits to govern the workability, which for a CSD mainly include the pitch acceleration to prevent shifting of objects and the well-being of the crew [55]. From the time series of absolute motion the pitch acceleration can be obtained, as shown in Fig. 7.19.

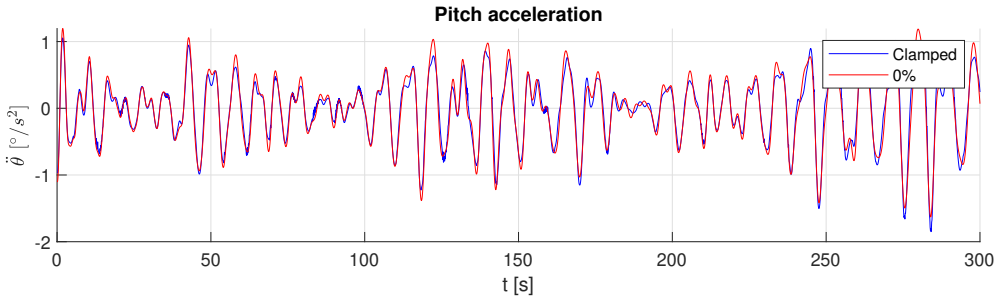

Figure 7.19: Pitch acceleration in head seas, for H_s = 1 m and T_p = 9 s.

The operability results for pitch acceleration in head seas are shown in Fig. 7.20 and 7.21.

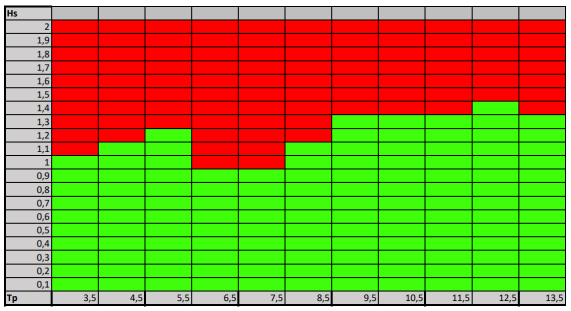

Figure 7.20: Pitch acceleration operability limit for CS configuration.

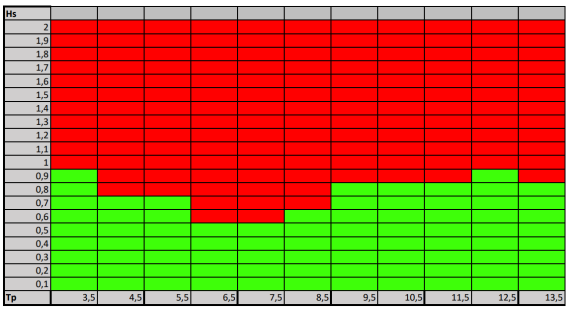

Figure 7.21: Pitch acceleration operability limit for 0% FS configuration.

These results illustrate a significant increase in acceleration for 0% FS across all wave periods. The operability is based on the largest acceleration value in the time series. The overall workability for CS is 58.2% and decreases to 36.4% for the 0% FS configuration. The operability is severely reduced when examining acceleration compared to absolute motion, where acceleration becomes the governing limit for a number of wave periods for the 0% FS configuration, compared to the spud bending stress limit.

7.2.4. Cutter head movement

The contact of the cutter head with the breach is a core principle of the workability of a CSD. Any significant lift would decrease the production of the CSD, and excessive pushing of the cutter head into the breach can damage to the cutter itself. Because the ladder is a modelled as a separate body from the pontoon, its motion response is a combination of the pontoon motion and its own motion response to a wave. Fig. 7.22 and 7.23 show the motion RAO of the ladder as a single body in heave and pitch respectively.

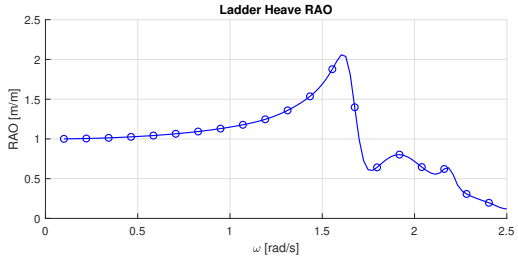

Figure 7.22: Heave RAO of the ladder, for α = 90°.

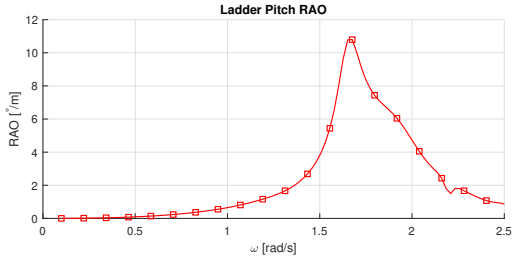

Figure 7.23: Pitch RAO of the ladder, for α = 180°.

From these figures it can be seen that the ladder has its most significant motion response above 1.5 rad/s. These peaks can also partly be seen in the RAOs of the complete CSD in Fig. 6.5 and 6.6. From these FD responses, the TD response for the vertical motion of the cutter head and the ladder pitch angle are calculated. These results are illustrated for a head sea wave record in Fig. 7.24.

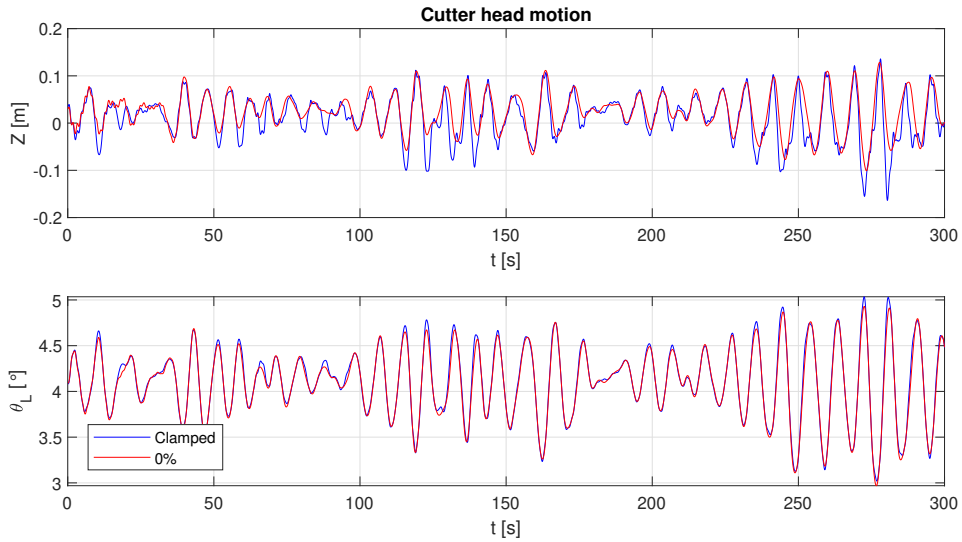

Figure 7.24: Cutter head motion comparison, for H_s = 1 m, T_p = 9 s.

It is important to note that the ladder angle is a combination of the pontoon motion and the specific hydrodynamic response of the ladder. This means that a change in ladder angle does not necessarily result in a lifting motion of the cutter head. From Fig. 7.24 it can be seen that the effect of flexibility is largest in the vertical motion of the ladder but not as pronounced in the ladder angle. This indicates that the ladder behaves and moves mostly independently of the pontoon. The ladder angle stays mostly similar, but there is a clear decrease in vertical motion in the 0% FS configuration. This could indicate a damping effect on the ladder motion from the motion of the pontoon. Using these results, the operability scatter tables are created and shown in Fig. 7.25 and 7.26.

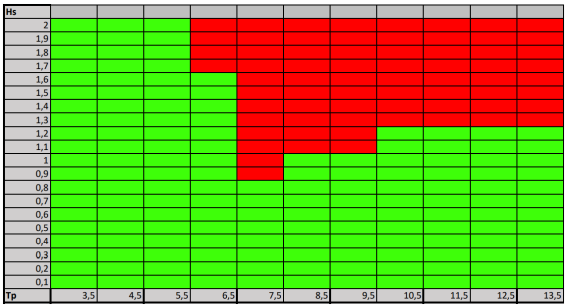

Figure 7.25: Vertical ladder motion operability limit for CS configuration.

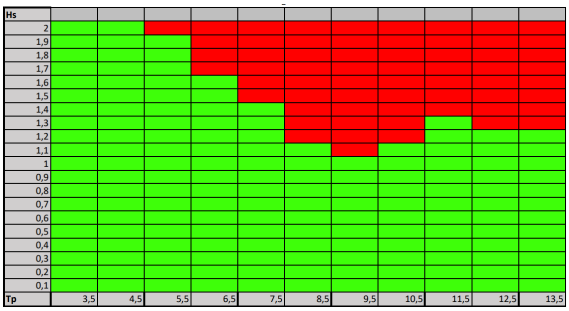

Figure 7.26: Vertical ladder motion operability limit for 0% FS configuration.

From the operability results it can be seen that the critical wave period shifts from 7.5 s for CS to 9.5 s for the 0% FS configuration. This corresponds to the decrease in natural frequency seen in both the heave and pitch RAOs of the CSD. This could indicate that, although the change in ladder angle across different spud keeper configurations is mostly negligible, the actual vertical motion response of the cutter head is more directly linked to the heave and pitch motion response of the pontoon.

7.2.5. Swing wire tension

The tensions in the swing wires are analysed for a CSD in operating conditions, but without any swing motion and a swing angle of ϕ_s = 0°. Due to the way winches and swing wires are designed in practice, they tend to have the same limiting force. It is therefore assumed that wire failure and winch failure share the same operational limit. The anchors are placed slightly behind the cutter head in x-direction, as stated in Appendix A, Table A.5, resulting in swing wire angles of Φ_{PS} = Φ_{SB} = 66.7°, where PS and SB denote portside and starboard respectively. The tension in the swing wire and its components in 3D for a JONSWAP beam wave record with H_s = 0.5 m and T_p = 8 s are shown in Fig. 7.27, for swing wires with a pretension of T_0 = 100 kN.

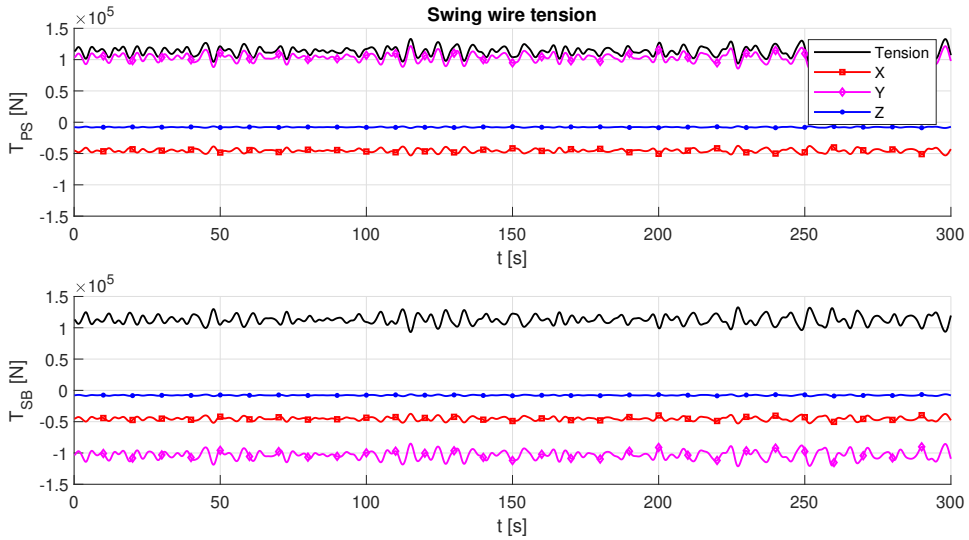

Figure 7.27: Swing wire tension of CS with H_s = 0.5 m and T_p = 8 s.

From Fig. 7.27 it can be seen that the main tension component is found in the y-direction, making up the majority of the overall tension T. The minimum and maximum tensions found in Fig. 7.27 are shown in Table 7.4. Negative tensions denote a force in the opposite direction.

	Tension		X		Y		Z	
	Min	Max	Min	Max	Min	Max	Min	Max
T_{PS} [kN]	93.8	133.1	-37.7	-53.0	85.7	121.7	-6.4	-9.3
T_{SB} [kN]	93.2	132.6	-37.4	-52.9	-85.1	-121.3	-6.2	-9.4

Table 7.4: Minimum and maximum swing wire tensions in CS.

From these results it can be seen that the tension amplitude in the swing wires is 40 kN. The majority of this increased tension is in the y-direction, which would increase if the distance between the anchor and the attachment of the swing wire to the ladder in x-direction is reduced. The vertical tension amplitude is fairly low, indicating that the swing wire influence on the pitch motion is very limited.

As the tension difference between PS and SB is negligible in the chosen model set-up, the comparison study of the swing wire tension for different spud keeper configurations will only include the PS swing wire. Fig. 7.28 shows this comparison for FS configurations compared to the CS connection.

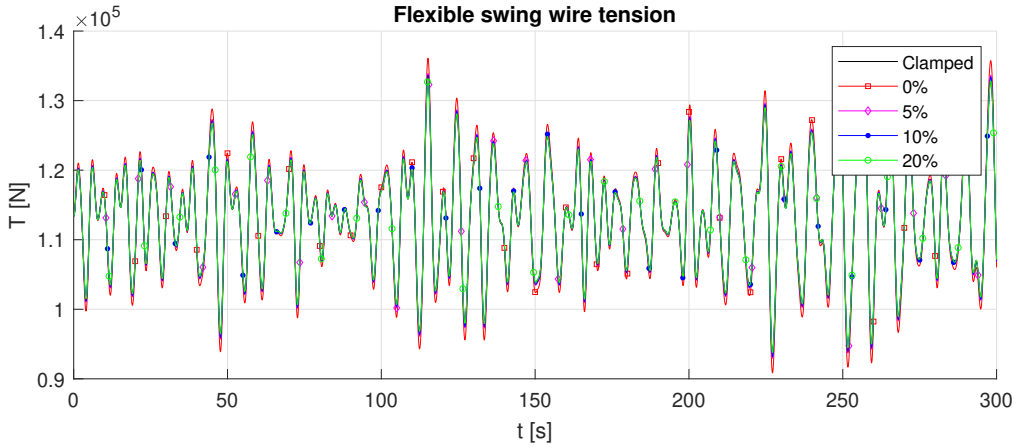

Figure 7.28: Swing wire tension comparison, for H_s = 0.5 m and T_p = 8 s.

From Fig. 7.28 it can be seen that the increased flexibility only slightly increases the tension in the swing wires when the connection becomes completely flexible. Any connection that still introduces some level of stiffness only has a negligible increase in tension. This relative difference with the CS connection is shown in Table 7.5.

	Tension [kN]		Difference [%]	
	Min	Max	Min	Max
CS	93.8	133.1	-	-
0%	97.5	136.6	3.9	2.6
5%	95.1	134.4	1.4	1.0
10%	94.7	134.0	1.0	0.7
20%	93.8	133.1	0	0

Table 7.5: Difference in swing wire tension between FS configurations.

Table 7.5 indicates only a minimal increase in swing wire tension in all configurations compared to the CS connection, with an increase of the maximum tension of the swing wire of 2.6% when the pontoon is completely free to move in pitch and roll around the spud. When the spud stiffness is increased, this increased tension quickly approaches the clamped configuration, with no discernible difference in tension when the stiffness exceeds 20% of the original stiffness.

This portside swing wire tension was simulated for a number of standard sea states to investigate the effect the added flexibility has on the operability of the CSD. Fig. **??** and 7.30 show the resulting operability scatter tables for a CS and a 0% FS configuration. It can be seen that very extreme sea-states are necessary to approach the operational limit for either configuration. The overall operability results in an uptime of 82.3% in CS and 79.1% in 0% FS. The largest difference is seen at high frequencies, with a reduction of operability from 1.7 m significant wave height to 1.5 m for waves of 3.5 s peak wave period. Secondly, a minimal decrease in operability is seen in for waves longer than 11.5 s.

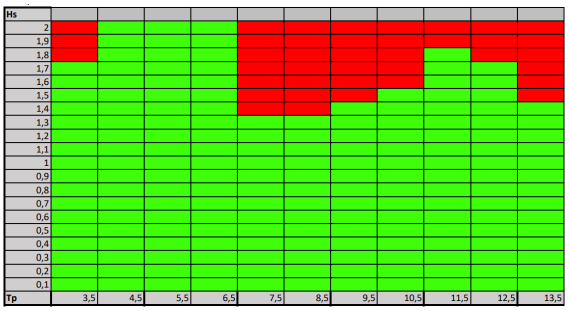

Figure 7.29: Swing wire tension operability limit for CS configuration.

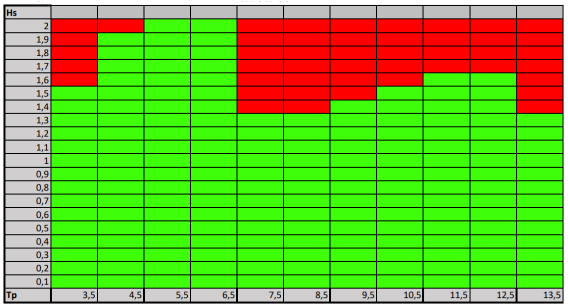

Figure 7.30: Swing wire tension operability limit for 0% FS configuration..

7.3. Operability analysis

The previous sections have been used as a means to verify the quality of the data and to show any anomalies found in the time series of a specific operability limit simulation. The complete operability analyses were performed using a large number of these simulations. In the JONSWAP spectra used, the period T_p is varied between 3.5 s and 13.5 s and the significant wave height H_s is varied between 0.1 m and 2 m. In this section the resulting operability scatter diagrams are presented, which are the sum of the four operability limits analysed in this chapter. It was found that the response of any flexible connection with a stiffness of 20% of the CS stiffness or higher only presented negligible difference with the CS results, therefore these are not presented here. Fig. 7.31 - 7.34 show the combined operability analysis for those connections for all the limits discussed previously, in head seas. Once again, it is important to

note that operability limits have been estimated from existing data, but are highly specific for any CSD. These results are meant to showcase the relative difference between the models and should not be used to infer any real-world operability windows.

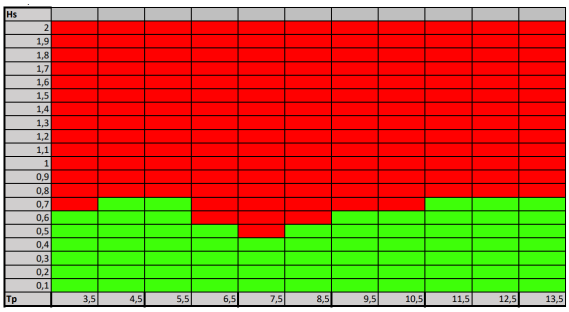

Figure 7.31: Complete operability analysis for CS configuration.

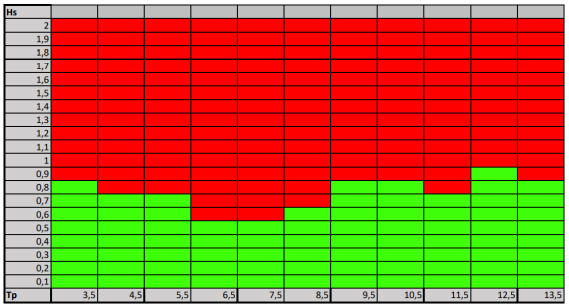

Figure 7.32: Complete operability analysis for 0% FS configuration.

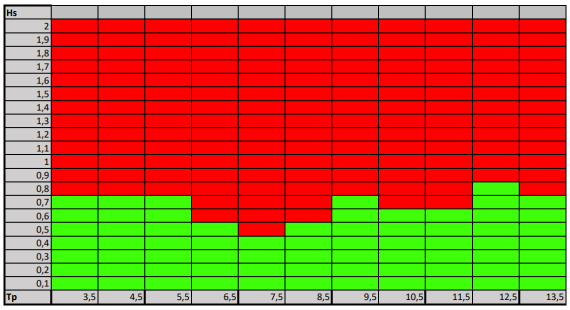

Figure 7.33: Complete operability analysis for 5% FS configuration.

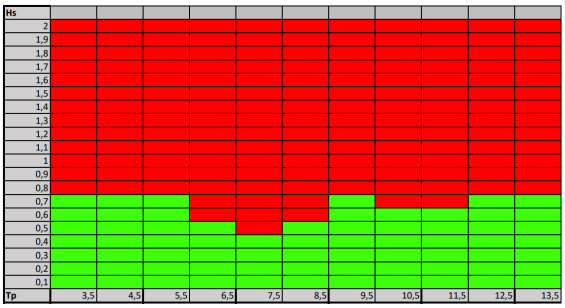

Figure 7.34: Complete operability analysis for 10% FS configuration.

For each configuration, the following results stand out (overall operability as a percentage in brackets):

- **Clamped spud (30.4%).** Across all wave periods, the operability of the CS configuration is completely governed by the spud bending stress limit. The best correlation from the FD to the TD results can be inferred from its pitch motion RAO, where the resonant frequency coincides with the wave period where the largest bending stress occurs.
- **FS 0% (35.5%).** This connection presents a significant improvement in operability. The spud bending stress when a CSD is free to move in pitch and roll is still a significant limit when the wave period matches the resonant peaks seen in the surge and pitch motion RAOs. The acceleration however plays a much larger role, matching the operability window of the bending stress in most cases.
- **FS 5% (31.4%).** The 5% FS connection has a large overlap with the CS configuration, and as such is also completely limited in operation by the spud bending stress. It presents a small difference in the operability window around T_p = 10.5 s, where its operability is shifted for a higher wave period than the CS connection.
- **FS 10% (30.9%).** Doubling the stiffness compared to 5% FS moves the operability closer to the CS connection, resulting in only a 0.5% improvement.
- **FS 20% (30.4%).** 20% stiffness of the original spud stiffness seems to be the limit for any significant difference in the motion and stress response on the spud. Any operability differences were negligible, and the reduction in spud bending stress was too slight to alter the operability window in any form.

The cable tension showed very little influence on the operability in head seas, as the y-component of the tension largely determines the overall tension. It would however need to be considered when the swing angle increases. Future research which include this swing motion should take care not to neglect the swing wire tension as an operational limit. The cutter head movement was shown to have a resonant motion peak in high-frequency waves. However, due to the depth at which most of the cutter ladder resides during operation, the actual fluid motion surrounding the ladder is limited, as was shown in Ch. 2. Because the cutter is very sensitive to changes in the cutting depth, it should be determined if the chosen limit if sufficient and what amount of lift of the cutter head can be deemed allowable.

7.3.1. Force-limited spud keeper

The force-limited spud connection will assume that the added flexibility is within the operational limits, thereby creating a best-case scenario where the spud bending stress is no longer a factor. From the previous analyses presented above, it can be seen that pitch acceleration becomes the sole limit governing the operability. This would present a operability scatter as shown in Fig. 7.35.

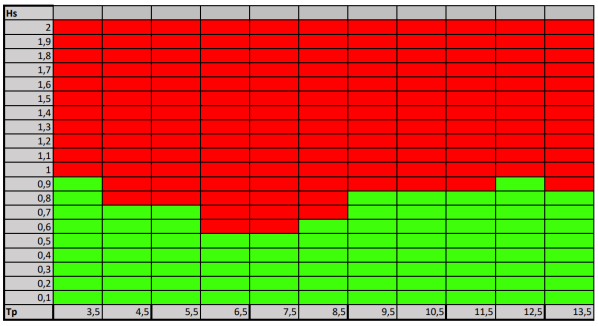

Figure 7.35: Complete operability analysis for a force-limited spud connection in head seas.

In this case, the total operability percentage would become 36.4%. This is an improvement over the 0% FS connection, but it would come with questions of feasibility.

8

Conclusion

Dredging vessels, and cutter suction dredgers (CSDs) in particular, have always been limited in their operability by their response to waves. Predicting this response is therefore crucial in preventing damage to critical operational and mooring components. With the increase in offshore projects in years to come, a model is required which accurately simulates real-world dredging operations. This thesis aims to expand upon previous models of CSD hydrodynamics in coastal conditions and use the newfound model to compare the operability of different CSD designs which use a level of flexibility in its spud mooring using the diffraction software ANSYS AQWA (AQWA). As prerequisites to the main research question, three objectives were considered that should be reached before the model could be used. These objectives are:

1. Building and verifying a model of wave forces, including non-linear wave phenomena and shallow water effects.
2. Modelling and verifying the boundary conditions such as the spud-soil interaction, representation of the swing wire forces and reaction forces related to the cutter in operation.
3. Modelling kinematics of the CSD-spud system as a multibody system, where the cutter ladder can move independently of the pontoon. The response of the system should be described in the time domain to account for shallow water non-linearities. Using this model, different flexible spud keeper configurations are analysed for their impact on CSD motions, spud stress and deflections and their overall effect on the operability of a CSD.

A hypothesis was proposed that older models could be improved in accuracy in three core areas: the presence of non-linearities in shallow water waves, the mooring effects of the spud and the cutter ladder, and the modelling of the cutter ladder as a separate body from the remaining CSD. This chapter will provide conclusions based on these three objectives.

8.1. Non-linear waves

Previous research has made assumptions about waves which were found to be inaccurate for shallow water waves in real-world conditions [86]. Regular, linear waves were shown to contain less wave energy than higher-order theories and possess a radically different wave shape than actual coastal waves. Modelling a CSD's motions using linear wave theory (LWT) would therefore underestimate the motions and forces endured during actual shallow water operation. A number of wave theories were discussed in terms of their applicability to the working area of a CSD. From this comparison, Stokes 2nd order wave theory (S2) was found to have the best agreement with real coastal waves. As S2 adds a non-linear steepness term

to a sinusoidal wave shape, FD modelling could no longer be used. The resulting CSD model in AQWA was tested to find the difference in its actual response between LWT and S2 in motions, wave forces and spud bending stress. It was shown that the overall wave height increased by 1.01% for S2, but an increased spud bending stress of 4.20% for waves at a water depth of 5 m. This indicates that the difference is significant and that the wave shape does impact the hydrodynamic response more than a simple increase in wave height of a linear wave would have done. This effect will become even more pronounced at smaller water depths, as this naturally increases the added steepness term. It can therefore be concluded that LWT does not accurately describe the hydrodynamic response of a CSD in shallow water and non-linearities and shallow water effects have to be taken into account.

8.2. Soil interaction

It is hypothesised that the current reliance on clamped spuds within CSD modelling does not give an accurate representation of real-world spud motion. A new model is proposed for wide and shallow spuds, replacing the clamped connection with a rotational spring to approximate soil reaction forces. It showed the tendency of a spud for rigid motion below the mudline, however these motions are very small compared to the resulting bending stress in the spud. It can therefore be concluded that, if this model is to be used in the future, it is better suited as an investigation into the upper limit of the soil reaction force. The complexity of the model means it cannot be simply implemented alongside the physical model in AQWA, and it does not offer a large enough benefit to the overall analysis. If this model is to be altered in the future it would require additional testing which can better describe the spring element in different soil types, and should be preferably be verified with real spud motion data during operation. For the purpose of the hydrodynamic analysis of the CSD it can therefore be argued that a clamped support suffices.

Next, mooring effects of the cutter ladder and operational forces of the cutter are often neglected in other studies on the motions of a CSD in waves, even though there is evidence that these can assist in the prevention of unwanted pitch motions [78]. To account for these effects, the connection of the cutter in the soil is modelled using spring elements. The effect of this spring can clearly be seen in the TD results of the cutter head movement, where the motion is clearly damped when the cutter head is pushed into the breach. This suggests a positive influence of the cutter head on the overall motion of the CSD. It should be noted that the the next improvement to the model would be to include the swing motion, which can give an indication of the production variation when the CSD moves in waves. The spring model would need to be expanded to include the cutting action of the cutter in both vertical and horizontal direction.

8.3. Modelling

For the overall model in AQWA, a number of conclusions can be made. Firstly, it is shown that the ladder and the pontoon have vastly different motion RAOs and should therefore be considered separate bodies. This is also visible in the TD model, which showed different motion responses for the ladder and the pontoon when the flexibility in the spud connection is changed. Therefore, accurate hydrodynamic analysis of a CSD cannot be done using a single-body model. Secondly, it is shown that potential theory is only accurate for large structures if external viscous damping is considered. Comparisons with the experimental data from the model tests by Brown [7] verifies this claim. As this damping coefficient is almost exclusively dependent on the geometry of the CSD, the numbers in this project cannot be copied for models of different CSDs and should be determined separately. Lastly, the added mass coef-

ficient is depth-dependent, which emphasises the need for specific shallow water modelling. The variation in motion RAOs for different water depths highlight that motion responses have to be considered for every viable operational water depth.

The analysis of the flexibility in the spud connection was done using a clamped model (CS), a fully flexible model (FS) and a number of partially flexible models which still retained a percentage of the original spud stiffness in rotation. FD modelling of these configurations showed a clear shift in the resonance peak of the motion response toward lower frequencies for more flexible connections. Furthermore flexible configurations have a larger overall motion response for low wave frequencies, but interestingly show a lower response for high frequencies. From this it can be concluded that changing the spud keeper design to include this flexibility can be beneficial if the new resonance occurs outside of the wave frequencies present in the working area. This would result in smaller pitch motion and thereby smaller stresses on the spud or other critical mooring elements.

8.4. Operability

Using the information and conclusions presented above, the main research question can be answered, which reads:

"How can different flexible spud keeper configurations be modeled and incorporated into a dynamic multibody model of a CSD in coastal conditions, and what are the effects on its hydrodynamic response?"

The modelling part of the question has been answered in the above sections, but to provide a clear means of comparison between the configurations, an operability analysis was performed based on spud bending stress, absolute motion and acceleration of the pontoon, cutter head movement, and swing wire tension. Analysis of the current CS configuration indicated that spud bending stress is the main governing operational limit, with an overall operability of 30.4% within the given wave parameters. Purely on spud bending stress, the FS configuration would increase the operability to 40.4%. FS did however present a large decrease in operability due to the maximum allowable pitch acceleration of the pontoon, bringing its overall operability down to 35.5%, or an increase in operability of 16.4% compared to CS. FS connections which still held a level of stiffness only provided small improvements for very specific wave parameters, but overall can be considered insignificant and are unlikely to provide a significant benefit to real offshore dredging operation.

To answer the research question, this thesis provided concrete evidence that flexible spud keeper configurations can expand the operability window of a CSD, mainly through the decrease in overall spud bending stress. They would incur increased motions and accelerations and alter the motion of the pontoon and the cutter ladder towards lower wave frequencies. It was shown that shallow coastal conditions require a more intricate modelling approach when it comes to wave theory and that there are major effects on the hydrodynamic coefficients when the CSD approaches the seabed. It is however important to note that a number of assumptions could not be verified within this model, and that future research is needed to allow for the modelling of the CSD swing motion, verification of the spud model and a full analysis of the cutter forces during operation.

9

Further research

Over the course of creating the model and its use, a number of assumptions were made which require further verification. This chapter will introduce a number of examples of further research which should be performed to confirm these assumptions and statements and improve the model before it can be used practically.

9.1. Boundary conditions

The Wang model for wide shallow spuds shows promise when it comes to accurately representing a spud's motion below the mudline. However, due to the lack of data surrounding the equivalent stiffness for different types of soils, it becomes very complex to implement in early hydrodynamic analysis of any new CSD design. Secondly, the model becomes almost impossible to use when a soil is highly inconsistent, for example because of the presence of rocks which alter the stiffness and likely the penetration depth. Two additional experiments could be performed to increase its usability. First, research into the motion of a spud during CSD operation can be done for different soil types, similarly to the research done by Sitanggang which is used in this thesis [68]. Expanding the approach to allow for complete soil failure around the spud can confirm the spud tip force upper limit suggested in this thesis, and thereby confirm the shape of the rotational stiffness of the spring presented by Wang. Secondly, because the Wang model is solely based on FEM data, real-world experiments which confirm the placement and stiffness of the spring itself are desirable. This can be used to confirm the assumptions made, including the plastic deformation of the soil at the spud tip and the differences in stiffness for varying soil shear moduli. Either of these experiments could verify the conclusion made that soil failure around the spud is not a critical component of operability.

Including the operational forces as a combination of fixed forces and spring elements is already step towards increased accuracy in the modelling of all the forces a CSD endures during operation, but the accuracy is difficult to verify. Cutter force functions based on the depth of the cut and the soil properties have been proposed in the past and should be the next step to be implemented. It is unclear if this would be possible in AQWA considering its limited functionalities when it comes to soil interaction. Therefore, a comparison study is be proposed between the simplified approach taken in this thesis and more extensive cutter force functions. This can provide better insight in the actual forces encountered, and could be used to find a characteristic value the operational force could take depending on the operational conditions in the working area. For practical use of the model, it would be desirable to implement such a cutter force function into the hydrodynamic motion model, which would allow for results to not

just include motion and reaction forces, but also the effects of changes in the design of the CSD on the production.

9.2. Modelling

The choice to limit the water depth to a minimum of 5 m was made using very conservative estimates for a minimum dredging depth. Practical knowledge of dredging shows that it is possible to dredge at smaller water depths. When looking at the applicability of shallow water wave theories, it can be argued that a point might be reached where Cnoidal theory becomes dominant over S2. It was also shown that most hydrodynamic coefficients are very sensitive to depth changes, and would thus alter the motion behaviour of the CSD. A number of assumptions made regarding the dynamics of the CSD could be verified from model experiments, which would be the next logical step following this thesis. From the motions found in model experiments the hydrodynamic coefficients can be confirmed, including the depth effects seen in the added mass coefficients and confirming the viscous damping approach specifically for a CSD and not just rectangular barges. The resulting RAOs can confirm the shift towards lower frequencies seen in the comparison RAOs for different water depths. Adding flexibility can then be used to confirm the model data presented in this thesis.

AQWA has the capability to include set motions in a TD model. This means the swing motion could be modelled directly instead of making use of added resistance to include operational forces. During the swing motion the CSD encounters a larger range of wave angles of attack than have been considered in this thesis, which could further expand upon which heading is most optimal for dredging in waves. The inclusion if this feature would however heavily rely on the method with which the cutter force function is implemented.

Bibliography

[1] G. B. Airy. *Tides and waves*. B. Fellowes, 1845.

[2] D. Amar Bouzid. “Numerical investigation of large-diameter monopiles in sands: Critical review and evaluation of both API and newly proposed py curves”. In: *International Journal of Geomechanics* 18.11 (2018), pp. 401–432.

[3] S. Bai et al. “Data mining approach to construction productivity prediction for cutter suction dredgers”. In: *Automation in Construction* 105 (2019), pp. 102–148.

[4] E. van der Blom et al. “Development of dredge equipment is no longer driven by economy only”. In: *Proceedings, WEDA XXXI Technical Conference & TAMU 42 Dredging Seminar*.

[5] J. Boussinesq. *Essai sur la théorie des eaux courantes*. Vol. 2. Imprimerie nationale, 1877.

[6] C. L. Bretschneider. *Wave variability and wave spectra for wind-generated gravity waves*. 118. The Board, 1959.

[7] D. T. Brown, R. E. Taylor, and M. H. Patel. “Barge motions in random seas–a comparison of theory and experiment”. In: *Journal of Fluid Mechanics* 129 (1983), pp. 385–407.

[8] D. E. Cartwright and M. S. Longuet-Higgins. “The statistical distribution of the maxima of a random function”. In: *Proceedings of the royal society of London. Mathematical and Physical Sciences* 237.1209 (1956), pp. 212–232.

[9] S. K. Chakrabarti. “Empirical calculation of roll damping for ships and barges”. In: *Ocean Engineering* 28.7 (2001), pp. 915–932.

[10] S. K. Chakrabarti. *Hydrodynamics of offshore structures*. WIT press, 1987.

[11] Y. W. Choo and D. Kim. “Experimental development of the p-y relationship for large-diameter offshore monopiles in sands: Centrifuge tests”. In: *Journal of Geo-technical and Geo-environmental Engineering* 142.1 (2016), pp. 40–58.

[12] G. Clauss et al. “Water depth influence on wave–structure-interaction”. In: *Ocean engineering* 36.17-18 (2009), pp. 1396–1403.

[13] J. P. Coelingh, A. J. M. Van Wijk, and A. A. M. Holtslag. “Analysis of wind speed observations on the North Sea coast”. In: *Journal of Wind Engineering and Industrial Aerodynamics* 73.2 (1998), pp. 125–144.

[14] J. I. Collins. “Probabilities of breaking wave characteristics”. In: *Coastal Engineering 1970*. 1970, pp. 399–414.

[15] W. E. Cummins. *The impulse response function and ship motions*. Tech. rep. David Taylor Model Basin Washington DC, 1962.

[16] Damen Shipyards - Damen Dredging Equipment. *Cutter Suction Dredger CSD650 Product Sheet*. URL: `https://products.damen.com/~/media/Products/Images/Clusters%5C%20groups/Dredging/CSD/CSD%5C%20650/Documents/Damen_Cutter_Suction_Dredger_650.ashx`.

[17] R. G. Dean. “Stream function representation of nonlinear ocean waves”. In: *Journal of Geophysical Research* 70.18 (1965), pp. 4561–4572.

[18] Det Norske Veritas DNV. “Fatigue design of offshore steel structures”. In: *Rev. 3* (2011).

[19] G. Dong et al. “Energy properties of regular water waves over horizontal bottom with increasing nonlinearity”. In: *Ocean Engineering* 218 (2020), pp. 108–159.

[20] D. Doong, B. Lee, and C. C. Kao. “Wave measurements using GPS velocity signals”. In: *Sensors* 11.1 (2011), pp. 1043–1058.

[21] S. X. Du et al. “The occurrence of irregular frequencies in forward speed ship seakeeping numerical calculations”. In: *Ocean engineering* 38.1 (2011), pp. 235–247.

[22] ECS. “Eurocode 7: geotechnical design–Part 1: general rules”. In: *European Committee for Standardization. The authority of the Standards Policy and Strategy Committee* (2004).

[23] J. D. Fenton. “Nonlinear wave theories”. In: *the Sea* 9.1 (1990), pp. 3–25.

[24] C. Gaudin, F. Schnaid, and J. Garnier. “Sand characterization by combined centrifuge and laboratory tests”. In: *International Journal of Physical Modelling in Geotechnics* 5.1 (2005), pp. 42–56.

[25] Y. Goda, T. Takayama, and Y. Suzuki. “Diffraction diagrams for directional random waves”. In: *Coastal Engineering 1978*. 1978, pp. 628–650.

[26] S. D. A. Hannot et al. “A validated tool for evaluating the design and predicting the workability of dredgers”. In: *Proceedings WODCON XX-Congress and Exhibition: The Art of Dredging*. 2013.

[27] K. Hasselmann. “Feynman diagrams and interaction rules of wave-wave scattering processes”. In: *Reviews of Geophysics* 4.1 (1966), pp. 1–32.

[28] K. Hasselmann et al. “Measurements of wind-wave growth and swell decay during the Joint North Sea Wave Project (JONSWAP).” In: *Ergaenzungsheft zur Deutschen Hydrographischen Zeitschrift, Reihe A* (1973).

[29] N. Hogben. “Global wave statistics”. In: *British Maritime Technology* (1986).

[30] L. H. Holthuijsen. *Waves in oceanic and coastal waters*. Cambridge university press, 2010.

[31] Y. Ikeda, T. Fujiwara, and T. Katayama. “Roll damping of a sharp-cornered barge and roll control by a new-type stabilizer”. In: *The Third International Offshore and Polar Engineering Conference*. OnePetro. 1993.

[32] Ansys Inc. “AQWA theory manual”. In: *ed. Canonsburg, PA 15317, USA* (2013).

[33] Rocscience Inc. “ROCScience: RSPile Laterally Loaded Piles”. In: (2022). URL: `https://static.rocscience.cloud/assets/verification-and-theory/RSPile/RSPile-Laterally-Loaded-Pile-Theory.pdf`.

[34] A. Jafari, B. Asgarian, and M. Daghigh. “Effect of Foundation Modeling on Extreme Response of Offshore Jack-up Unit”. In: *International Conference on Offshore Mechanics and Arctic Engineering*. Vol. 49095. 2010, pp. 475–481.

[35] P. Jeanjean et al. “The new API recommended practice for geotechnical engineering: RP 2GEO”. In: *2nd International Symposium on Frontiers in Offshore Geotechnics, ISFOG 2010*. CRC Press. 2011, pp. 903–908.

[36] J. M. J. Journee. “Theoretical manual of SEAWAY”. In: *Delft University of Technology Shiphydromechanics Laboratory,(Release 4.19, 12-02-2001)* (2001).

[37] J. Journeé and W. Massie. *Offshore Hydromechanics*. Delft University of Technology, 2001.

[38] H. Kato. “Effects of bilge keels on the rolling of ships”. In: *Journal of Zosen Kiokai* 1965.117 (1965), pp. 93–101.

[39] G. H. Keulegan, L. H. Carpenter, et al. “Forces on cylinders and plates in an oscillating fluid”. In: *Journal of research of the National Bureau of Standards* 60.5 (1958), pp. 423–440.

[40] P. J. Keuning and J. M. Journee. “Calculation method for the behaviour of a cutter suction dredge operating in irregular waves”. In: (1983).

[41] R. T. Klinkvort and O. Hededal. “Effect of load eccentricity and stress level on monopile support for offshore wind turbines”. In: *Canadian Geotechnical Journal* 51.9 (2014), pp. 966–974.

[42] D. J. Korteweg and G. De Vries. “XLI. On the change of form of long waves advancing in a rectangular canal, and on a new type of long stationary waves”. In: *The London, Edinburgh, and Dublin Philosophical Magazine and Journal of Science* 39.240 (1895), pp. 422–443.

[43] H. E. Krogstad and Ø. A. Arntsen. “Linear wave theory”. In: *Norwegian University of Science and Technology* (2000).

[44] B. Le Mehaute, D. Divoky, and A. Lin. “Shallow water waves a comparison of theories and experiments”. In: *Coastal Engineering 1968*. 1969, pp. 86–107.

[45] S. Levitus. *National Oceanographic Data Center inventory of physical oceanographic profiles: global distributions by year for all countries*. 18. US Department of Commerce, National Oceanic and Atmospheric Administration, 1992.

[46] B. Loos. “Operability limits based on vessel motions for submarine power cable installation”. MSc Thesis. Mekelweg, Delft: TU Delft.

[47] G. G. Meyerhof. “Some recent research on the bearing capacity of foundations”. In: *Canadian geotechnical journal* 1.1 (1963), pp. 16–26.

[48] G. G. Meyerhof, V. V. R. N. Sastry, and A. S. Yalcin. “Lateral resistance and deflection of flexible piles”. In: *Canadian Geotechnical Journal* 25.3 (1988), pp. 511–522.

[49] S. A. Miedema. “Mathematische modelvorming tav een snijkopzuiger in zeegang”. In: *TH Delft* (1984).

[50] S. A. Miedema. “The modelling of the swing winches of a cutter dredge in relation with simulators”. In: *Texas A/M 32nd Annual Dredging Seminar*. 2000.

[51] S. A. Miedema, J. M. J. Journee, and S. T. Schuurmans. *On the Motions of a Seagoing Cutter Dredge: A Study in Continuity*. Delft University of Technology, Ship Hydromechanics Laboratory, 1992.

[52] J. R. Morison et al. “The forces exerted by surfaces waves on piles”. In: *Petroleum trans* (1950).

[53] Ministerie van Infrastructuur en Waterstaat - Netherlands. *Stromingskaart Nederland*. URL: `https://waterinfo.rws.nl/#!/kaart/stroming/`.

[54] Ministerie van Infrastructuur en Waterstaat - Netherlands. *Windkaart Nederland*. URL: `https://waterinfo.rws.nl/#!/kaart/wind/`.

[55] I. R. Nielsen. “Assessment of ship performance in a seaway”. In: *Publisher: NORDFORSK, Sortedam Dossering 19, DK-200 Copenhagen, Denmark, ISBN: 87-982637-1-4* (1987).

[56] U. D. Nielsen and A. Ikonomakis. “Wave conditions encountered by ships — A report from a larger shipping company based on ERA5”. In: *Ocean Engineering* 237 (2021), pp. 109–148. ISSN: 0029-8018.

[57] Netherlands Wind Assosciation: NWEA. *Nederland start inhaalrace Offshore Wind*. Jan. 2022. URL: https://www.nwea.nl/nederland-start-inhaalrace-offshore-wind/.

[58] D. V. Okur and A. Ansal. “Stiffness degradation of natural fine grained soils during cyclic loading”. In: *Soil Dynamics and Earthquake Engineering* 27.9 (2007), pp. 843–854.

[59] D. W. Ostendorf and O. S. Madsen. “An analysis of longshore currents and associated sediment transport in the surf zone”. In: *Ralph M. Parsons Laboratory for Water Resources and Hydrodynamics* (1979).

[60] G. Petrasovits and A. Awad. “Ultimate lateral resistance of a rigid pile in cohesionless soil”. In: *Fifth Eur Conf On Soil Proc/Sp/*. Conf Paper. 1972.

[61] W. J. Pierson Jr and L. Moskowitz. “A proposed spectral form for fully developed wind seas based on the similarity theory of SA Kitaigorodskii”. In: *Journal of geophysical research* 69.24 (1964), pp. 5181–5190.

[62] W. J. Pierson Jr, G. Neumann, and R. W. James. *Practical methods for observing and forecasting ocean waves by means of wave spectra and statistics*. Tech. rep. Naval Oceanographic Office NSTL Stations MS, 1971.

[63] J. A. Pinkster and J. P. Hooft. “Low frequency second order wave forces on vessels moored at sea”. In: *11th Symposium on Naval Hydrodynamics, ONR, London, England, 1976*. 1976.

[64] W. G. Qi et al. “Scour effects on p–y curves for shallowly embedded piles in sand”. In: *Géotechnique* 66.8 (2016), pp. 648–660.

[65] M. Rahman. “Fundamentals concerning Stokes waves”. In: *WIT Transactions on Engineering Sciences* 9 (1970).

[66] W. J. M. Rankine. “II. On the stability of loose earth”. In: *Philosophical transactions of the Royal Society of London* 147 (1857), pp. 9–27.

[67] M. Shadlou and S. Bhattacharya. “Dynamic stiffness of monopiles supporting offshore wind turbine generators”. In: *Soil Dynamics and Earthquake Engineering* 88 (2016), pp. 15–32.

[68] A. P. B. Sitanggang. “A Geo-Centrifuge Experiment of Spud Pole Anchoring in Sand”. MSc Thesis. Delft: TU Delft, 2017.

[69] SNAME. “Nomenclature for treating the motion of a submerged body through a fluid”. In: *The Society of Naval Architects and Marine Engineers, Technical and Research Bulletin* 1950 (1950), pp. 1–5.

[70] R. M. Sorensen. “Two-dimensional wave equations and wave characteristics”. In: *Basic Coastal Engineering* (2006), pp. 9–52.

[71] M. St Denis and W. J. Pierson Jr. “On the motion of ships in confused seas, Soc”. In: *Nav. Architects Mar. Eng. Trans* 61 (1953), pp. 332–357.

[72] G. G. Stokes. “On the theory of oscillatory waves”. In: *Transactions of the Cambridge philosophical society* (1880).

[73] N. Subramanian. *Design of steel structures*. Oxford University Press, 2008.

[74] G. Van Oortmerssen. *The motions of a moored ship in waves*. Tech. rep. H. Veenman en Zonen nv, 1976.

[75] P. N. W. Verhoef. *Wear of rock cutting tools: implications for the site investigation of rock dredging projects*. Routledge, 2017.

[76] H. Vindenes et al. “Analysis of tidal currents in the North Sea from shipboard acoustic Doppler current profiler data”. In: *Continental Shelf Research* 162 (2018), pp. 1–12.

[77] W. J. Vlasblom. “College WB3413 Dredging Processes”. In: *The Breaching* (2003).

[78] W. J. Vlasblom. “Designing dredging equipment”. In: *Lecture notes, TU Delft* Vol. 5 (2003), p. 24.

[79] W. J. Vlasblom. “Relation between cutting-, sidewinch-, and axial forces for cutter suction dredgers”. In: *Proceedings 15th world dredging congress, Las Vegas, Nevada, USA, June 28-July 2, 1998: dredging into the 21st century & Exhibition: vol. 1*. WEDA. 1998, pp. 275–291.

[80] J. H. Vugts. *Handbook of Bottom Founded Offshore Structures: Part 1. General features of offshore structures and theoretical background*. Vol. 1. Eburon Uitgeverij BV, 2013.

[81] H. Wang et al. “A simple approach for predicting the ultimate lateral capacity of a rigid pile in sand”. In: *Géotechnique Letters* 10.3 (2020), pp. 429–435.

[82] H. Wang et al. “A simple rotational spring model for laterally loaded rigid piles in sand”. In: *Marine Structures* 84 (2022), pp. 103–225.

[83] P. Wellens. “MT44020 Motions and Loading of Structures in Waves, Course Notes”. In: *TU Delft* (2021).

[84] J. E. W. Wichers. “On the forces on a cutter suction dredger in waves”. In: *Proc. WODCON IX, Vancouver, BC, Canada* (1980).

[85] J. E. W. Wichers and E. J. Claessens. “Prediction Downtime of Dredges Operating in the open sea”. In: *WEDA, Rhode Island* (2000).

[86] R. L. Wiegel. “A presentation of cnoidal wave theory for practical application”. In: *Journal of Fluid Mechanics* 7.2 (1960), pp. 273–286.

[87] L. Xiong et al. “Motion responses of a moored barge in shallow water”. In: *Ocean Engineering* 97 (2015), pp. 207–217.

[88] L. Zhang, F. Silva, and R. Grismala. “Ultimate lateral resistance to piles in cohesionless soils”. In: *Journal of Geotechnical and Geoenvironmental Engineering* 131.1 (2005), pp. 78–83.

Appendix A: CSD700 Geometry

This appendix will provide all the technical properties of the CSD700 designed by Damen used in the model. The CSD700 is part of Damen Dredging Equipment's CSD2.0 project, which aims to improve the current range in their dredging abilities, while at the same time aiming for a higher level of sustainability in operation and production. To reduce both the cost and difficulty of transport, the CSDs have reduced in overall size. Where the less powerful CSD650-25m of the old range had a total length in mooring position of 70 m, the CSD700 only measures 64 m while still able to dredge up to a maximum dredging depth of 25 m. This was done by moving the ladder hinge back, as can be seen in Fig. A.1 and A.2.

Tables A.1 - A.4 show the overall dimensions and dredging characteristics of the CSD700 that were used in the model. As this project was performed during the design phase of the CSD700, some parameters were still unknown or likely to change in the final design. Due to similarities with the size and power of the older range model CSD650-25m, any unknown parameters have been estimated from this model [16].

There are some crucial changes in the new model which affect its hydrodynamic response. First, the pontoon tapers on the aft-side. As this decreases the effective beam, it affects the natural roll period and roll damping of the overall vessel, as is shown in Section 4.3. Secondly, the hull is created out of one single pontoon known as a monohull. This eliminates shear stresses in the connection between multiple pontoons. Due to this design change these splitting forces were not taken into account for this project.

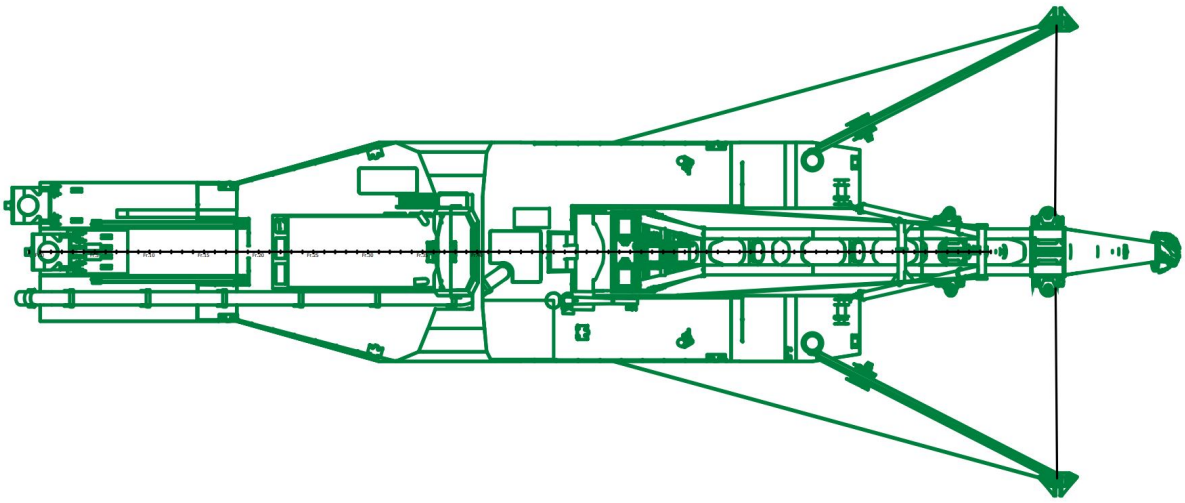

Figure A.1: Top view of the CSD700.

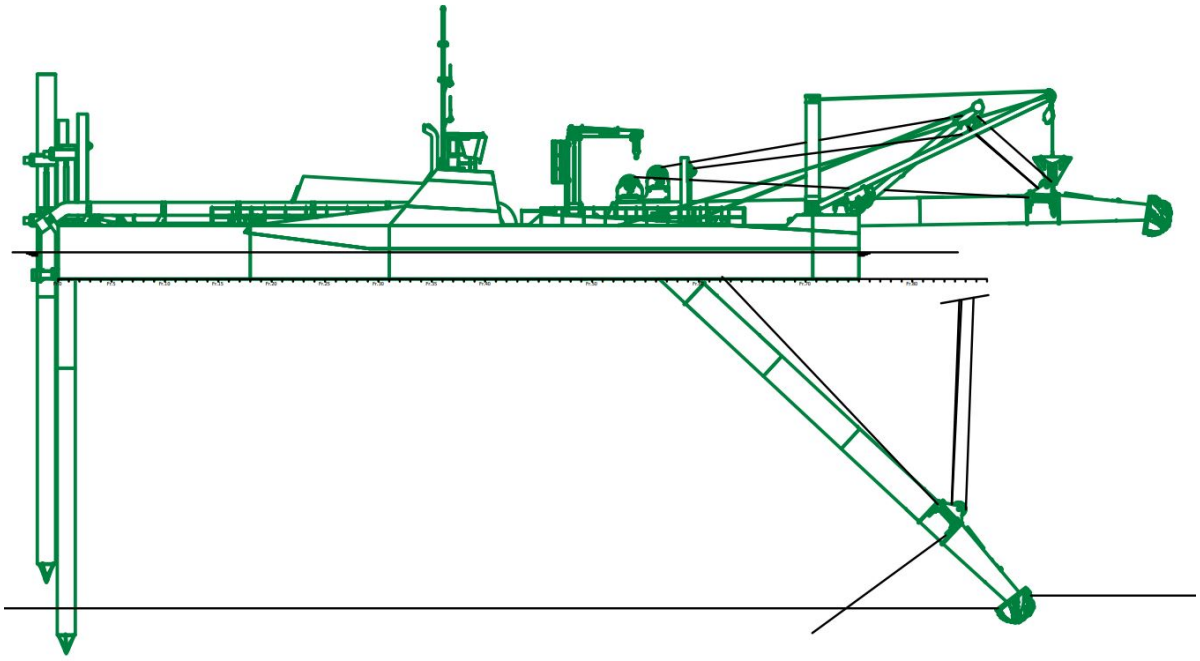

Figure A.2: Side view of the CSD700.

General	
Type	CSD700
Maximum dredging depth	25 m
Hull type	Monohull

Table A.1: General parameters of the CSD700 used in the model.

Dredging Features	
Swing width	70 m
Slurry capacity	7000 m^3/h
Suction/discharge pipe diameter	700 mm
Cutter type	Crown model

Table A.2: General dredging features of the CSD700 used in the model.

Dimensions	
Length including ladder	64 m
Length pontoon	45 m
Beam	12 m
Height pontoon	3 m
Draught	1.5 m
Width ladder	2.5 m
Spud length	30 m
Spud diameter	1014 mm
Cutter diameter	2100 mm
Spud hoisting stroke	3 m
Spud carriage step distance	6 m
Weight without spuds	735 tonnes

Table A.3: Principal dimensions of the CSD700 used in the model.

Power characteristics	
Cutter power	700 kW
Hoisting winch capacity	270 kN, 0-15 m/min
Side winch capacity	270 kN, 0-20 m/min

Table A.4: Power and engine characteristics of the CSD700 used in the model.

Interaction points	Coordinates		
	x [m]	y [m]	z [m]
Spud	0	0	0
Pontoon COG	22.2	0	0
Ladder COG	46.2	0	-0.75
Ladder hinge	30.3	0	-0.75
Spud-soil interaction	0	0	-5
SB wire connection	57.2	-1.5	-0.75
PS wire connection	57.2	1.5	-0.75
SB anchor	40	-40	-5
PS anchor	40	40	-5
Cutter-soil interaction	62	0	-5

Table A.5: Coordinates of the interaction points of the CSD700 at h = 5 m, θ_{ladder} = 0°.

A.0.1. Dredging depth

According to the rules of thumb for safe dredging operation by Vlasblom [78], dredging can take place if there is at least 1 m of clearance between the underside of the keel and the sea floor, as well as a minimum ladder angle of 5°. Fig. A.3 shows the distribution of the ladder angle with the still water line. It can be seen that a minimum dredging depth according to these rules would be 4 m, however practice teaches that this is a very conservative estimate. For the purpose of this project however this rule is obeyed.

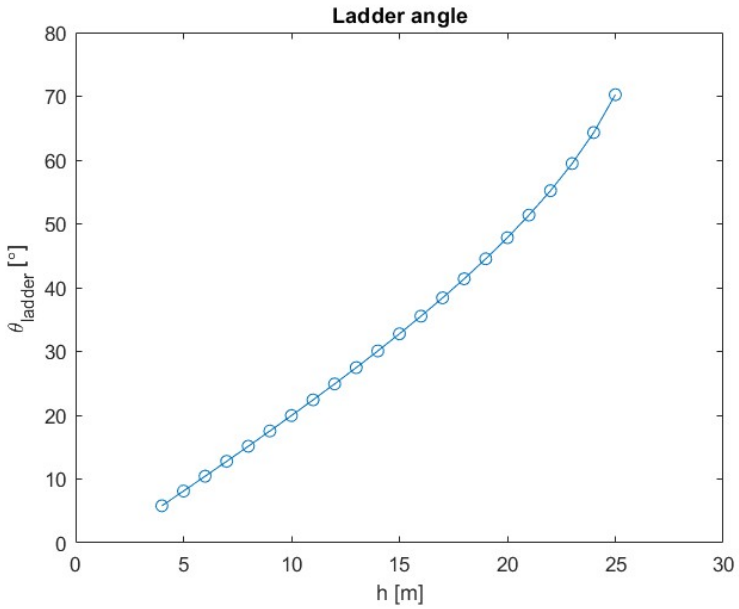

Figure A.3: Cutter ladder angle with the sea floor as a function of water depth.

B

Appendix B: Soil parameters

As soil mechanics are not the main topic of analysis in this thesis but only serve as a means to determine the mooring effect of the cutter ladder, they are not discussed in-depth in the main thesis. This appendix serves to expand upon the theory used to find the soil response to the spud force and the cutter interaction. First, specific soil parameters will be covered for the medium-dense sand mixture used in the spud and soil analysis in Chapter 3. Because the model builds on previous Damen and TU Delft research done by Sitanggang [68] on the behaviour of shallow spuds under cyclic loading, the soil was chosen to approximate the soil used in that analysis as close as possible, while remaining relevant for the operational conditions of the case study. Next, two approaches will be given to determine the rotational stiffness K_θ of the spud for different soil profiles. Finally, a brief analysis is given into the difference between undercutting and overcutting and their effect on the mooring of a CSD.

B.1. Soil data and additional equations

This section will provide the data used to determine the soil stiffness in Section 3.3 and introduce a number of equations to determine the loading condition of the spud below the mudline. The soil data for medium-dense sand is shown in Table B.1. Any properties not available in the thesis by Sitanggang are provided by Subramanian [73]:

Soil data		
Symbol	Description	Value
ρ	Density	$2.10 \cdot 10^3$ kg/m^3
E_s	Elasticity modulus	48-81 N/mm^2
k_s	Modulus of subgrade reaction	9600-80000 kN/m^3
v_s	Poisson's ratio	0.3
K_p	Coefficient of passive earth pressure	2.769
$P_{b,u}$	Allowable bearing pressure	250 kN/m^2
c_u	Apparent cohesion	15-30 kPa
$\phi^{'}$	Effective soil stress friction angle	28°
$\phi^{'}_a$	Angle of internal friction	21°
γ_s	Saturated unit weight	20.0 kN/m^3
$\gamma^{'}$	Effective unit weight	9.94 kN/m^3

Table B.1: Soil data for medium-dense sand [68, 73]

Additional equations pertaining to the interaction between the spud and the soil and the determination of the rotational spud stiffness K_θ found in Eqs 3.7 - 3.19:

- Shear modulus of a soil [68]:

$$G_s = \frac{E_s}{2(1+v_s)} \tag{B.1}$$

- Shaft friction factors [35]:

$$\alpha = \frac{\phi'}{2} = 14^\circ \tag{B.2}$$

$$\beta = 45^\circ + \frac{\phi'}{2} = 59^\circ \tag{B.3}$$

- Factor A to account for the loading condition [81]:

$$A = \begin{cases} 0.9 & \text{for cyclic loading} \\ 3 - 0.8 \cdot \frac{X}{D} & \text{for static loading} \end{cases} \tag{B.4}$$

- Coefficient of lateral earth pressure at rest [35]:

$$K_0 = 0.4 \tag{B.5}$$

B.2. K_θ for different soil profiles

This section will provide additional information regarding different small strain shear modulus G_0 distributions than presented in Section 3.3. The soil distribution and the profile of the shear modulus have been assumed to be constant in the model, however different soil types and other environmental conditions might prove this assumption to be wrong. Wang et al. provides two more equations that have a good representation with FEM results for a linearly increasing G_0 with the penetration depth of the spud, and one for a G_0 which varies with the square root of the depth. Especially the square root profile shows promise with practical applications of the rotational spring model in sand, but research on that topic is still inconclusive and should be verified with experimental testing. The initial rotational stiffness is found with:

$$K_{\theta\text{-initial}} = C_k D L^2 G_{0.75L} \tag{B.6}$$

Where C_k is a function of empirical constant a and b and depth and dimensions of the spud:

$$C_k = a \cdot \exp\left(b \times \frac{L}{D}\right) + c \cdot \exp\left(d \times \frac{L}{D}\right) \text{ for } 10 \geq \frac{L}{D} \geq 1 \tag{B.7}$$

For:

$a = 9.1,$	$b = -2.24,$	$c = 2.71,$	$d = 0.065$	for constant G_0 over the depth
$a = 6.5,$	$b = -1.5,$	$c = 1.4,$	$d = 0.044$	for a linearly increasing G_0 over the depth
$a = 6.2,$	$b = -1.62,$	$c = 1.85,$	$d = 0.053$	for a varying G_0 with the square root of the depth

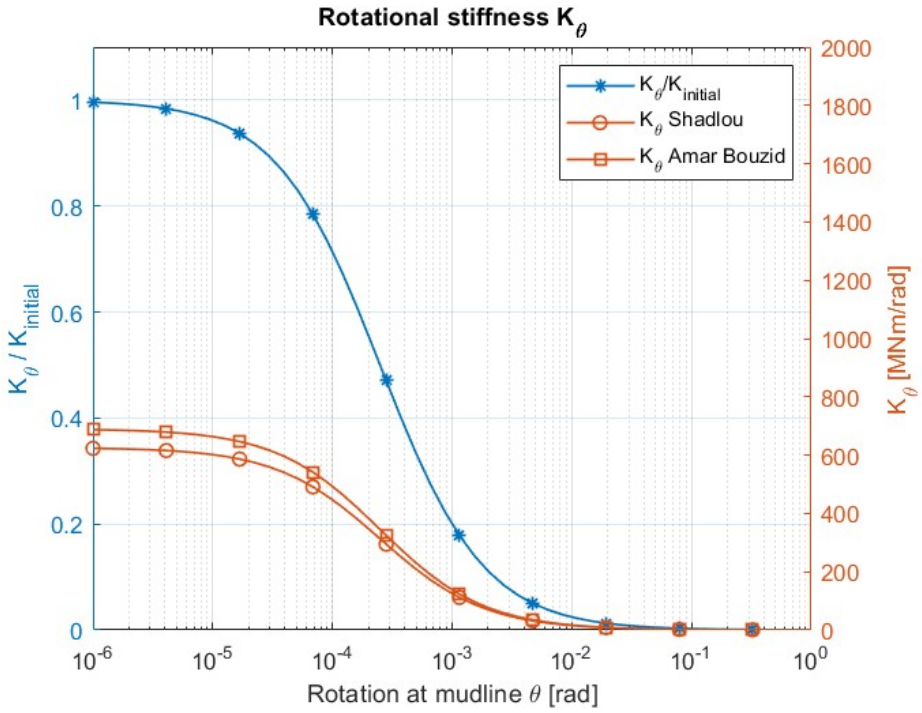

Figure B.1: Degradation of rotational stiffness for linear increasing G_0.

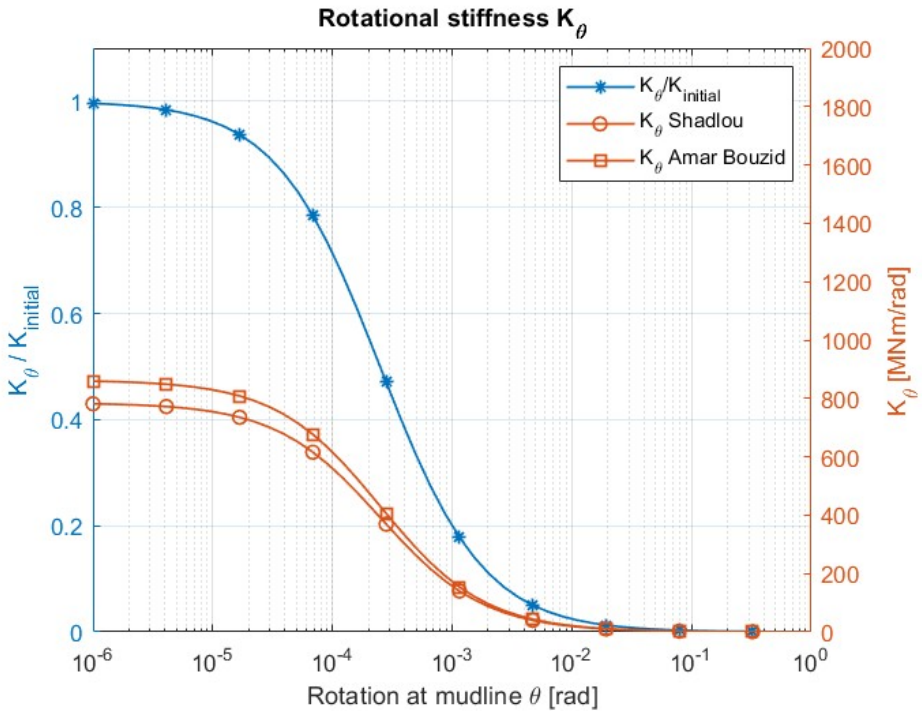

Figure B.2: Degradation of rotational stiffness for increasing G_0 with the square root of the depth.

Some additional approximations are presented by Amar Bouzid for the resulting rotational spring stiffness K_θ these soil profiles in Eq. B.8. Fig. B.1 and B.2 show the new K_θ distributions due to the new varying shear modulus.

$$\begin{aligned} K_{\theta\text{-initial}} &= 4DL^2G_{0.75L} && \text{for constant } G_0 \\ K_{\theta\text{-initial}} &= 2DL^2G_{0.75L} && \text{for linearly increasing } G_0 \\ K_{\theta\text{-initial}} &= 2.5DL^2G_{0.75L} && \text{for } G_0 \text{ increasing with the square root of the depth} \end{aligned} \tag{B.8}$$

Fig. B.1 and Fig. B.2 shows a large decrease in stiffness compared to a constant G_0. This could lead to an overestimation of the soil failure limit used in the model. Extra research and site-specific tests are necessary to find an accurate representation of the true G_0 distribution.

B.3. Cutter forces

The speed of the swing, the depth of the cut and specific properties of the soil are all crucial parts of determining the overall operational forces endured by the cutter head and the cutter ladder. This section will use the specific energy approach introduced by Vlasblom [78] to find the relevant cutter moments and forces. It is assumed that the cut is follows a linear path with no inconsistencies in the soil and no variations in the cutting depth, thereby resulting in a constant specific energy. This produces the following power equation for the cutting force:

$$F_c = c \cdot d^\alpha \cdot v_t^\beta \cdot W \tag{B.9}$$

For:

$$d = \left(\frac{2\pi \cdot v_t}{\omega \cdot z}\right) \cdot \sin\theta = p \cdot \sin\theta \tag{B.10}$$

Where c is a constant depending on soil type and the operational conditions such as water depth, cutting depth etc., d is the cutting depth (symbols used as shown in Fig. B.3), v_t denotes the cutting velocity, W is the width of the cut, ω is the angular velocity of the cutter head, and z is the number of arms. This equation can be transformed to find the production Q and the specific energy E_s, with:

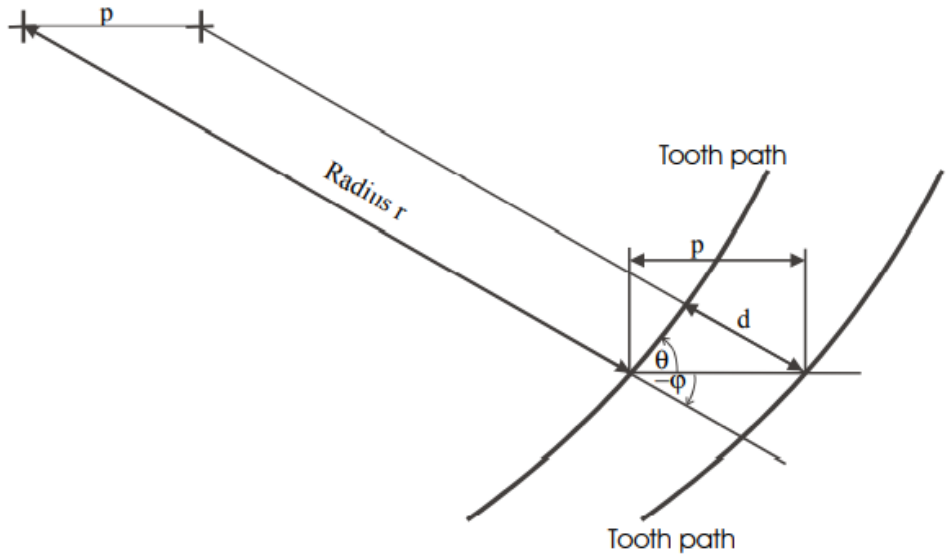

Figure B.3: Path of a single cutter tooth through the soil [78].

$$Q = d \cdot v_t \cdot W \tag{B.11}$$

$$E_s = \frac{F_c \cdot v_t}{Q} = \frac{c \cdot d^{\alpha} \cdot v_t^{\beta} \cdot W \cdot v_t}{d \cdot v_t \cdot W} = c \cdot d^{\alpha-1} \cdot v_t^{\beta} \tag{B.12}$$

Which, according to the linear cutter process, gives the following expression for F_c:

$$F_c = c \cdot d \cdot v_t \cdot W = c \cdot (p \cdot \sin\theta) \cdot v_t \cdot W \tag{B.13}$$

The specific energy approach can be expanded to find the specific torque and production of the cutter head in any soil type, but this is beyond the scope of this thesis.

B.3.1. Overcutting vs. undercutting

The cutting direction of rotation mainly affects the function of the swing winches. During undercutting, the swing wires are winched in to ensure the proper swing motion, thereby counteracting forces from the cutter which are trying to pull the opposite direction as shown in Fig. B.4. For overcutting, the self-propelling force in the direction of the swing often becomes too great, causing the cutter to 'drive' on the soil like a wheel instead of cutting it. The swing winch in this case has to provide a braking force to ensure proper cutting and slow down the swing motion [50]. Vertically, the forces are affected as well, mainly the hoisting wire tasked with lifting and lowering the cutter ladder. For undercutting, the cutter will dig itself deeper into the breach, requiring a net lifting force from the hoisting winch. In overcutting the opposite effect is required, where the own weight of the cutter ladder should keep the cutter on the right depth which means extra slack has to be given by the hoisting winch. Undercutting, especially when dredging hard soils, is the only real working condition because overcutting cannot provide a high enough cutting force [75]. It is therefore chosen to assume undercutting when determining the mooring effect of the cutter.

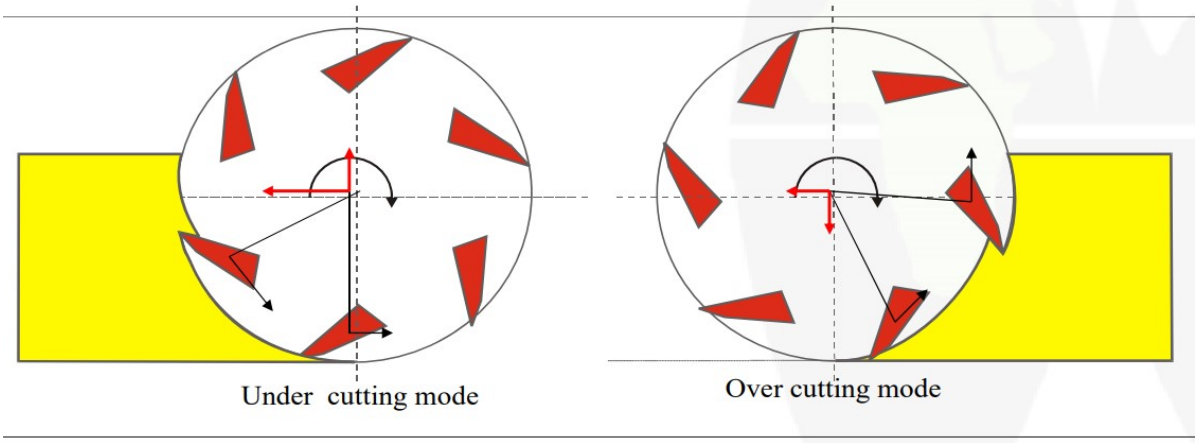

Figure B.4: Differences between overcutting and undercutting [78].

C

Appendix C: Verification of a barge model

To verify the values of the added viscous damping in the model, a comparison study was done with experimental data found by Brown et al. [7] in their 1983 study *'Barge motions in random seas: a comparison of theory and experiment'*. This study uses a model flat-bottomed barge with zero forward speed in both regular and random waves. For the purpose of this comparison, the sharp-keeled barge of 1:36 scale was replicated in ANSYS AQWA, with geometry parameters as given in Table C.1, to find the hydrodynamic coefficient matrices. The RAO's were then found using a MATLAB script using Eq. 5.2. The equivalent AQWA model is shown in Fig. C.7. Brown tests two configurations of the barge, one with a rounded keel and one with a sharp keel edge profile. Due to the similarities with the eventual CSD model, the sharp keel edge profile barge is recreated at a 1:36 scale (the same scale used in the Brown study).

Parameter	1:36 scale value
Length	2.4 m
Breadth	0.8 m
Height	0.34 m
Draught	0.105 m
Mass	200.8 kg
Distance CoG above keel [m]	0.111 m
K_{xx}	0.244 m
K_{yy}	0.688 m
K_{zz}	0.598 m

Table C.1: Geometry and mass properties of the model barge [7].

A frequency domain study was done to check the agreement of the natural modes and responses with experimental data. To achieve this, a head sea and beam sea condition were modelled. For these conditions the three most significant motion responses were chosen, which are heave, pitch and roll. The 20 frequencies were checked in the AQWA Hydrodynamic Diffraction model, processed into an EOM MATLAB model over the range of 0 - 15 rad/s. The results are shown in Fig. C.1 - C.6. The agreement is good with standard LWT potential theory for surge, sway, heave and pitch.

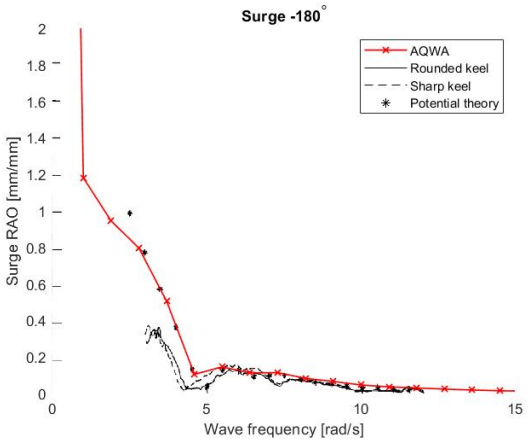

Figure C.1: Surge RAO in head seas.

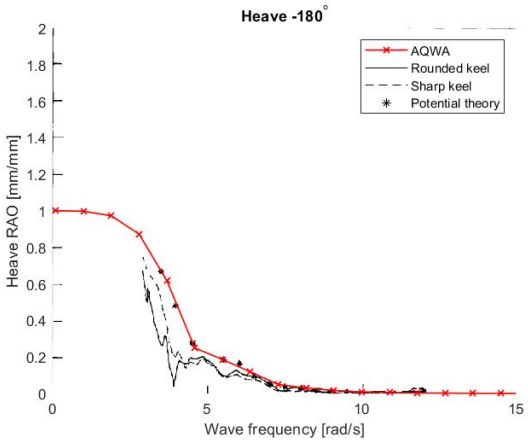

Figure C.2: Heave RAO in head seas.

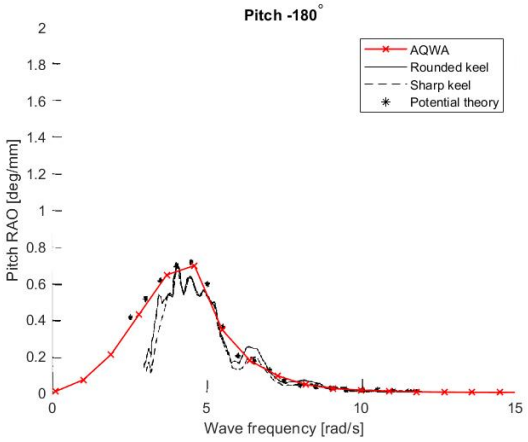

Figure C.3: Pitch RAO in head seas.

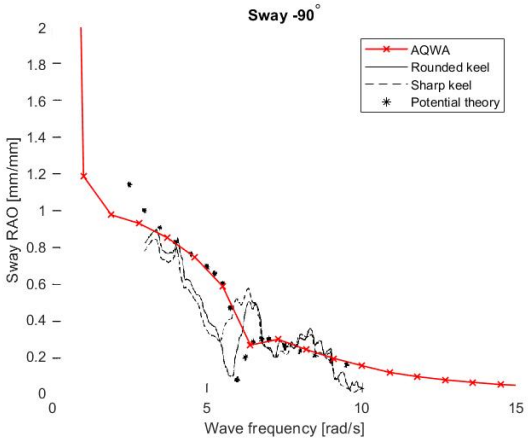

Figure C.4: Sway RAO in beam seas.

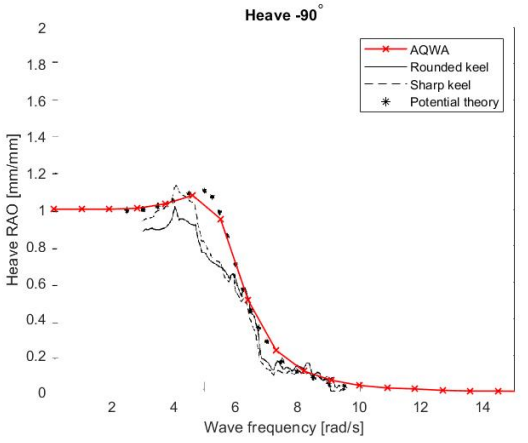

Figure C.5: Heave RAO in beam seas.

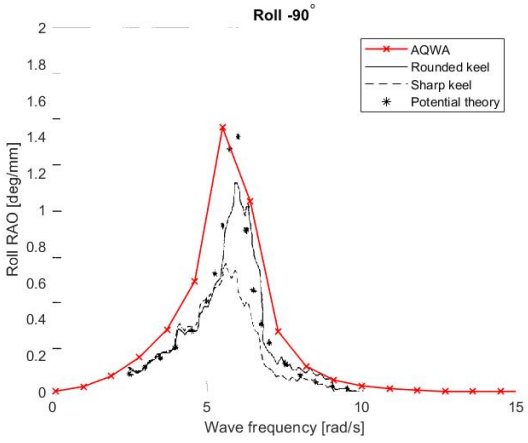

Figure C.6: Roll RAO in beam seas.

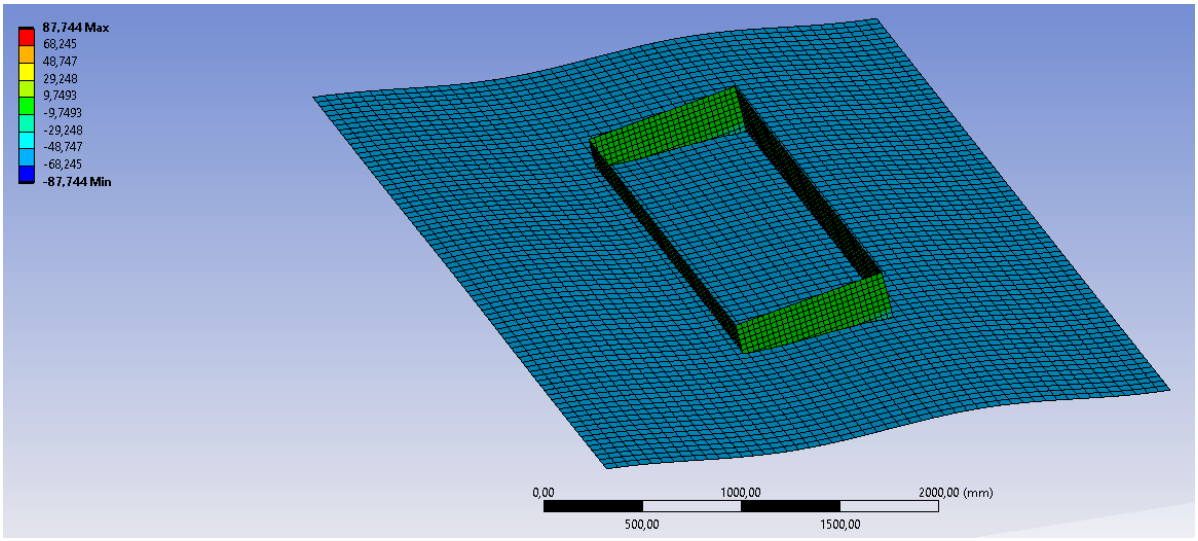

Figure C.7: ANSYS AQWA model of the model barge.

As mentioned in Section 2.1, the assumption of no viscosity has a large effect especially on the roll response motion near natural frequency. Therefore extra viscous damping is added as is discussed in Section 4.3, ignoring the bilge keel damping and lift damping components. General assumptions made for ship-like structures are that viscous roll damping lies within a range of 3% to 7% of the critical roll damping of the ship [9]. Fig. C.8 shows the correlation of the damping with the experimental data found by Brown:

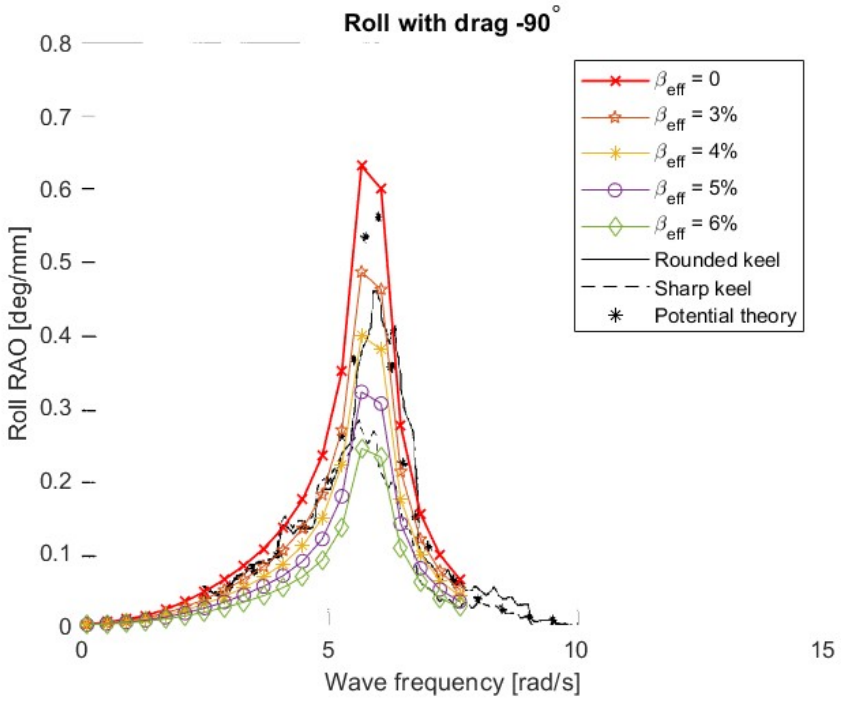

Figure C.8: Roll RAO including viscous roll damping in beam seas.

It can be seen that the experimental data has the best agreement with a viscous damping component equal to 4 or 5% of the critical damping factor. This verifies the approach taken to find the viscous damping for the CSD in Section 4.3.

Appendix D: Additional Results - FD

This appendix will provide additional results from the frequency domain calculations in Chapter 6.

D.1. Response Amplitude Operators

This section will expand on the RAOs given in Sections 6.3 and 6.4. It varies RAOs over the full range of wave directions in a shallow water depth of 5 m, and a range of wave frequencies to cover all possible operational conditions in coastal areas.

From these figures, a base-level verification can be performed. The following rules should be adhered to:

- **Surge:** There should be limited to no surge motion in beam seas of α = 90°.
- **Sway:** There should be limited to no sway motion in head seas of α = 180°.
- **Heave:** The peak in heave motion should not significantly exceed 1 m/m. This means the CSD moves with the fluid motion.
- **Roll:**
  - Roll resonance is heavily dependent on the beam geometry of the CSD. The largest resonance peak should occur when $B = 0.5 \cdot \lambda$.
  - There should be limited to no roll motion in head seas of α = 180°.
- **Pitch:**
  - Pitch resonance is heavily dependent on the length geometry of the CSD. The largest resonance peak should occur when $L = 0.5 \cdot \lambda$.
  - As opposed to roll motion, there can be a pitch motion in beam seas of α = 90°, due to the rotation of the CSD around the spud instead or around it COG. Because the CSD is heavily asymmetrical across the yz-plane, there could exist a larger heave response for the front of the CSD compared to the back and vice versa. This causes a pitch motion.
- **Yaw:** There should be limited to no yaw motion in head seas of α = 180°.

D.1.1. RAOs | CS

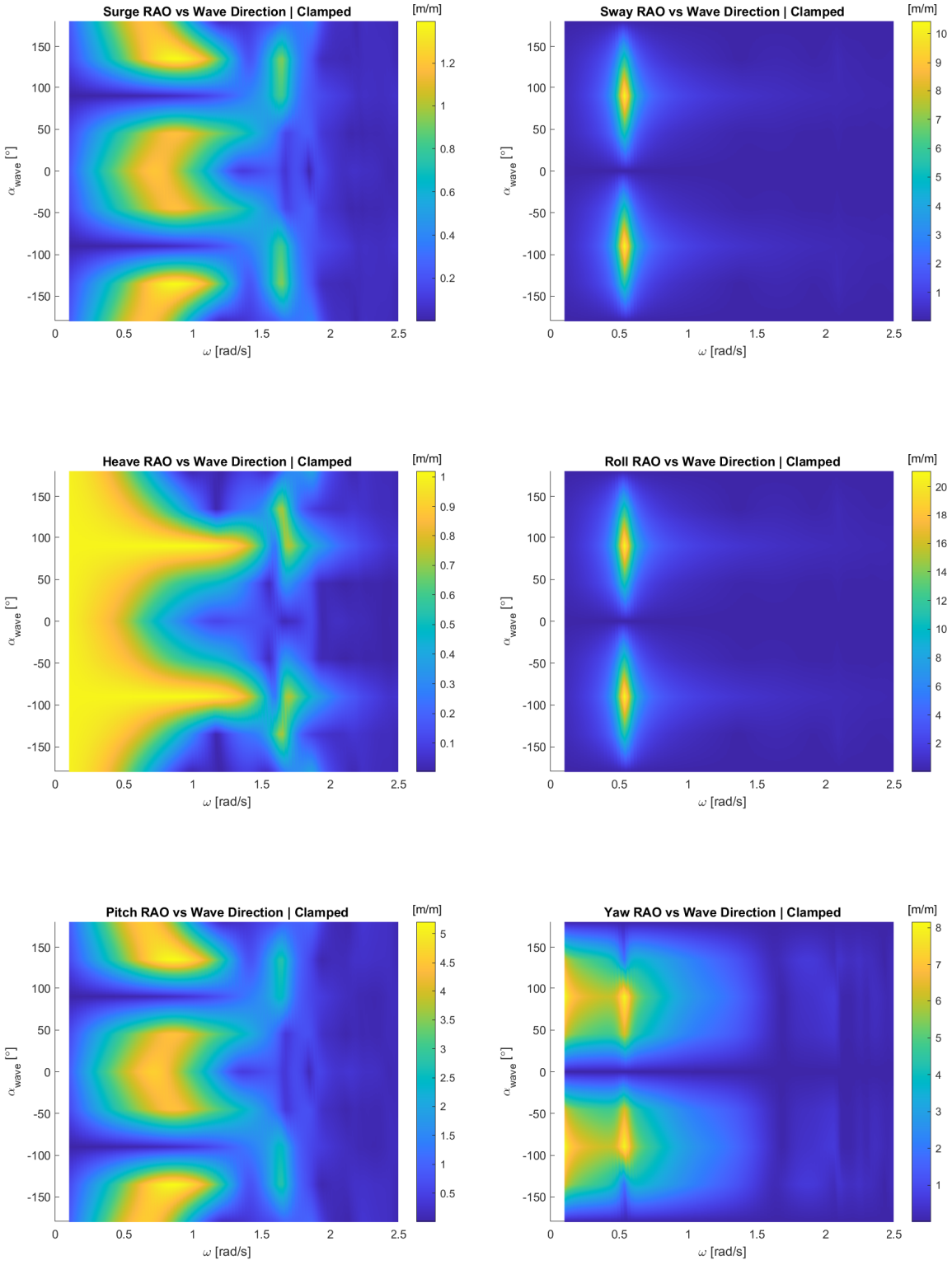

Figure D.1: Complete FD RAO results for the clamped spud configuration for all wave directions.

D.1.2. RAOs | 0% FS

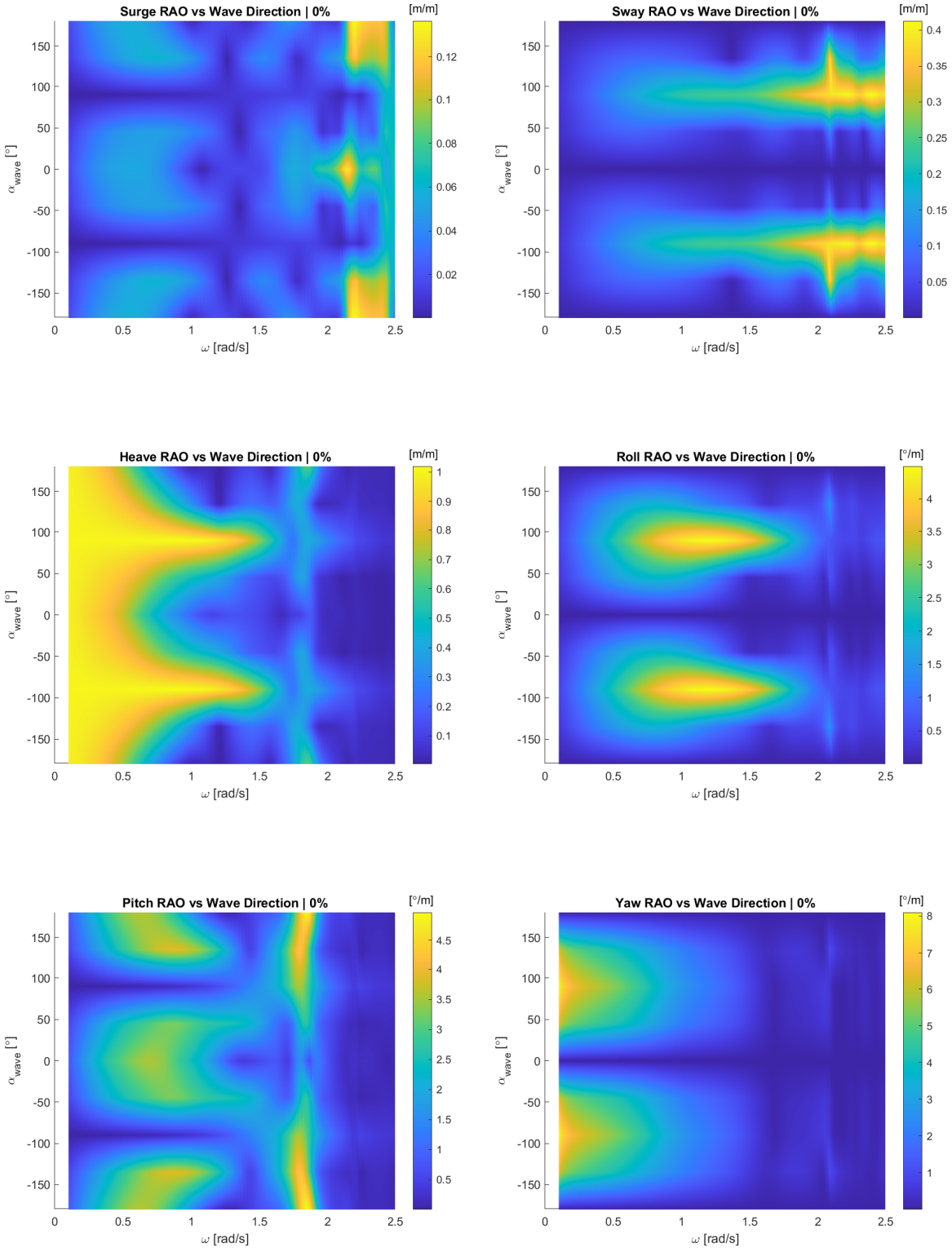

Figure D.2: Complete FD RAO results for the 0% spud configuration for all wave directions.

D.1.3. RAOs | 5% FS

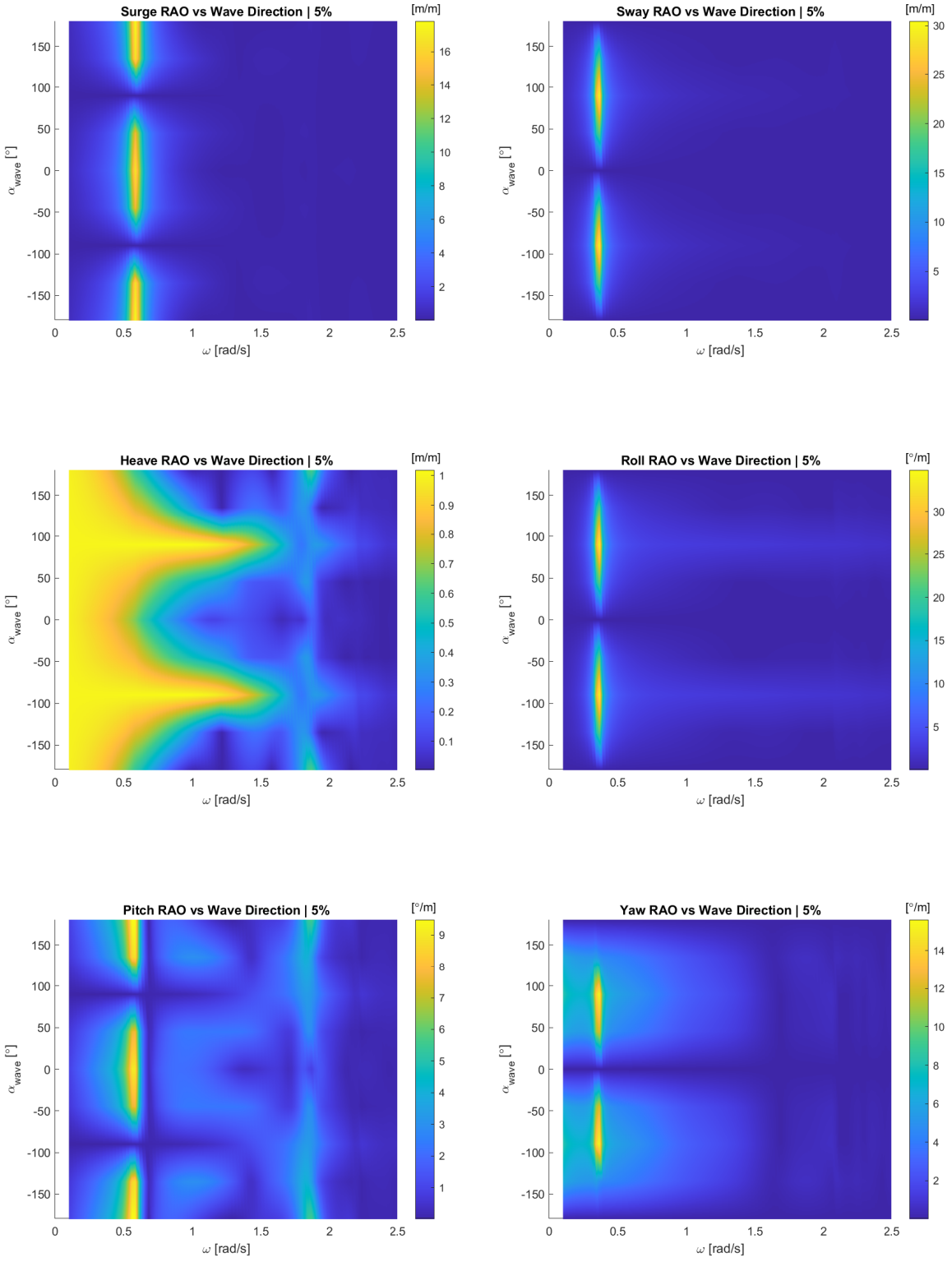

Figure D.3: Complete FD RAO results for the 5% spud configuration for all wave directions.

D.1.4. RAOs | 10% FS

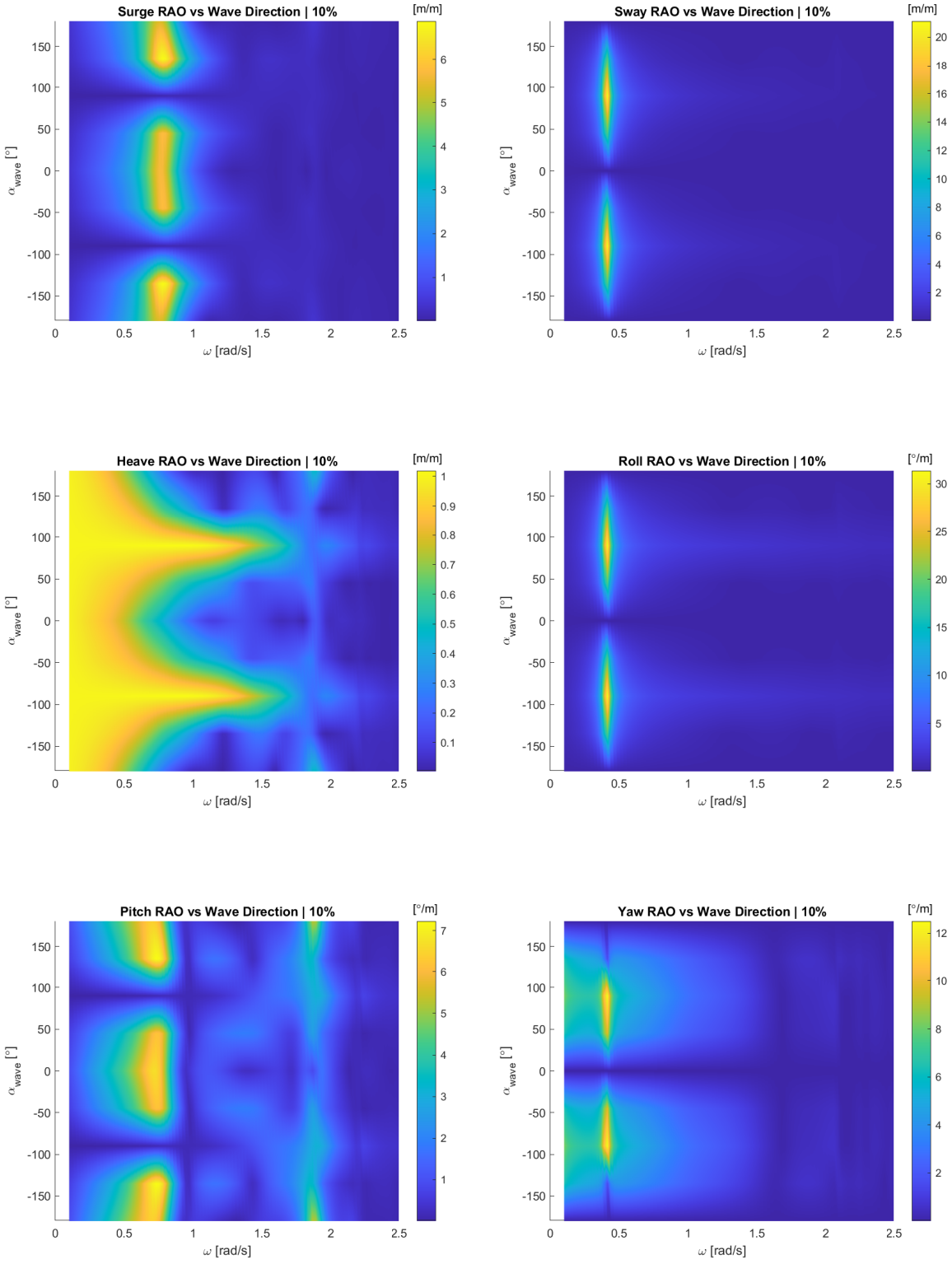

Figure D.4: Complete FD RAO results for the 10% spud configuration for all wave directions.

D.1.5. RAOs | 20% FS

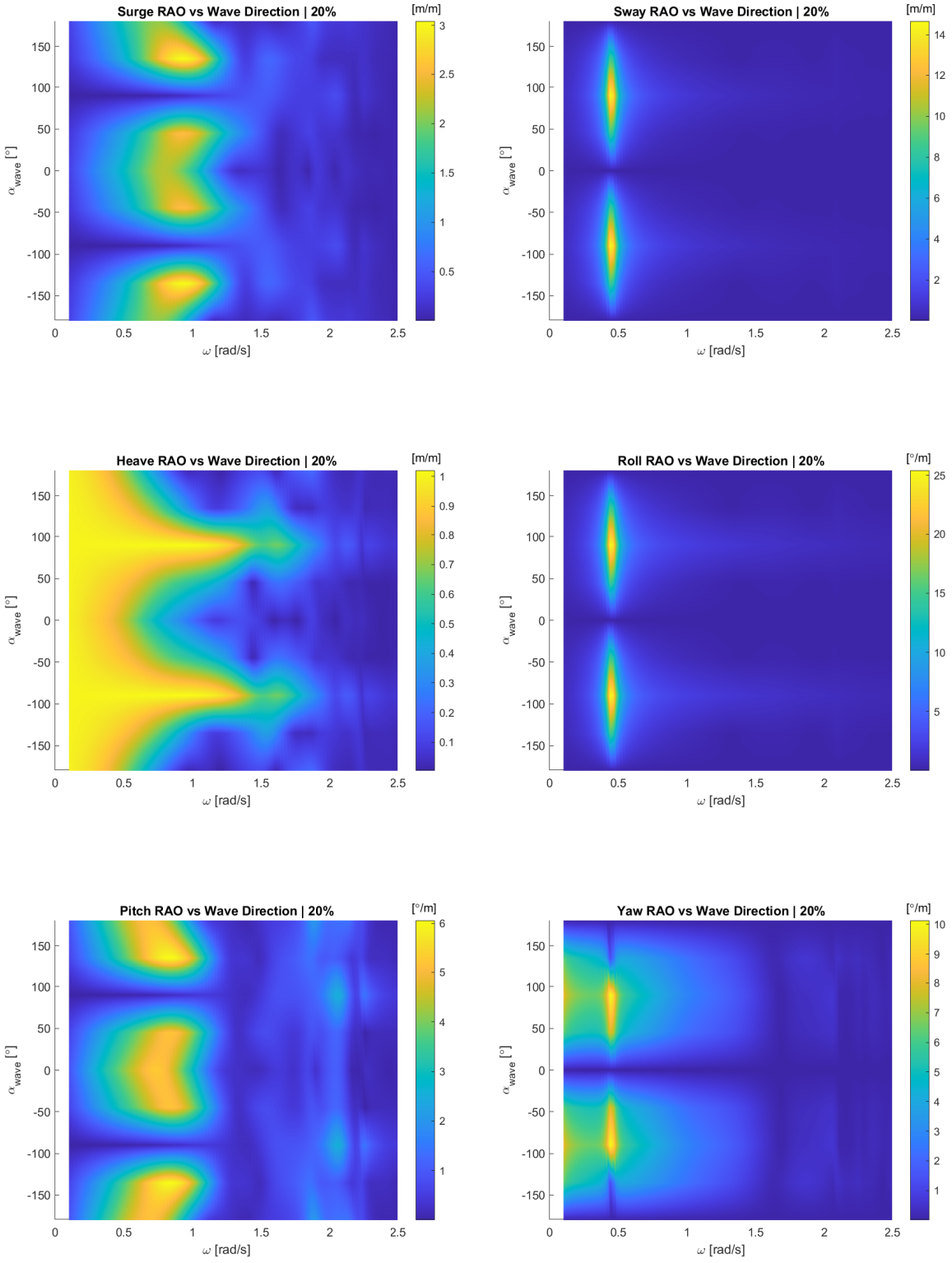

Figure D.5: Complete FD RAO results for the 20% spud configuration for all wave directions.